

## DNA-capped silver nanoparticles for stochastic nanoparticle impact electrochemistry

Lena Nörbel

Information

Band / Volume 66

ISBN 978-3-95806-541-3





Forschungszentrum Jülich GmbH  
Institute of Biological Information Processing  
Bioelectronics (IBI-3)

# **DNA-capped silver nanoparticles for stochastic nanoparticle impact electrochemistry**

Lena Nörbel

Schriften des Forschungszentrums Jülich  
Reihe Information / Information

Band / Volume 66

ISSN 1866-1777

ISBN 978-3-95806-541-3



Bibliografische Information der Deutschen Nationalbibliothek.  
Die Deutsche Nationalbibliothek verzeichnet diese Publikation in der  
Deutschen Nationalbibliografie; detaillierte Bibliografische Daten  
sind im Internet über <http://dnb.d-nb.de> abrufbar.

Herausgeber  
und Vertrieb:           Forschungszentrum Jülich GmbH  
                              Zentralbibliothek, Verlag  
                              52425 Jülich  
                              Tel.: +49 2461 61-5368  
                              Fax: +49 2461 61-6103  
                              **zb-publikation@fz-juelich.de**  
                              **[www.fz-juelich.de/zb](http://www.fz-juelich.de/zb)**

Umschlaggestaltung:   Grafische Medien, Forschungszentrum Jülich GmbH

Druck:                    Grafische Medien, Forschungszentrum Jülich GmbH

Copyright:              Forschungszentrum Jülich 2021

Schriften des Forschungszentrums Jülich  
Reihe Information / Information, Band / Volume 66

D 82 (Diss. RWTH Aachen University, 2021)

ISSN 1866-1777  
ISBN 978-3-95806-541-3

Vollständig frei verfügbar über das Publikationsportal des Forschungszentrums Jülich (JuSER)  
unter [www.fz-juelich.de/zb/openaccess](http://www.fz-juelich.de/zb/openaccess).



This is an Open Access publication distributed under the terms of the [Creative Commons Attribution License 4.0](https://creativecommons.org/licenses/by/4.0/),  
which permits unrestricted use, distribution, and reproduction in any medium, provided the original work is properly cited.

## Abstract

One of the major challenges in analytical chemistry is reducing the detection limit of an analyte down to a level where the specific identification of a single entity is possible. In this context, nano-impact electrochemistry is one of the most active and promising research areas in the field of single-entity experiments. This method is a versatile analytical procedure for characterization and real-time monitoring of bioconjugation and biomolecular recognition events as well as for ultrasensitive detection of a variety of biological species. The combination of a highly sensitive amplifier system and high-density microelectrode arrays allows detection of single silver nanoparticle impacts down to subpicomolar concentrations. For the analyte detection, silver nanoparticles are modified with biomolecular receptors alternating their impact frequency on the electrode surface. Thus, the particles serve as redox tags converting an otherwise redox-inactive target into an electrochemically detectable species. In this work, silver nanoparticles were modified with thiolated single stranded oligonucleotides with varying molar ratios of DNA to nanoparticles. The modified conjugation protocol resulted in stable DNA-nanoparticle conjugates. In depth characterization of these conjugates gave insight into their structural and physicochemical properties. In a next step, the impact behaviour of DNA-capped nanoparticles was evaluated and compared to citrate-capped nanoparticles. Different parameters were identified to influence the impact probability. First, the surface modification results in a higher nanoparticle stability by preventing particle aggregation, which increases the impact frequency, especially in the presence of high salt concentrations. Second, the redox activity is reduced in comparison to citrate stabilized particles. In particular, the ligand surface density as well as the conformation and size of the receptor molecule were found to play a crucial role. Furthermore, the composition of the electrolyte and the applied potential affect the impact probability, but to a different extent as for citrate stabilized particles. By carefully adjusting the surface density of ligands, a high particle stability is achieved while maintaining their desired redox activity. The results demonstrate that DNA-AgNPs possess impact characteristics different from standard citrate stabilized particles. In a last step, stochastic nanoparticle impact electrochemistry was probed for the detection of DNA hybridization events on the nanoparticle surface. The results disclose decreased hybridization efficiencies on the nanoparticle surface and reveal that a surface-bound process is more complicated when compared to hybridization in solution.



## Zusammenfassung

Eine der größten Herausforderungen in der analytischen Chemie ist es, die Nachweisgrenze für einen bestimmten Analyten so zu verringern, dass die spezifische Identifizierung einer einzelnen Einheit möglich ist. Ein besonders aktives und vielversprechendes Forschungsfeld sind elektrochemische Kollisionsexperimente. Diese Methode stellt ein vielseitiges analytisches Instrument zur Charakterisierung von biomolekularer Interaktion und dem sensitiven Nachweis verschiedener biologischer Spezies dar. Die Kombination aus einem sensitiven Verstärker und Mikroelektrodenarrays ermöglicht die Detektion einzelner Silber-Nanopartikel im subpikomolaren Bereich. Die Nanopartikel sind mit biomolekularen Rezeptoren gekoppelt, welche eine Affinität für den zu analysierenden Liganden aufweisen. In dieser Konstellation fungieren die Nanopartikel als Redoxmarkierung. Auf diese Weise ist es möglich, einen redox-inaktiven Liganden elektrochemisch nachzuweisen. Die Kopplung des Rezeptors beeinflusst die Frequenz, mit welcher die Nanopartikel mit der Elektrode kollidieren und diese Frequenz dient als Messgröße. In dieser Arbeit wurde einzelsträngige DNA mit Hilfe einer Thiolgruppe an Silber-Nanopartikel gebunden. Die Kopplung wurde für verschiedene molare Verhältnisse von DNA zu Nanopartikel durchgeführt und resultierte in stabilen Nanopartikel-DNA Komplexen. Eine detaillierte Charakterisierung ergab Aufschluss über die strukturellen und physikalisch-chemischen Eigenschaften der Nanopartikel. Als Nächstes wurde das Kollisionsverhalten der DNA-funktionalisierten Nanopartikel untersucht und mit citrat-stabilisierten Partikeln verglichen. Die Kollisionswahrscheinlichkeit wird von mehreren wichtigen Faktoren beeinflusst. Generell ist die Redoxaktivität im Vergleich zu citrat-stabilisierten Partikeln verringert. Die DNA-Kopplung führt jedoch zu einer verbesserten Stabilität der Nanopartikel, weshalb die Kollisionsfrequenz bei Messungen in hohen Salzkonzentrationen erhöht ist. Hierbei sind vor allem die Ligandendichte auf der Oberfläche, sowie Konformation und Größe der DNA-Moleküle von besonderer Bedeutung. Zusätzlich wird das Kollisionsverhalten von der Zusammensetzung des Elektrolyten und dem angelegten Potential beeinflusst, jedoch in anderem Maße als bei citrat-stabilisierten Partikeln. Eine sorgfältige Einstellung der Ligandendichte ermöglicht die Herstellung stabiler Partikel unter Beibehaltung ihrer gewünschten redox-aktiven Eigenschaften. Die Ergebnisse verdeutlichen, dass DNA-stabilisierte Nanopartikel eine andere Kollisionscharakteristik besitzen als Citrat-stabilisierte. Im letzten Schritt wurden die elektrochemischen Kollisionsexperimente für den Nachweis von DNA-Hybridisierung auf der Nanopartikeloberfläche verwendet. Die Ergebnisse zeigen eine verringerte Effizienz der Hybridisierung und verdeutlichen, dass der Prozess an der Partikeloberfläche um ein Vielfaches komplizierter ist als in Lösung.



# Contents

<b>1</b>	<b>Introduction</b>	<b>1</b>
<b>2</b>	<b>Background</b>	<b>5</b>
2.1	Fundamentals of electrochemistry . . . . .	5
2.1.1	Electrode/electrolyte interface . . . . .	5
2.1.2	Electrode processes . . . . .	7
2.1.3	The standard electrode potential . . . . .	8
2.1.4	Electrode kinetics . . . . .	10
2.1.5	Diffusion-limited currents . . . . .	11
2.2	Metallic nanoparticles and deoxyribonucleic acid (DNA) . . . . .	13
2.2.1	Metallic nanoparticles . . . . .	13
2.2.2	Deoxyribonucleic acid (DNA) . . . . .	17
2.2.3	DNA functionalized metallic nanoparticles . . . . .	19
2.3	Stochastic nanoparticle impact electrochemistry . . . . .	21
2.3.1	Overview of different types of impacts . . . . .	22
2.3.2	Behaviour of individual nanoparticles at the nano-interface . . . . .	25
<b>3</b>	<b>Materials and methods</b>	<b>27</b>
3.1	Microelectrode array . . . . .	27
3.1.1	MEA composition and layout . . . . .	27
3.1.2	Electrochemical characterization . . . . .	28
3.2	BioMAS measurement device . . . . .	30
3.2.1	Pre-amplification headstage 'Pico Amp' . . . . .	31
3.2.2	Main-amplifier . . . . .	32
3.2.3	General measurement procedure . . . . .	32
3.2.4	Data analysis . . . . .	34
3.3	Nanoparticle modification and characterization . . . . .	35
3.3.1	Preparation of DNA . . . . .	35
3.3.2	Nanoparticle modification and separation . . . . .	36
3.3.3	UV-Vis spectroscopy . . . . .	37
3.3.4	Determination of DNA strand density on nanoparticles . . . . .	37
3.3.5	Dynamic light scattering and zeta potential . . . . .	38

3.3.6	Inductively coupled plasma mass spectrometry . . . . .	39
3.3.7	Scanning transmission electron microscopy . . . . .	39
3.4	DNA hybridization . . . . .	39
3.4.1	SYBR Green fluorescence assay . . . . .	39
3.4.2	Nanoparticle impact electrochemistry . . . . .	40
3.5	Buffers, chemicals and reagents . . . . .	41
3.6	Statistics and python based data evaluation . . . . .	42
<b>4</b>	<b>Particle modification and characterization</b>	<b>43</b>
4.1	Physical and chemical properties . . . . .	44
4.2	Density of DNA strands on nanoparticles . . . . .	48
4.3	Summary . . . . .	53
<b>5</b>	<b>Stochastic nanoparticle impact electrochemistry</b>	<b>55</b>
5.1	Characterization of the BioMAS measurement device and experimental procedure	56
5.1.1	Noise analysis . . . . .	56
5.1.2	Experimental procedure . . . . .	59
5.2	Amperometric detection of silver nanoparticle oxidation . . . . .	62
5.3	Comparison between citrate- and DNA-capped nanoparticles . . . . .	65
5.4	Influence of supporting ion identity and concentration . . . . .	68
5.5	Influence of DNA density and length . . . . .	73
5.6	Single stranded DNA with secondary structure . . . . .	78
5.7	Summary . . . . .	80
<b>6</b>	<b>Detection of DNA hybridization</b>	<b>83</b>
6.1	Experimental evaluation and predictions of single stranded DNA structure . .	83
6.2	DNA hybridization in solution . . . . .	87
6.3	DNA hybridization on nanoparticles . . . . .	89
6.4	Impact based detection of DNA hybridization . . . . .	92
6.5	Summary . . . . .	93
<b>7</b>	<b>Summary and Outlook</b>	<b>95</b>
<b>8</b>	<b>Appendix</b>	<b>99</b>
	<b>Bibliography</b>	<b>111</b>
	<b>List of Figures</b>	<b>135</b>
	<b>List of Tables</b>	<b>139</b>
	<b>Acknowledgements</b>	<b>140</b>

# 1 Introduction

Reducing the detection limit of an analyte is one of the major challenges in analytical chemistry. The ultimate goal is the specific detection of a single entity, such as an atom, a molecule, a nanoparticle, a virus or a cell. Recent advances in measurement science are pushing the limits and we are reaching a point where single entity sensitivity can be accomplished [1–3]. But why is it important to investigate a single entity? First, it allows separation of discrete responses from the bulk [4]. Conventional methods are based on measuring an average quantity over a large array of entities, which fades out the unique features of an individual entity and its dynamics [5]. Decoding the contribution of a single entity to the ensemble response could significantly advance the understanding of their physicochemical properties such as catalytic or electrochemical activity. Additionally, obtaining information on the temporal and spatial distribution of entities or events could provide a deeper understanding of many biological and technological processes [2,4]. Second, single entity experiments enable investigation of electron transfer reactions at a level, where they have not been probed before. This could pave the way to answer fundamental questions about electron transfer processes, and give rise to entirely new types of experiments [5–7]. Third, detection of a single entity corresponds to the ultimate mass-sensitivity. This has the potential to revolutionize diagnostics by providing access to detection of very dilute species at an early stage [1,2,7,8].

Electrochemistry is pioneering in the field of single entity experiments due to several reasons. It exhibits inherent sensitivity essential for this type of experiments in combination with simple experimentation, fast response and low operational costs. One of the most active and promising topics in single entity electrochemistry is stochastic nano-impact electrochemistry [3,4,9,10]. For a typical experiment, an electrode held at a certain electric potential is submerged into an electrolyte solution. This solution contains a freely-diffusing analyte nanoparticle of interest. Brownian motion induces stochastic collisions of the nanoparticle with the electrode. Such a nanoparticle impact can be monitored in the current response of the electrode, revealing information on the nanoparticle population [11,12]. Stochastic nano-impact electrochemistry is a promising experimental procedure for different analytical purposes. One of the most direct applications is the detection and characterization of nanoparticles [13,14]. With the fast advance of nanotechnology, nanomaterials find widespread use in a variety of fields such as medicine, cosmetics, food, and electronics. A result of this rising usage of nanomaterials is the release of extensive quantities of nanoparticles into the



environment. Consequently, there is an exigent demand for the development of analytical methodologies for quantification, characterization and monitoring of nanoparticles in biological and environmental samples [15, 16]. Compton and co-workers demonstrated the detection, quantification and sizing of silver nanoparticles in different real-world samples spiked with nanoparticles such as sea, tap or bottled water [17–19]. Furthermore, there is increasing interest to utilize this method for characterization and monitoring of bioconjugation and biomolecular recognition events such as DNA hybridization. Additionally, the methodology holds potential for sensitive detection of a variety of biological species including DNA, RNA, enzymes, viruses, bacteria or cells [3, 7, 14]. A possible approach could involve the use of surface-modified nanoparticles as label with a modification via adsorption or coating with molecules (analytes). Since the electrochemical response shows a strong dependence on the nanoparticle’s surface properties, any surface alteration could be monitored via collision [2, 14]. The Bard group demonstrated the detection of individual DNA hybridization events by using platinum nanoparticles modified with oligonucleotides [20]. Later, Crooks employed an analogue scheme for the detection of microRNA strands [21]. Andreescu and co-workers used an approach based on silver nanoparticles with single stranded DNA targets (aptamers) on their surface for probing of biorecognition and surface modification. The functionalization with DNA resulted in a decrease in redox activity, which could be restored upon aptamer target binding [22]. However, overall successful application for diagnostic purposes has been rare and the repertoire of analytes is limited.

For the detection of single entities different challenges and limitations have to be considered. To begin with, the electrochemical current arising from a single entity, such as a biomolecule, is small and can easily be exceeded by a background current. Therefore, sensitive low-noise equipment, small-sized electrodes for noise reduction and suitable detection schemes for signal amplification are required. Furthermore, a direct electrochemical detection of redox-inactive targets is not possible and for such targets the development of an adequate detection scheme is required [5, 23–25]. Additionally, an ultimate sensitivity in terms of mass does not automatically correspond to a high sensitivity with respect to concentration [8]. In single entity electrochemistry, the electrode size usually has to be approximately in the size range of the entity under investigation. The overall collision frequency is determined by the size of the electrode and mass-transfer. For rare analytes in a large sample volume, the statistical probability of an electrode interaction is low. This results in excessive measurement times, which in turn limit the experimental feasibility [2, 26]. Simply increasing the electrode size to enhance the collision probability, however, would strongly decrease sensitivity due to higher noise levels. A solution to this problem could be performing measurements on a larger number of electrodes simultaneously. In such an arrangement, each individual electrode exhibits the capability of identifying discrete events and together they enable detection of ultra-low concentrations [2, 8]. However, the most challenging task is the introduction of specificity for

---

the colliding entity. In case of Faradaic charge transfer, three different main nano-impact strategies exist: blocking, electrocatalytic amplification and material dissolution. The first two approaches rely on indirect nanoparticle detection. For blocking impacts, the current flux from a solution-phase redox tracer is monitored. This flux is blocked upon collision of an insulating nanoparticle. The electrocatalytic approach monitors the current flux generated by a redox-reaction at the surface of a colliding nanoparticle. This reaction can exclusively occur at the nanoparticle due to its electrocatalytic activity [11,12]. Possible interference from other blocking or electroactive species in the sample impedes the potential for specificity [2]. Additionally, electrocatalytic amplification is often performed in hydrazine solutions [20,21], which could be problematic for point-of-care applications due to its toxicity. In contrast, the material dissolution strategy is based on direct oxidation of a nanoparticle. During the experiment, the electrode is held at an oxidizing potential. Upon collision with the electrode, a nanoparticle is oxidized and the resulting current response is monitored [11,12]. This approach is considered as the most promising strategy to achieve specificity [2]. Due to the high packing density of metal atoms within a nanoparticle, the current response can be very large, resulting in a high signal-to-noise ratio, since each atom of the nanoparticle contributes to the charge transfer [2]. In our group, it has been demonstrated that a highly sensitive amplifier system in combination with a microelectrode array allows detection of single silver nanoparticles in aqueous solution. This material dissolution based approach enables analysis of sub-picomolar nanoparticle concentrations [27]. The use of microelectrode arrays combines low background currents with high throughput and spatial information and directly addresses the described limitations for ultra-low analyte concentrations.

The aim of this work is to lay a foundation for advancing the silver based material dissolution approach into an universal biomolecular detection method. A key challenge for this development is the introduction of specificity. Our strategy utilizes the redox-activity of silver nanoparticles and combines it with the specificity of biomolecular recognition elements. This can be achieved by coupling of biomolecular receptors to silver nanoparticles. Single stranded DNA represents an attractive receptor molecule, offering not only the detection of complementary DNA but also of a variety of different ligand classes if DNA aptamers are employed [28]. To accomplish this challenge, several fundamental questions have to be resolved. Central issues are the nanoparticle modification and the influence of the receptor molecules on nanoparticle impact experiments. In order to address this issues, different DNA strands are attached to the nanoparticle surface via thiol chemistry. This process has to be optimized in order to get stable DNA-AgNP conjugates over a wide range of DNA concentrations and oligonucleotide length. Additionally, a detailed characterization of the as prepared conjugates is crucial. The corresponding results are discussed in chapter 4. In case of citrate-capped silver nanoparticles several studies have contributed to identify critical parameters for nanoparticle impact measurements and the system is relatively well-understood [27,29–32]. However, for

the introduction of DNA as ligand a strong impact on the oxidation behaviour has been reported [22,33]. In order to gain a better understanding of the influence of the DNA, a detailed evaluation of the oxidation process in presence of DNA is performed. Special attention is paid to DNA concentration, length and conformation. Additionally, the role of the measurement parameters, such as applied potential or background electrolyte, was examined. The results are presented in chapter 5. Finally, stochastic nanoparticle impact electrochemistry is probed for the detection of DNA hybridization events on the nanoparticle surface and the related results are elucidated in chapter 6.

## 2 Background

### 2.1 Fundamentals of electrochemistry

This section gives an overview of some fundamental theories of electrochemistry. In general, electrochemistry describes the processes and structures occurring at the interface between an electronic conductor (electrode) and an ionic conductor (electrolyte) or at the interface between two electrolytes [34]. While evolving, electrochemistry had great influence on the understanding of electricity and the development of chemistry in general and it still has strong links to other research fields [35]. Especially, electroanalytical techniques are of great interest as they enable first-hand access to detailed information on chemical, physical and biological processes [36].

#### 2.1.1 Electrode/electrolyte interface

Initially, when solids, such as metals, alloys, semiconductors or insulators, are immersed into an electrolyte solution, electric current flows until reaching of the electrochemical equilibrium. Reason for that is a difference in the Fermi energy of the electrons in the solid and the redox potential of the electrolyte, which are equal at equilibrium. The transfer of electric charges results in development of a specific interfacial region with a charge distribution different from the bulk. On the solid side charge builds up, which is compensated on the solution side by oppositely charged ions attracted to the metal surface by Coulomb interactions. The resulting electrical charge separation is called the electrochemical double layer (EDL), which can be considered as a capacitor. Since this interface has crucial influence on electrochemical processes it is necessary to have a closer look on its structure and properties [35–38].

Heinrich von Helmholtz reported the first detailed theoretical description of the electrochemical double layer in 1879. He inferred that the interphase consists of a compact layer of ions in close contact with the charged metal surface (Helmholtz layer). Hence, the EDL can be described as a parallel-plate capacitor with a separation distance corresponding to the closest approach of the centre of an ion to the surface [39]. However, this model does not consider a dependency of the capacitance values on the applied potential or any changes in concentration due to thermal motion [35]. Later Gouy and Chapman presented a model accounting for

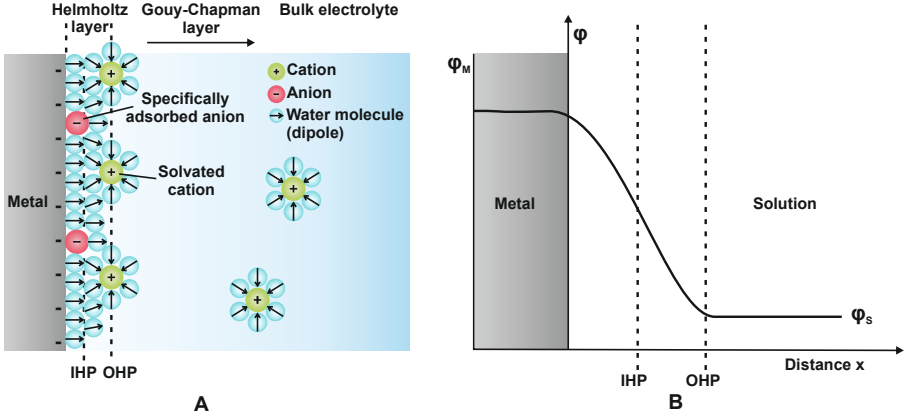


**Figure 2.1:** A) Illustration of the electrochemical double layer with the compact Helmholtz and diffusive Gouy-Chapman layer. B) Electric potential profile across the double layer (adapted from ref. [36,38]).

thermal motion of the ions. The effects of the electrostatic forces together with the thermal motion in the solution lead to the formation of a diffuse double layer with the accumulated ions extending to some distance from the metal surface. The charge distribution of ions as a function of distance to the electrode surface can be described by Maxwell-Boltzmann statistics [40,41]. This model is in good accordance with the experimentally observed results but fails for higher electrolyte concentrations and electrostatic potentials since it disregards the size of the ions [35]. In 1924, Stern proposed a new model combining both, a rigid and a diffusive layer with the definition of a plane of closest approach of ions to the surface, the Helmholtz plane [42]. Grahame refined this model by suggesting a difference between chemical and electrostatic adsorption of ions. When the ions are adsorbed due to strong and localized chemical forces they are deformed and partially dehydrated resulting in a loss of mobility. These specifically adsorbed ions form the compact inner layer with the locus of their centres termed inner Helmholtz plane (IHP). In the case of electrostatic interaction the adsorption forces are weaker and thus, the ions are not deformed, which allows them to still take part in thermal motion. The approach of those solvated ions is only possible to a certain distance, which is called the outer Helmholtz plane (OHP) and is defined as the locus of centres of nearest solvated ions. Due to thermal movement these solvated ions are diffusively distributed in a three-dimensional area corresponding to the diffusive layer or Gouy-Chapman layer [35,38,42,43].

The thickness of the electrochemical double layer can be estimated as  $1.5 \kappa^{-1}$ . For a  $z:z$  electrolyte, the Debye-Hückel length  $\kappa^{-1}$  is given by Equation 2.1 with the relative dielectric permittivity of the solvent  $\epsilon_r$ , permittivity of the vacuum  $\epsilon_0$ , Boltzmann constant  $k_B$ , tempera-

ture  $T$ , bulk concentration of electrolyte  $c^b$ , ion charge  $z$  and elementary charge  $e$ .

$$\kappa^{-1} = \sqrt{\frac{\epsilon_r \epsilon_0 k_B T}{2c^b z_i^2 e^2}} \quad (2.1)$$

The profile of the electric potential across the double layer is depicted in Figure 2.1B. It is assumed that the electrode is negatively charged and the potential  $\varphi_M$  is nearly constant throughout the metal phase. A discontinuity can be observed for the metal atom layers close to the solution [36].

### 2.1.2 Electrode processes

As mentioned before, electrochemical systems deal with the electrode/electrolyte interface and associated processes upon application of an electric potential and a resulting current flow. The explanations in section 2.1 might give the impression that it is sufficient to study the electrochemical events that are taking place at a single interface. However, experimentally it is not applicable to study one isolated boundary. Instead it is necessary to consider a set of interfaces called electrochemical cell, most broadly defined as two electrodes in contact with an electrolyte.

In general, there are two different types of processes, that can take place at electrodes. In one case, a transfer of charges across the electrode/electrolyte interface occurs. Usually, this involves the transfer of electrons causing an oxidation or reduction process at the surface of the electrode. Because these processes follow Faraday's law they are termed Faradaic. According to Faraday's law of electrolysis the charge is proportional to the amount of product formed at the electrode [38]. In the other case, the composition of the electrochemical double layer changes due to a potential difference between electrolyte and electrode or a variance in the electrolyte composition, resulting in adsorption or desorption processes. Despite the absence of a charge transfer reaction a current flow can take place for a short time period. These processes are termed non-Faradaic with the double layer charging or discharging current as a prominent example [38, 44, 45]. Overall, a Faradaic electrode reaction is composed of different steps leading to the conversion of an electroactive species at the electrode surface with the slowest step being rate-determining. The processes that are influencing the reaction rate are: the mass transport of electroactive reactant and product (1), the electron transfer between the electroactive species and the electrode surface (2), chemical reactions taking place in proximity of the electrode (3) and surface reactions such as adsorption or desorption (4). An overview of the electrode reaction pathway is depicted in Figure 2.2. The first two processes hold true for all Faradaic electrode reactions whereas the others are not necessarily involved. Electrochemical reactions are defined as heterogeneous due to the fact that

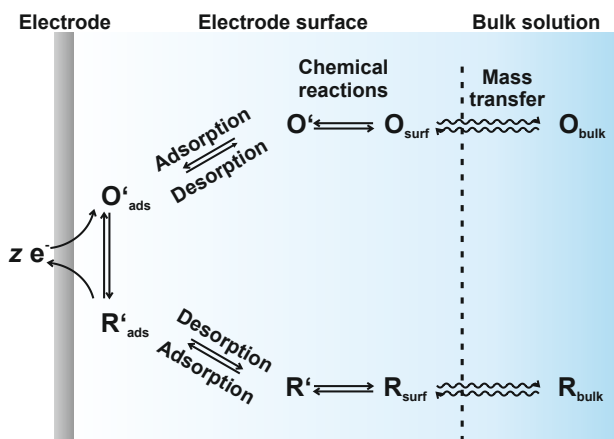


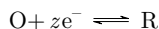
**Figure 2.2:** Scheme of an overall electrode pathway including mass transfer, chemical reactions, surface adsorption and desorption and electron transfer (adapted from ref. [38]).

they only happen at the electrode/electrolyte interface and not in the bulk electrolyte [38].

### 2.1.3 The standard electrode potential

In every electrochemical cell the overall chemical reaction is composed of two independent half-reactions (anodic and cathodic reaction). They correspond to the occurring chemical changes at the electrodes. Those half-reactions are responsive to a difference in the interfacial potential at the respective electrode but usually only one of the reactions is of interest. The electrode at which this reaction takes place is termed working electrode. The other half-reaction is standardized by the use of an electrode with a constant phase composition, the reference electrode. With this cell configuration, the potential of the working electrode is controlled with respect to the reference electrode and thus all observed changes in the cell can be attributed to the working electrode [38]. The commonly accepted primary reference electrode is the standard or normal hydrogen electrode (SHE or NHE). Its potential is defined as zero and all electrochemical potentials are reported with respect to this reference point. However, since a hydrogen electrode is difficult to handle experimentally, other reference electrodes are used. Widely employed is for example the silver/silver chloride electrode with a reference potential of around 0.2 V vs. NHE. Practically, many electrochemical experiments are performed with a three-electrode configuration. For this, the potential is measured between the reference electrode and the working electrode meanwhile the current flows between the working and a counter electrode. As a result the reference electrode exhibits a stable potential [38, 46]. The simplest case of a Faradaic electrode reaction is the direct and reversible heterogeneous

electron transfer between an electrode and an electroactive species. The following equation describes the reduction of O by uptake of  $z$  electrons (left to right). In the opposite direction the reduced species R is oxidized to O by release of  $z$  electrons.



If the working electrode is biased to negative potentials the energy levels of the electrons are increased. At some point their level is sufficiently high to transfer into unoccupied electronic states on the solution-phase species. This electron flow from the electrode to the solution causes a reduction or cathodic current and can be understood as the reduction of O to R. If the electrode is biased to positive potentials the opposite process takes place. In this case, the energy levels of the electronic states are decreased and electrons from the solution-phase species are transferred into vacant electronic states on the electrode. This electron flow from the solution to the electrode results in an oxidation or anodic current corresponding to the oxidation of the reduced species R to O. The potentials at which the described processes take place correspond to the standard potential  $E^0$ , which is material and concentration dependent [38,46].

The overall cell potential corresponds to the potential difference between the two electrodes and can be related to changes of the Gibbs free energy  $\Delta G$  in the system. For an electrochemical equilibrium, the relation between Gibbs free energy  $\Delta G$  and the equilibrium potential  $E_{eq}$  is:

$$\Delta G = -zFE_{eq} \quad (2.2)$$

with the number of electrons  $z$  and the Faraday constant  $F$ . For reactant and product having unit activity and the reduction taking place Equation 2.2 can be expressed as:

$$\Delta G^0 = -zFE^0 \quad (2.3)$$

with the electrochemical standard potential  $E^0$  and the standard Gibbs free energy change  $\Delta G^0$ . With the Gibbs free energy  $\Delta G$  and the ratio of reduced to oxidized species it is now possible to link the electrode potential  $E_{eq}$  with the concentrations of the reactants. The mathematical expression for this correlation is referred to as the Nernst equation (Equation 2.4) with the universal gas constant  $R$ , temperature  $T$ , number of electrons  $z$ , Faraday constant  $F$  and the activity of reactive species  $a_O$  and  $a_R$ :

$$E_{eq} = E^0 + \frac{RT}{zF} \ln \frac{a_O}{a_R} \quad (2.4)$$

Since  $E^0$  is only defined at standard conditions, the formal potential  $E^{0'}$  expresses the value for a fixed set of experimental conditions, which results in Equation 2.5 with the bulk con-



centration of reactive species  $c_O$  and  $c_R$  [36, 38, 46, 47].

$$E_{eq} = E^{0'} + \frac{RT}{zF} \ln \frac{c_O}{c_R} \quad (2.5)$$

### 2.1.4 Electrode kinetics

For a process described by the Nernst equation at equilibrium, no net reaction is taking place at the electrode surface. If the electrode is polarized by changing the potential, the reaction will occur in either the anodic or cathodic direction. This deviation from the equilibrium potential is called polarization. The magnitude of polarization is expressed as overpotential  $\eta$ . This is defined as the potential difference between the expected equilibrium potential  $E_{eq}$  and the potential  $E$  at which the redox reaction is observable as given in Equation 2.6.

$$\eta = E_{eq} - E \quad (2.6)$$

For any non-spontaneous electrochemical reaction, this overpotential is required to overcome the potential barrier at the electrode/electrolyte interface with the reaction rate being dependent on the overpotential. The relationship between the overpotential and the current  $I$  can be described by the Butler-Volmer equation, the basic equation for electrochemical kinetics, with current density  $j$ , area  $A$ , exchange current density  $j_0$  and the transfer coefficient  $\alpha$  [36, 38, 46–48].

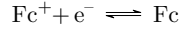
$$j = \frac{I}{zFA} = j_0 \left\{ -\exp \left[ -\frac{\alpha zF}{RT} \eta \right] + \exp \left[ -\frac{(1 - \alpha)zF}{RT} \eta \right] \right\} \quad (2.7)$$

It is important to note that this equation is only valid if the current is limited by the reaction kinetics and not by mass-transfer. Experimentally, this was found to be the case for small overpotentials and high concentrations.

### 2.1.5 Diffusion-limited currents

A common method for obtaining information on an electrochemical system is the application of a perturbing electrical signal and the subsequent observation of induced changes in the system's characteristics. In the case of chronoamperometry, the current is monitored as a function of time upon application of a potential step as perturbation. This method is also the working principle for the electrochemical detection of silver nanoparticles employed in this work.

For the oxidation of ferrocene to ferrocenium, which is often used as reference model [49]:



there is a potential region  $E_1$ , where no Faradaic processes take place. Additionally, there is also a more positive potential region  $E_2$ , where the oxidation of ferrocene features kinetics being so fast that the Fc-surface concentration approximates zero. If the potential is now stepped from  $E_1$  to  $E_2$ , ferrocene is oxidized resulting in a current flow. The initial oxidation has generated a concentration gradient over a certain distance from the electrode surface into the bulk solution. This induces a continuous flux of ferrocene to the electrode surface and the solution volume in which this flux occurs corresponds to the diffusion layer. The flux and therefore also the current correlate proportionally to the concentration gradient at the electrode surface. Due to the continuous flux, the ferrocene depletion zone (thickness of the diffusion layer) increases, resulting in a decline of the slope of the concentration gradient and the current with time [38, 50]. In case of a planar macroelectrode and a diffusion-controlled process  $\text{O} + z\text{e}^- \rightleftharpoons \text{R}$ , the current-time response is given by the Cottrell equation [51] with the current  $I$ , time  $t$ , number of electrons  $z$ , Faraday constant  $F$ , the diffusion coefficient  $D_O$

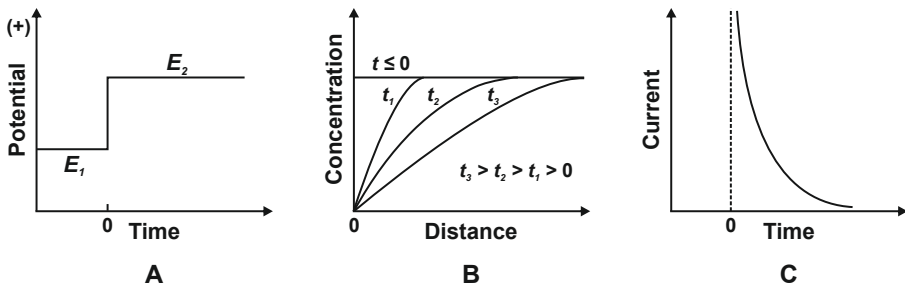


**Figure 2.3:** A) Typical potential waveform for a chronoamperometric step from  $E_1$  to  $E_2$ . B) Concentration profile for varying time points into the experiment. C) Chronoamperometric response (current vs. time), (adapted from ref. [38]).

and the bulk concentration of species O in solution  $c_O$ :

$$I(t) = \frac{zFA\sqrt{D_O}}{\sqrt{\pi t}} c_O \quad (2.8)$$

## Microelectrodes

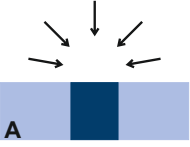
The development of microfabrication techniques in the early 1980s enabled the production of electrodes with micrometre or sub-micrometre dimensions. Such miniaturized electrodes have been termed microelectrodes and are now widely employed for a variety of electrochemical measurements. Although there is no clear definition for microelectrodes, generally two premises have to be fulfilled. They have to be smaller than the scale of the diffusion layer in typical experiments and one dimension, called critical dimension, has to be smaller than  $25\text{ }\mu\text{m}$  [38]. However, a decrease in the geometric dimensions of an electrode is accompanied by a deviation of its behaviour from that of macroelectrodes. Overall, three phenomena can be observed. Firstly, the current density increases. Secondly, in case of dissolved redox molecules the observed current decreases but not proportionally to the electrode area. Thirdly, the mass transport of redox molecules from the bulk electrolyte to the electrode changes from linear to 2- or 3D diffusion, which is an important feature [50, 52–55].

The disc electrode is one of the most commonly used geometries but complicated to describe theoretically due to diffusion in two dimensions. It occurs normal to the plane of the disc and radially with regard to the axis of symmetry resulting in a non-uniform current density. Two limiting cases have to be considered in order to calculate the current at a disc electrode. In case of short time periods, where the critical dimension exceeds the thickness of the diffusion layer, the radial diffusion component is negligible and linear semi-infinite diffusion can be assumed [38]. The time-dependent current for short time periods can be approximated by the Shoup-Szabo equation [56]:

$$I(t) = 4zFc_ODOr \left[ 0.7854 + 0.8862 \left( \frac{4D_O t}{r^2} \right)^{-\frac{1}{2}} + 0.2146e^{-0.7823 \left( \frac{4D_O t}{r^2} \right)^{-\frac{1}{2}}} \right] \quad (2.9)$$

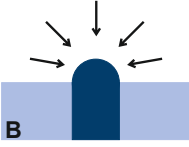
with the current  $I$ , time  $t$ , number of electrons  $z$ , Faraday constant  $F$ , the diffusion coefficient  $D_O$ , the bulk concentration of species O in solution  $c_O$  and the radius  $r$ . For longer time periods ( $t \gg \frac{r^2}{D_O}$ ), the thickness of the diffusion layer is large in comparison to the critical dimension and the current of the microelectrode approximates steady-state or quasi steady-state. The current in this case can be described by the equations stated in Figure 2.4 and depends on the geometry of the electrode [57]. Given are the equations for inlaid disc, hemispherical and recessed disc electrodes with the recess depth  $L$ . The electrode geometries and associated diffusion profiles are as well depicted in Figure 2.4. Microelectrodes feature several practical advantages over larger electrodes such as fast accomplishing

$$\begin{aligned}
 i_{ss} &= 4zFD_Oc_Or & i_{ss} &= 2\pi zFD_Oc_Or & i_{ss} &= \frac{4\pi zFc_OD_Or^2}{4L + \pi r} & (2.10)
 \end{aligned}$$



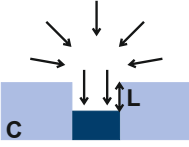
**A**

**Inlaid disc**



**B**

**Hemispherical**



**C**

**Recessed disc**

**Figure 2.4:** Geometries of microelectrodes with corresponding diffusion profiles: A) inlaid disc, B) hemispherical, C) recessed disc.

of steady-state signals, a decreased ohmic drop, short response time and small currents. Additionally, mass transfer is very efficient with rates comparable to those of macroelectrodes. Especially, microelectrode arrays are of great interest for analytical approaches. They show higher signal-to-noise ratios compared to macroelectrodes with an equivalent electrode surface area, which provides lower current detection limits. Furthermore, the rapid accomplishing of steady-state together with fast charging enhance the sensor response time. [38, 50, 54, 55, 58].

## 2.2 Metallic nanoparticles and deoxyribonucleic acid (DNA)

### 2.2.1 Metallic nanoparticles

#### Nanoparticles - general concept

Engineered nanoparticles represent a new class of materials with unique properties. A suitable definition could be as followed: An engineered nanoparticle is any intentionally generated particle with a characteristic dimension between 1 and 100 nm and properties, that are different in comparison to non-nanoscale particles exhibiting the same chemical composition [59]. Whilst nanoparticles exist in a variety of different material compositions and shapes, they all share a universal concept: their properties are closely linked to their atomic-scale structure and nanoscale size [60]. One of the most characteristic features of nanoparticles is their large surface-to-volume ratio, which increases with decreasing particle size. Due to lower coordination with adjacent atoms and more unsaturated sites or dangling bonds, the surface atoms are chemically more reactive in comparison to the bulk. Thus, they can show extraordinary physical properties or interact with their environment. Accordingly, the surface properties have a strong influence on the structural and electronic behaviour and material characteristics such as melting point or magnetic moment can change [60–63]. Different nanoparticle categories

are for example carbon-based, ceramic, semiconductor, polymeric or metal nanoparticles [64]. The following section will be focused on metallic colloidal nanoparticles such as silver or gold colloids.

### **Synthesis, stabilization and functionalization**

In general, nanoparticles can be fabricated by a variety of physical and chemical techniques. Physical procedures often base upon a 'top-down' approach, employing the decomposition of bulk or precursor materials into smaller fragments, which can be converted into nanoparticles. On the contrary, chemical methods mostly rely on 'bottom-up' approaches with nanoparticles formed by the assembly of smaller subunits. This chemical growth usually involves precipitation of a solid phase from solution with a nucleation step followed by particle growth via molecular addition and aggregation [62,64,65]. A scheme of the different synthesis approaches is given in Figure 2.5A. One of the most widely-used synthetic procedure for obtaining metallic nanoparticles is wet chemical reduction. Typically, a metal salt as precursor is dissolved in an appropriate solvent and reduced with a reducing agent such as sodium borohydride, trisodium citrate or others [63,65–67]. At large, the synthesis is performed in presence of protective agents or ligands, complying with two different tasks. Firstly, they control the nanoparticle growth with regard to rate, final dimension or geometric shape. Secondly, they protect nuclei and larger nanoparticles from aggregation via repulsive forces, which can be induced for example by electrostatic repulsion. A prominent example for this electrostatic stabilization represent citrate ions, which serve as reducing agent at the same time. Another possibility for stabilization is the introduction of bulky molecules such as polymers like polyvinylpyrrolidone, which generates steric hindrance [60,65,68]. Figure 2.5B shows a schematic illustration of both stabilization principles. A prerequisite for stabilization is the surface attachment of the ligand molecules via attractive interactions like chemisorption, electrostatic attraction or hydrophobic interaction. Mostly, the attraction is introduced by a functional head group of the ligand, which features affinity to inorganic surfaces. This concept of affinity-based attachment can also be employed for exchanging the ligand molecules on the nanoparticle surface in order to further improve the stability or introduce new properties. A good example for this exchange are silver nanoparticles produced by citrate reduction in aqueous solution. The negatively charged citrate ions are adsorbed on the nanoparticle surface, providing stabilization via electrostatic repulsion. When stored in the synthesis solution, the nanoparticles might be stable over years. This changes drastically, for example upon addition of salts. The electric field stabilizing the particles is shielded in the presence of high salt concentrations, which allows the nanoparticles to approach each other. At some point the attractive forces, like Van der Waals force or hydrogen bonds, cause reversible agglomeration or irreversible aggregation of particles [68–70]. In order to prevent aggregation and particle ripening, the citrate layer can be exchanged by stronger binding ligands. Suitable candidates are ligands containing

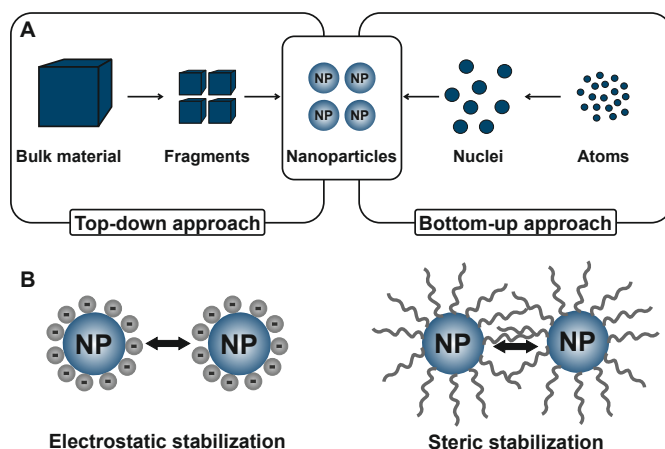


**Figure 2.5:** A) Scheme of top-down (left) and bottom-up (right) approach for the synthesis of nanoparticles. B) Nanoparticle stabilization with ligand molecules via electrostatic repulsion (left) and steric repulsion (right).

a thiol group, which exhibits high affinities comparable to covalent binding for noble metal surfaces (especially gold) [71]. In comparison to self-assembled thiolate monolayers (SAMs) on planar crystal faces [71–73], the process for nanoparticle surfaces gets more complicated. Reason for this are binding sites differing in affinity for the ligands due to the presence of a variety of different crystal facets along with an increased fraction of terraces, edges and vertices. This, together with the ligands being able to diffuse on the particle surface, renders the characterization of the ligand shell and therefore the nanoparticles themselves rather complicated [68, 74].

### Electronic and optical properties

As mentioned before, a decrease in size and dimensionality of a material has strong influence on its properties and characteristics. Especially, the electronic properties vary radically with decreasing size due to a decrease in the density of states and a spatial restriction of the electronic motion. The stationary states are now dictated by the boundaries of the system, resulting in surface effects becoming paramount. In the nanometre to sub-nanometre size regime, the bulk band structure disappears and discrete energy levels appear [60, 76]. The unique optical properties of nanoparticles are in close relation to their electronic structure. They originate from the collective oscillation of the conduction-band electrons upon interaction with the electromagnetic field of incident light. This phenomenon is termed localized surface plasmon resonance (LSPR), which is a characteristic property of metallic nanoparticles. In general, a combination of three factors leads to this oscillation. Firstly, the conduction-

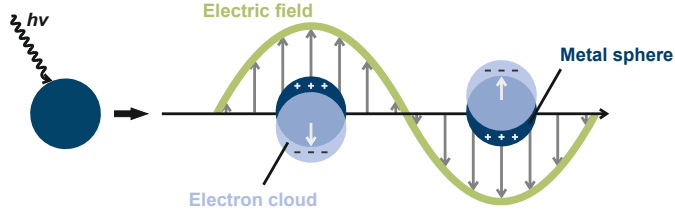


**Figure 2.6:** Schematic illustration of a localized surface plasmon, adapted from ref. [75].

band electrons are accelerated by the electromagnetic field of incident light. Secondly, the displacement of the electron cloud relative to the ionic cores results in a restoring force due to the Coulomb attraction between the ionic cores and the electrons. Thirdly, the electrons are confined to dimensions much smaller than the incident wavelength [75–78]. The plasmon resonance can be observed as strong absorption band in a spectrum, when the frequency of the electromagnetic field is resonant with the collective electron motion. Size, shape and the dielectric properties of the metal nanoparticle as well as of the surrounding medium strongly influence the width and the frequency of this absorption. Noble metals such as gold, silver and copper exhibit distinct absorption bands in the visible range, which is the origin of their bright colours (red (Au, Cu), yellow (Ag)) [76, 79, 80].

## 2.2.2 Deoxyribonucleic acid (DNA)

### Structure and function

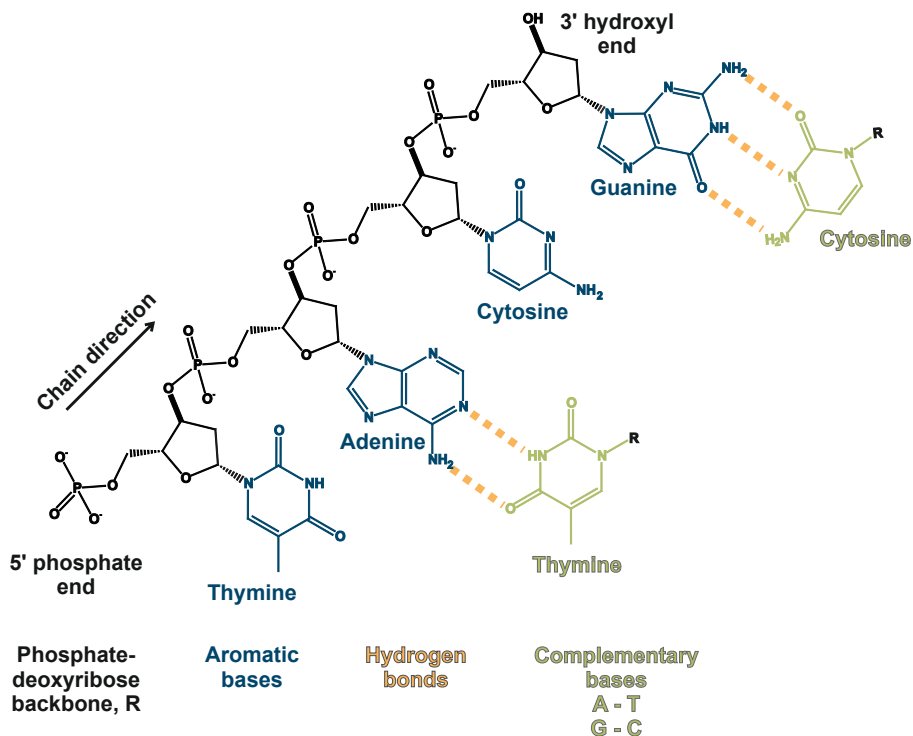


**Figure 2.7:** Chemical formula of the DNA structure with the phosphate-deoxyribose backbone (black), aromatic bases (blue), Watson-Crick base pairing via hydrogen bonds (orange) and the complementary bases A-T, C-G (green) with residual DNA structure R.

Deoxyribonucleic acid (DNA) is a linear polymer, consisting of nucleotides as monomeric unit. The linear arrangement of the four naturally occurring nucleotides is the critical feature, encoding all the genetic information required for the development of complex life form. Overall, the DNA is composed of three components: heterocyclic aromatic bases, ribose sugars and phosphate groups. The chemical formula of a single strand of DNA is given in Figure 2.7 (black, blue). A  $\beta$ -glycosyl linkage connects the bases with the cyclic sugar (deoxyribose for DNA, ribose for RNA) forming a nucleoside. Upon phosphorylation of the 3'- or 5' sugar hydroxyl group, a nucleotide is generated, which can be found in DNA, RNA and various energy carrier molecules. Within the nucleotides, the pyrimidine (Thymine, Cytosine) and purine (Adenine, Guanine) bases act as genetic information molecules. Reason for this is



their unique structural identity, provided by a differential positioning of hydrogen bond acceptor and donor groups. The carbonyl oxygen and the nitrogen in the ring act as hydrogen bond acceptors, whereas the hydrogen atoms of the amino groups serve as donor groups. Additionally, due to their aromatic nature the bases are rigid planar molecules. Another important feature of a polynucleotide is a strand polarity with two distinct ends named 5' and 3' and new nucleotides are introduced in 5' to 3' direction (indicated by a black arrow in Figure 2.7) [81,82].

One of the most crucial features of DNA is the organization into a right-handed double helix as described first by Watson and Crick in 1953 [83] with two individual DNA strands aligned in an antiparallel manner. The strands stick together because of the afore mentioned hydrogen bonds between the individual bases with a strict complementary base pairing (A-T, G-C) as depicted in Figure 2.7. Furthermore, the flat bases are stacked uniformly close to the centre of the cylindrical helix due to Van der Waals forces and hydrophobic interactions. Consequently, the phosphate and sugar groups are located on the outside of the helix, providing a backbone. In this configuration, the atoms of the bases and thus the encoded information are physically shielded from any chemical modifications caused by environmental influences. The dimensions of a classical right-handed helix can be approximated as 2.0 nm in diameter and a helix pitch of 3.6 nm with 10.5 base pairs per turn [81,82].

### DNA hybridization

The structure of the double helix is exceptionally stable due to the combination of base pair stacking and hydrogen bond interactions together with solvation in solution. Therefore, a dissociation of the DNA into single strands requires adequate treatment to overcome these forces. One possibility is incubation at very high or low pH values, where the stacking is destabilized by ionization of the bases. Additionally, the double helix can be dissociated by increasing the temperature, with the melting temperature  $T_m$  defined as the temperature at which 50 % of the sample is dissociated [81].  $T_m$  is characteristic for the respective helix and increases with length and GC/AT ratio of the polynucleotide. Furthermore, it is influenced by the ionic strength of the medium and the presence of metal ions such as  $Mg^{2+}$ , which increases duplex stability. The reformation of the helical structure by hydrogen bond interactions of complementary base pairs on the single DNA strands is commonly referred to as hybridization and follows a cooperative zipper mechanism. A scheme of this mechanism is depicted in Figure 2.8A. If complementary sections on the two opposing DNA strands come in close contact, a base pair can form. However, this isolated base pair is fairly unstable and can dissociate easily. The stability increases with the formation of a second adjacent base pair. Three base pairs together constitute an appropriate nucleus acting as starting point for further base pairing or zipping of the remaining bonds. The overall transition can be considered as all-or-nothing process (two-state model). The polynucleotides exist solely either as

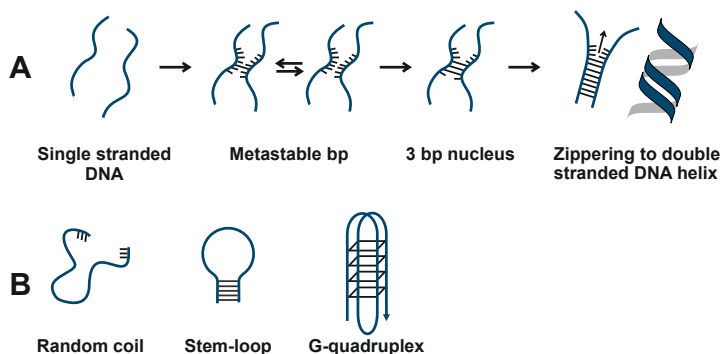


**Figure 2.8:** A) Scheme of cooperative zipper mechanism for DNA hybridization, bp = base pair, B) common motifs of single stranded DNA secondary structure.

dissociated, coiled monomers or in their completely associated double helical form, in which only the terminal base pairs dissociate and associate rapidly [82,84].

The mentioned mechanism for DNA hybridization depends strongly on the initial conformation of the single DNA strands and might change if the monomers don't exist as random coils anymore but feature a secondary structural motif. Such a motif forms in case of two or more self-complementary sections within a single DNA strand, resulting in intrastrand base pairing [84–88]. Common secondary intrastrand structures are stem-loop (also called hairpin) [89] or g-quadruplex [90,91] conformations as shown in Figure 2.8B. Additionally, hybridization rates decrease for surface-immobilized DNA strands in comparison to identical experiments carried out in solution [86].

DNA hybridization is a very specific molecular recognition process, which can be exploited for a variety of different tasks. In molecular biology it serves as extremely powerful tool amongst others for DNA analysis, for example in polymerase chain reactions (PCR) [92] or DNA microarrays [93]. Additionally, DNA sequences can be used as programmable objects for the controlled molecular self-assembly of DNA nanostructures, such as DNA origami or as templates for the assembly of inorganic materials such as nanocrystals [94–97].

### 2.2.3 DNA functionalized metallic nanoparticles

The use of nanomaterials for diagnostic applications such as the detection of DNA or protein markers had strong influence on the field of biosensing and facilitated the development of novel platforms and methods for the specific detection of bioanalytes. Key features have been advancements in nanomaterial synthesis and characterization, enabling precise control of their properties. Additionally, improved surface modification and engineering methods provided

strategies for functionalization with a variety of ligand classes in order to tune binding affinities and target specificity [98–100].

An important concept is the conjugation of biomolecules to inorganic nanoparticles, also termed bioconjugation. Gold and silver nanoparticles are commonly conjugated to DNA by a ligand exchange with thiol-modified DNA strands as described by Mirkin and co-workers [97]. Such functionalized oligonucleotides generated by solid-phase synthetic procedures are commercially available. For the modification, the nanoparticles are usually mixed with an excess of oligonucleotides bearing an alkyl-thiol group on one end. The DNA binds spontaneously to the metal surface and unbound strands are separated by centrifugation and removal of the supernatant. The resulting DNA-nanoparticle conjugates are soluble in aqueous solution and exhibit long-term stability [68,101]. An important aspect to consider is the possibility of non-specific binding of the nucleotide bases to the nanoparticle surface. The interaction can be ascribed to the binding of the amines in the pyrimidine and purine rings of the nucleotide bases and has been evaluated in detail for gold and silver. In case of silver, cytosine binds the strongest with the following order for the individual bases:  $C > G > A > T$  [102]. For gold, the order is  $A > C > G > T$ , with the affinity of consecutive adenine nucleotides (polyA) being comparable to that of thiol chemisorption [103,104]. Several methods have been reported in order to reduce the non-specific adsorption. Possible approaches are DNA adsorption followed by a subsequent treatment with mercaptohexanol or enhancement of the DNA surface density. This will displace the non-specifically bound strands, since the non-specific interactions require a larger surface area [101,105]. The surface density in general can be controlled via adjustment of the excess ratio or by dilution with other (shorter) strands [106]. In addition, also the electrolyte concentration during the modification step has influence on the surface density. Reason for this is a screening effect of the negatively charged backbone, which allows a more compact strand packing [107,108]. Instead of eliminating non-specific interactions of the individual DNA bases, the effect can also be exploited for a thiol-free DNA conjugation to gold. The DNA sequences are designed with a polyA anchoring sequence, a vertical T spacer and the capture sequence complementary to the DNA probe. The polyA anchor preferentially binds to the gold surface while at the same time blocking nearby adsorption sites due to a larger 'footprint' compared to thiol groups. As a consequence, non-specific interactions of other sequences are suppressed and the strand adopts an L-shaped conformation, which is beneficial for DNA hybridization [109,110]. In general, DNA hybridization of surface immobilized probes and solution phase oligonucleotides was found to be more complicated and sensitive to external effects when compared to hybridization in solution. Parameters such as strand density, surface charge, DNA length or the flatness of the substrate can have strong influence on stability and kinetics of DNA hybridization and have to be considered for nanoparticle based hybridization assays [106,111–113].

## 2.3 Stochastic nanoparticle impact electrochemistry

Metallic nanoparticles have gained increasing attention due to their unique chemical and physical properties, which can be substantially different compared to those of the bulk material. Especially, their high surface-to-volume ratio, size and shape-dependent optical and electronic properties and a high density of active sites resulted in widespread technical applications such as in sensors, catalysis, optical or biomedical applications [114, 115]. However, it is still necessary to find ways for nanoparticle characterization and an improved knowledge of their structure-function relationship. Notably, a comprehensive understanding of the electrochemical interface in combination with related reactions and kinetics at the nanoscale are considered to have great influence on future applications [116].

In recent years, stochastic collision based electrochemical measurements have demonstrated great potential for the characterization of individual nanoparticles and the investigation of their kinetics and thermodynamics [11, 12, 117]. Generally, stochastic electrochemistry describes a group of electrochemical experiments, where the charge or current related to a random discrete event is monitored at an electrode surface as a function of time, concentration or electrode size [118]. This is in contrast to the nearly constant response of bulk or ensemble measurements, where the characteristics of individual events are usually masked [5, 117, 118]. However, single nanoparticle measurements are challenging due to the difficulties of delivering, locating and typifying an individual nanoparticle at a nanoscale interface. Furthermore, the current response associated with a single nanoparticle is typically small and ultrafast and thus hard to detect accurately. Therefore, a single nanoparticle detection scheme usually requires microelectrodes for a reduction of the background current noise in combination with high-bandwidth and low-noise electrochemical measurement equipment. Additionally, the electrode dimension (larger than the particle) and the nanoparticle concentration have to be adjusted to ensure only one collision in a certain time interval while at the same time measuring a sufficient number of responses for valid data analysis [117, 118]. The main information that can be extracted from the response is: 1) the event frequency at the electrode, 2) the current magnitude in an event and, 3) the current shape vs. time in relation to experimental parameters [118]. In the following, an overview of different types of experiments and the underlying concepts is given.

### 2.3.1 Overview of different types of impacts

Since the first report of a stochastic electrochemistry experiment by Lemay in 2004 [119], the field has developed rapidly and several methods have been introduced. Most of them use amperometry to monitor the response, however with different types of impacts under observation [2]. Herein, the focus lies on electrode/particle impacts with a Faradaic response, which can be divided into three main categories: blocking, mediated Faradaic and Faradaic impacts and will be illustrated in greater detail. Additionally, experimental procedures based on capacitive [120] or enzymatically enhanced impacts [121,122] have been reported as well as measurements in vesicles, droplets or micelles as confined volume [123–125].

#### Blocking impacts

The blocking experiment is based on the observation of a decrease in electrode area (blockage) upon collision of an insulating particle. As background, a heterogeneous redox reaction of solution phase redox reporters is performed at the electrode. The collision of an insulating particle leads to a decrease in the surface area of the electrode and thus the flux of the redox reporter to the electrode is disrupted. As a result, a step-wise reduction of the diffusion limited current of the redox species can be observed with the step height correlating to the size of the nanoparticle [2,12]. Figure 2.9 shows a schematic representation of the experiment with the corresponding step-like amperometric response. This type of experiment was pioneered by Lemay *et al.* in 2004, where they demonstrated the amperometric detection of single carboxylated micro- and nanospheres as discrete steps in the current-time response [119].

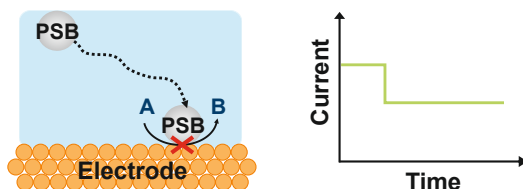


**Figure 2.9:** Scheme of blocking impacts with a decrease in electroactive electrode area upon collision of a polystyrene bead (PSB) with the electrode and the corresponding step-like amperometric response (adapted from ref. [2]).

### Mediated Faradaic or electrocatalytic impacts

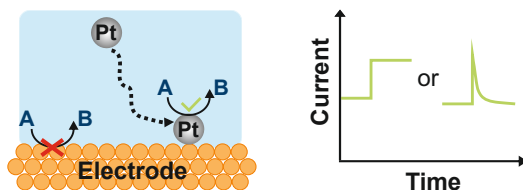


**Figure 2.10:** Scheme of mediated Faradaic impacts via electrocatalytic amplification with the catalytic reaction taking place upon collision of a Pt nanoparticle with the electrode and the corresponding step- or spike-like amperometric response (adapted from ref. [2]).

The mediated Faradaic experiment exploits material related differences in heterogeneous kinetics. The particle itself does not undergo any redox reaction but can catalyse one. Practically, this means the reaction under observation does not occur at the electrode, either due to an inert material or kinetic limitations related to the electrode potential. However, the surface can still perform electron transfer to a colliding nanoparticle. Once the nanoparticle collides, it adopts the electrode potential facilitating a reaction at its surface, which results in a current response. The shape of the amperometric current response depends on the nature of the nanoparticle/electrode contact. A current spike can be observed for a short contact time either due to the particle leaving the electrode or a decrease in catalytic activity. In case of long-term particle adsorption, the reaction at the nanoparticle surface takes place continuously resulting in a current step [2, 12, 118]. Since the particle leads to an increase in electroactive surface area the radius of the nanoparticle is correlated with the amplitude of the current step [126]. Figure 2.10 shows a schematic representation of the experiment with the corresponding step- or spike-like amperometric response. This method was developed by Bard et al. using an inert carbon fibre electrode in acidic solution in combination with catalytically active platinum nanoparticles. For example, for proton reduction the reaction is rapid on platinum but sluggish on carbon. Accordingly, when the electrode is biased to a potential range where proton reduction emerges solely on platinum, an alteration in the amperometric response can be recognized upon collision of a nanoparticle with the electrode [127, 128].

## Direct Faradaic or material dissolution impacts

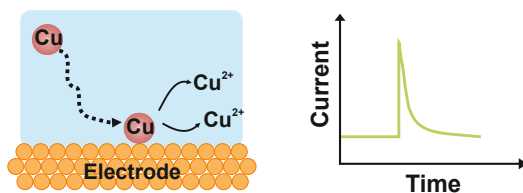


**Figure 2.11:** Scheme of material dissolution impacts with oxidation and resulting dissolution of a Cu nanoparticle upon collision with the electrode and the corresponding spike-like amperometric response (adapted from ref. [2]).

The direct Faradaic approach is based on a direct electron transfer between the electrode and the particle resulting in a redox reaction. In practice, the electrode surface is biased at a potential where the colliding nanoparticle is either oxidized or reduced. This process leads to a spike-like Faradaic response. In case of material dissolution, potential soluble products will diffuse away. Due to the high packing density of metal atoms the obtained signal response can be very large giving rise to a high signal-to-noise ratio. In case of complete oxidation (or reduction) of the nanoparticle, the overall charge transferred during the event can be related to the number of atoms constituting the nanoparticle via Faraday's first law. Thus, the nanoparticle size can be calculated with the integral under the current peak. [2,12,29,126]. Figure 2.11 shows a schematic representation of the experiment with the corresponding spike-like amperometric response. This method was first reported by Compton and co-workers for the oxidation of single silver nanoparticles [129,130]. Later the method was expanded to different nanoparticle materials such as copper [131].

In summary, all of the above mentioned impact methods allow for single nanoparticle detection with the capability of sizing of the nanoparticles. Additionally, direct impacts also enable identification of the material, based on the particular material-dependent redox potential. On the contrary, indirect methods only permit discrimination between electrocatalytic and comparatively inert materials. The fact that this holds true for a variety of different materials could induce adverse responses originating from other electroactive species present in the sample. With the redox potential as characteristic feature of the respective nanoparticle material under investigation, direct impacts are less predispositioned to false positive results and fouling of the system [2,126].

## 2.3.2 Behaviour of individual nanoparticles at the nano-interface

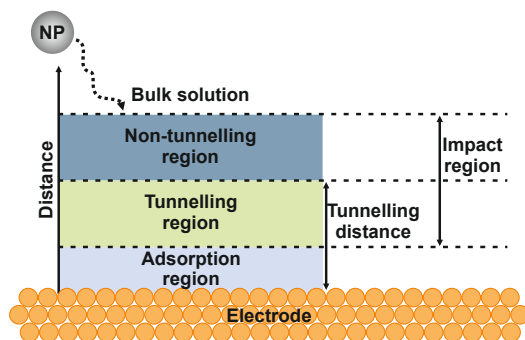


**Figure 2.12:** Theoretical model of the space above an electrode with segmentation into four different zones: the bulk solution, a non-tunnelling region, a tunnelling region and the adsorption region (adapted from ref. [132]).

A typical stochastic nanoparticle impact experiment consists of an electrode immersed in an electrolyte solution and a nanoparticle dispersion. This dispersion can either be premixed with the electrolyte solution or injected during the measurement. In general, the motion of an individual nanoparticle towards the surface of an electrode and a subsequent nanoparticle-electrode interaction are complex processes [117]. The dominating mass transport to the electrode for redox molecules in an electrolyte solution at room-temperature is based on diffusion, occurring due to random Brownian motion. However, depending on the experimental parameters other aspects such as migration due to electrical fields have to be considered [133]. In case of only taking Brownian motion into account, the diffusion coefficient of the particle in the bulk solution is constant and isotropic. However, when the nanoparticle approaches an interface such as the electrode/electrolyte interface to a distance comparable to its radius, the diffusion coefficients become anisotropic. Especially, the diffusion coefficients perpendicular and in plane parallel to the interface decrease in comparison to the bulk value. Furthermore, they are now depending on the distance of the nanoparticle to the interface [134–136]. This phenomenon, referred to as 'near-wall hindered diffusion' or 'hindered diffusion', slows down the particle motion with a full suppression of the perpendicular Brownian motion in direct proximity of the interface. As a result, the average residence time near the electrode is elongated [132, 137]. Figure 2.12 depicts the theoretical model of the space above an electrode with segmentation into four different zones being important during the course of a nanoparticle impact. The furthest region from the electrode is the bulk solution, where nanoparticles are not participating in any impacts. Here, with closer distance to the electrode the afore mentioned near-wall hindered diffusion comes into account. Upon further approaching the electrode, particles enter into the impact region, which is subdivided into two regions. In the non-tunnelling region (blue), the particles are Faradaically inactive but



still considered as impacting. This region is outside of the tunnelling distance, which can be described as the maximum distance to the electrode where charge transfer tunnelling is still possible. In nanometre range proximity to the electrode the tunnelling region (green) begins, in which the nanoparticles couple to the electrode and adopt the electrode's potential. This enables a Faradaic charge transfer, which contributes to the overall current of the electrode. In the region in direct vicinity to the electrode surface, which is defined as the adsorption region (grey), the particles either are adsorbed permanently while still mediating a Faradaic current or are removed from the electrode by diffusion [132, 137]. The resulting current is distance dependent because the charge transfer rate decreases exponentially with increasing electrode-particle spacing [114, 138]. Additionally, the reaction kinetics as defined by the Butler-Volmer equation and the diffusion-controlled transport of reagents and products may have an influence on the current [139, 140].

## 3 Materials and methods

### 3.1 Microelectrode array

In this work, Microelectrode Arrays (short MEA) were employed. The production was performed by technicians in the cleanroom of the Helmholtz Nanoelectronic Facility of the Forschungszentrum Jülich, following standard cleanroom protocols.

#### 3.1.1 MEA composition and layout

The general production process of the microelectrode arrays can be divided into three steps. First, the electrode layout and the feedlines are patterned via standard photolithography followed by metal deposition. For this, a 20 nm thin Ti layer followed by a 200 nm Au layer and another 10 nm Ti layer are deposited via electron beam evaporation onto a borosilicate wafer as substrate. Afterwards, the passivation layer is introduced. This layer consists of a stack of alternating silicon oxide (O) and silicon nitride (N) layers (together ONONO) and a  $\text{Ta}_2\text{O}_5$  top layer fabricated via atomic layer deposition (ALD). In the last step, the electrodes and bondpads are opened via photolithography and reactive ion etching. A simplified schematic of the different steps is shown in Figure 3.1. The detailed description of the fabrication process is given in the Appendix on page 99. Every individual MEA chip has a size of  $24 \times 24 \text{ mm}^2$ . The chip layout is depicted in Figure 3.2. The square sensor area in the centre is connected via metallic feedlines with the bondpads at the edge of the chip. The bondpads are metal-pads without passivation, allowing top contact connection with external electronics. The sensor

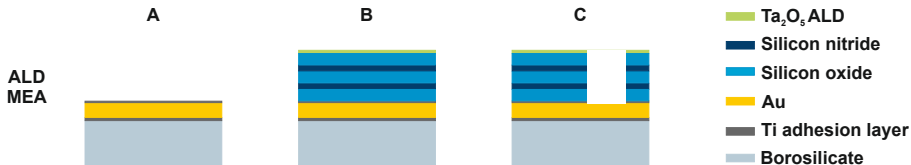


**Figure 3.1:** Simplified schematic of the different fabrication steps of MEAs. **A)** Metal deposition, **B)** passivation layer, **C)** electrode opening.

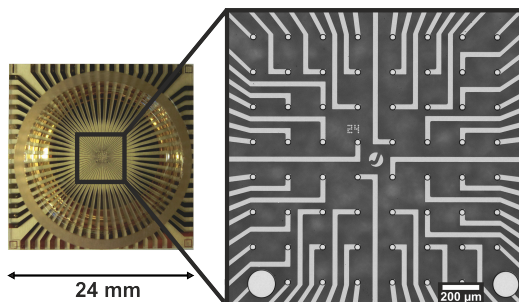


**Figure 3.2:** Picture of a MEA chip with glass ring on top and zoom in the square sensor area in the centre.

area has a size of  $1.4 \times 1.4 \text{ mm}^2$  with 64 equidistant electrodes. They are arranged in an  $8 \times 8$  layout grid with a distance of  $200 \mu\text{m}$  in between (see Figure 3.2). The diameters of the electrodes employed in this thesis were  $12 \mu\text{m}$ . The two large electrodes in the bottom right and left corner with a size of  $140 \mu\text{m}$  serve as benchmark electrodes. Optical characterization was performed with a standard up-right microscope (microscope: Axioplan 2 Imaging + Camera: AxioCam MRc 5 Zeiss-Oberkochen, Germany). The chips were inspected for impurities, residues and defects in the passivation or metallization. In addition, the radius of the electrode openings was checked. Prior to experimental usage the chips were cleaned by subsequent ultrasonication in acetone, isopropanol and water for 5 min to remove fabrication residues. A glass ring with a height of 5 mm and a diameter of 17 mm serving as reservoir for the electrolyte was glued onto the chips with polydimethylsiloxane (PDMS) from Sylgard 184, Dow Corning GmbH (Wiesbaden, Germany). Afterwards the chips were cured for 1 h at  $110^\circ\text{C}$ . To assure a clean surface the chips were treated with oxygen plasma using a Pico low-pressure plasma system (Diener electronic GmbH + Co. KG, Ebhausen, Germany). The parameters were 80 W and a pressure of 0.5 mbar for 3 min. Afterwards the samples were immersed in isopropanol for 10 min for reduction of the formed oxide layer.

### 3.1.2 Electrochemical characterization

All electrochemical experiments were performed using a potentiostat CHI1030B from CHI Instruments (Austin, USA). All data evaluation was performed with Python.

#### Potentiostat setup

A potentiostat is an electric instrument, which controls the voltage between a working electrode (WE) and a reference electrode (RE) in an electrochemical cell. This control is realized

by current injection into the cell via a counter electrode (CE). A simplified circuit diagram of a potentiostat is given in Figure 3.3.

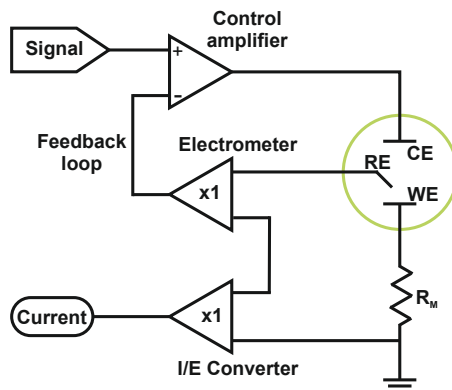


**Figure 3.3:** Simplified circuit diagram of a potentiostat with 3 electrode setup (adapted from ref. [141]).

The control amplifier keeps the potential difference between the WE and the RE at a defined value by regulating the current flow between the WE and the CE. The control is realized by a negative feedback mechanism, which enables regulation of any perturbations. The electrometer determines the potential difference between the WE and the RE. The ideal characteristics are infinite input impedance and zero input current. The current in the cell is detected by the I/E converter, which forces the cell current to flow through a current-measurement resistor  $R_M$  [141].

All experiments were performed with a 3-electrode setup. The electrodes of a MEA chip served as WE, a coiled Pt wire as CE and a Micro Dri-Ref-450 Ag/AgCl Reference Electrode (SDR2, World Precision Instruments, Sarasota, Florida) as RE. All potentials are given with respect to Ag/AgCl as reference electrode.

### Cyclic voltammetry (CV)

Cyclic voltammetry (CV) is a dynamic measurement technique and commonly used for the investigation of redox processes. It is employed to obtain insight into the thermodynamics of redox processes and the kinetics of charge transfer reactions. Furthermore, it serves as indicator for electrode quality and can measure the electrochemical real surface area [38,142]. Experimentally, a linearly changing potential is applied to the working electrode and the current recorded as function of the potential.

#### Redox probe:

Cyclic voltammetry was performed with 600  $\mu\text{M}$  1,1'-ferrocene dimethanol as redox probe in 300 mM KCl electrolyte. The potential was swept linearly between -0.2 and 0.6 V as switching potentials with a scan rate of 100 mV/s.

#### Sulfuric acid:

For this CV experiment, 50 mM  $\text{H}_2\text{SO}_4$  was used as electrolyte and the potential was swept linearly between 0 and 1.45 V as switching potentials with a scan rate of 100 mV/s.

## 3.2 BioMAS measurement device

The measurement device used for the current recordings in this thesis is called **Bioelectronic Multifunctional Amplifier System**, short BioMAS, and was developed and built in-house. The system consists of a main amplifier in combination with a modular pre-amplification headstage which is connected to a microelectrode array as depicted in Figure 3.4. One major benefit of this configuration is a first amplification with the headstage directly at the signal source (MEA electrode). A detailed description of the main components will be given in the following sections.



**Figure 3.4:** Picture of the BioMAS measurement setup consisting of the main-amplifier (top) and the pre-amplification headstage (bottom, black) including a MEA with electrolyte and reference electrode (green center).

### 3.2.1 Pre-amplification headstage 'Pico Amp'

The pre-amplification headstage used for the experiments is a transimpedance amplifier called picoAmp64III.1. A transimpedance amplifier is a classical feedback configuration for the sensing of current and a subsequent conversion into voltage [143]. The main components are a low-noise operational amplifier (op amp) (OPA129U, Texas Instruments Inc., Dallas, United States) and a  $1\text{ G}\Omega$  feedback resistor ( $R_{fbr}$ ), resulting in a transimpedance of  $1\text{ mV/pA}$ . The inverting input of the amplifier is connected to an electrode of a MEA (working electrode) via the metallic contact pad. The electrode itself is coupled to the potential reference point. This point is defined by a DRIFREF-2 Ag/AgCl Reference Electrode (World Precision Instruments, Sarasota, United States) immersed in the electrolyte solution on the MEA and connected to the zero point of a low-noise power supply. Additionally, the circuit allows for the application of a bias voltage to the working electrode. The non-inverting input is connected to the same reference point and set to the bias potential applied to the electrode. Overall, the feedback resistor  $R_{fbr}$  couples the inverting input with the output. Because of this feedback topology the current appearing at the inverting input will be countered by the amplifier. In order to get this current, the voltage between ground and output is measured and the original current can be obtained via recalculation with the transimpedance value. The input capacitance  $C_{input}$  corresponds to a complex component consisting of contributions from the electric circuit, conductor board, amplifier and to the largest extent from the electrochemical cell (MEA, electrolyte, reference electrode). The equivalent circuit of such a transimpedance amplifier is depicted in Figure 3.5. In the headstage, 64 individual amplifiers are combined for simultaneous recordings of 64 channels. Therefore, it is possible to record at all electrodes of a MEA at the same time. In order to suppress external noise, the headstage features an aluminium shielding. Additionally, all measurements are performed within a grounded Faraday cage that is mounted on top of an anti-vibration table.

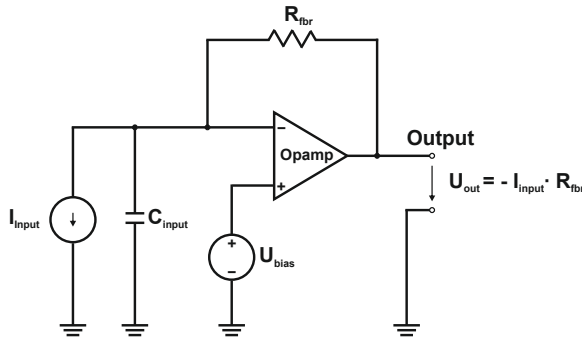


Figure 3.5: Simplified equivalent circuit diagram of a transimpedance amplifier.

### 3.2.2 Main-amplifier

After the first amplification stage within the headstage the signal output is transferred to the main amplifier. Here, the signal can be post-amplified by a factor of 1, 10 or 100 corresponding to overall transimpedance values of 1 mV/pA, 10 mV/pA or 100 mV/pA. Afterwards, the amplified signal is loaded into an analogue-digital-converter (ADC) (USB-6255 DAQ, National Instruments, Austin, USA) with a 16-bit resolution and a maximum sampling frequency of 1.25 MHz. In a typical experiment, a sampling rate of 10 kHz per channel is used. Finally, the signal is transferred to a personal computer via a fibre optic coupler. This ensures galvanic separation of the computer and the measurement setup. The measurement parameters and data monitoring and recording are controlled with an in-house program written in LabVIEW 2016 (National Instruments, Austin, USA) (see Figure 3.6).

### 3.2.3 General measurement procedure

Prior to every measurement set, the MEA chips were rinsed three times with isopropanol and purified and deionized water, followed by drying with nitrogen. Afterwards, the chip was placed onto the holder and the reservoir filled with electrolyte. The electrolyte composition and nanoparticle concentration varied for different experiments with the details given in the corresponding sections. The final measurement volume was set to 800  $\mu$ l and all concentrations

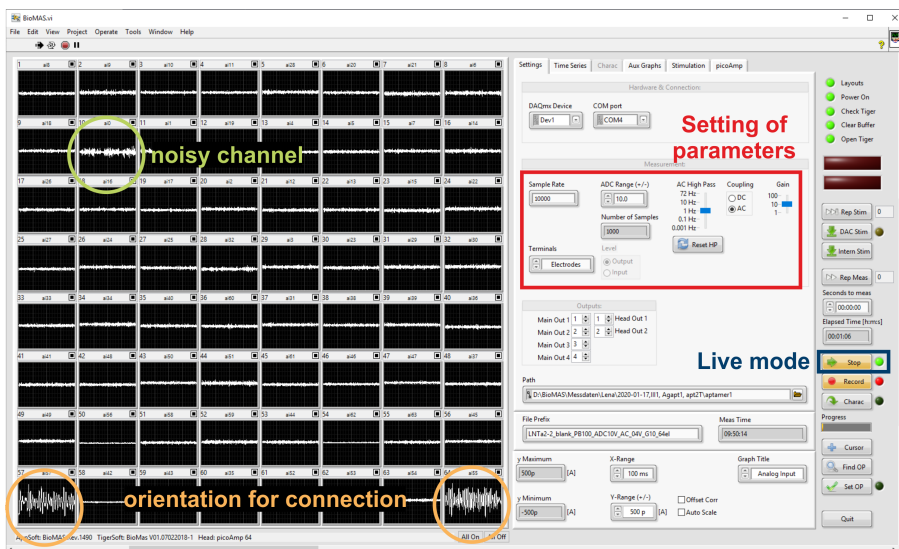


**Figure 3.6:** BioMAS measurement software interface. Parameter settings (red), live mode (blue), noisy channel (green), orientation for connection (orange).

**Table 3.1:** Measurement parameters for current recordings with BioMAS system.

Parameters	
Main-amplifier gain	10
Sample rate	10 kHz
Samples per channel	1000
ADC range	$\pm 10$ V
High pass filter	1 Hz
Y-range	$\pm 500$ pA
Current mode	AC

calculated accordingly. The MEA bondpads were contacted with the headstage and the reference electrode was inserted in the electrolyte and connected to the reference point. A picture of the software interface is depicted in Figure 3.6. The measurement parameters (red) were set as described in Table 3.1. Live monitoring of the current traces (blue) was used as measure for electrical connection with the big electrodes in the lower corners as orientation points (orange). For the actual measurement, live monitoring was activated and a constant potential applied (0-0.8 V as mentioned in the corresponding sections). The recording (and saving) was started and after 10-20 s the nanoparticles were injected into the reservoir with an eppendorf pipette close to the MEA's centre. 40-50 s after the injection, the recording was stopped. Afterwards, the reservoir content was collected and the chip rinsed and dried as described before. In general, a new measurement set was started by recording a current trace without nanoparticles to evaluate the background current noise and ensure good chip performance without artefacts. An example of a noisy channel/electrode is indicated with green in Figure 3.6.



## 3.2.4 Data analysis

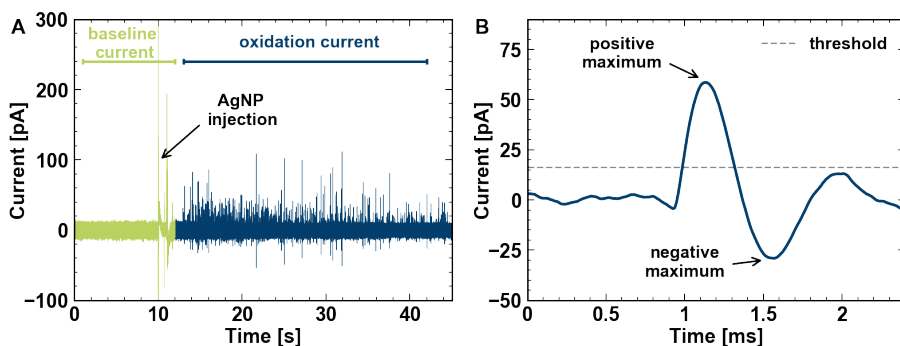


**Figure 3.7:** A) Exemplary current time trace of AgNP oxidation with baseline current (green) used for determination of rms, capacitive peak due to NP insertion (black arrow) and analyzed oxidation current (blue). B) Single oxidation peak with parameters for peak detection. Potential = 0.4 V vs. Ag/AgCl.

For data evaluation the recorded current traces are analyzed with an automated algorithm in MATLAB (Mathworks, Natick, USA) written by our collaborators from TU Munich as reported previously [144,145]. A typical current trace can be divided into three subregions as depicted in Figure 3.7A. In the first 10-15s the background current (noise) is measured in absence of any nanoparticles (green). Afterwards, the nanoparticle solution is inserted generating a large capacitive current spike and a disturbance of the current trace. For data evaluation 2s relaxation time after particle insertion are neglected, followed by 40s recording of the nanoparticle oxidation current with the characteristic current spikes (blue). An exemplary current spike of an impacting nanoparticle is given in Figure 3.7. After the actual peak, a current drop to negative values followed by a second smaller peak can be observed. This is an artefact originating from the design of the electronic circuit and has to be considered for data evaluation. The input impedance of the electrodes can cause an instability in the circuit, causing oscillation of the operational amplifier [146]. The detection algorithm calculates the root mean square (rms) and peak to peak (pk2pk) noise from the current trace before particle insertion and checks for irregular behaviour by evaluation of  $0.5 \text{ median(rms)} < x < 1.5 \text{ median(rms)}$ . Noisy electrodes and those showing no oxidation events are neglected and excluded from further evaluation. The actual peak detection is working with a current threshold of 10-fold rms as lower limit to avoid false positive detection. In order to prevent detection of the ringing artefacts, peaks have to be separated by more than 5ms. Overall, a peak is defined as a positive maximum with a corresponding negative maximum (ringing) within a 5ms time window. Additionally, the accumulated current of each peak is calculated to give the charge according to  $Q = I \cdot t$  with the peak duration  $t$ . Finally, the diameter of the impacting nanoparticle can be derived from Equation 3.1, with the molar

mass of silver  $M_{Ag}$ , density of silver  $\rho_{Ag}$ , Avogadro constant  $N_A$  and the elementary charge  $e_0$ .

$$d = 2 \left( \frac{3}{4\pi} \frac{QM_{Ag}}{N_A e_0 \rho_{Ag}} \right)^{\frac{1}{3}} \quad (3.1)$$

Subsequently, the total number of events can be further processed. Upon dividing the total number of impacts on all active channels by the evaluation time (40s after 2s relaxation time) the average impact frequency per MEA chip is calculated (reference point = 1 MEA chip). The average frequency per electrode is calculated as follows. In a first step, the median of all detected impacts is calculated, followed by normalization to one electrode via determination of the mean and the standard deviation. For this, only the channels with the number of impacts within 50-150 % of the median are considered. Division by the evaluation time results in the average frequency per electrode (reference point = 1 electrode of the 64 MEA electrodes).

### 3.3 Nanoparticle modification and characterization

#### 3.3.1 Preparation of DNA

All DNA sequences used in this work were synthesized by FRIZ Biochem GmbH (Neuried, Germany). All oligonucleotides with a thiol functional group were synthesized with a disulfide protection group with the following chemical formula:  $\text{OH}-(\text{CH}_2)_6-\text{S}-\text{S}-(\text{CH}_2)_6$ , (short: thiol). A summary of the sequences and the respective names is given in Table 3.2. The lyophilized powder was dissolved in purified and deionized water. The concentration of DNA

**Table 3.2:** DNA sequences with respective functional groups and complementary strands labelled as cDNA.

Name	Sequence	Functional group
10mer	5'-AGC TAG TTC C-SH-3'	thiol
13mer	5'-TGC GGA GGA AGG T-SH-3'	thiol
17mer	5'-HS-TTT ACC TGG GGG AGT AT-3'	thiol
20mer	5'-AGC TAG TTC CGT CAT GAT AT-SH-3'	thiol
26mer	5'-HS-TTT TTT TTT TTT TTG CGG AGG AAG GT-3'	thiol
17mer cDNA	5'-ATA CTC CCC CAG GTA AA-3'	none
26mer cDNA	5'-ACC TTC CTC CGC AAA AAA AAA AAA AA-3'	none
30mer cDNA	5'-CTG CCT TGA TCG AAT ACT CCC CCA GGT AAA-3'	none

was determined by measuring the absorbance at 260 nm with the DS-11 FX Spectrophotometer/Fluorometer (DeNovix Inc., Wilmington, United States). Prior to any immobilization the disulfide moieties were cleaved via incubation of equal volumes of DNA and a 5 mM solution tris-(2-carboxyethyl)-phosphine-hydrochloride (TCEP) for at least 1 h.

Folding predictions of possible secondary structures were performed using the Mfold web server (<http://unafold.rna.albany.edu/?q=mfold>) [147], which works with free energy minimization techniques. Based on Watson-Crick base pairing all possible secondary structures are approximated followed by selection of the most thermodynamically stable structures. Predictions were performed for linear DNA at a temperature of 25°C and ionic concentration of 50 mM NaCl. Only folding configurations within 5% from the minimum energy were computed with a maximum number of 50 folds. No limit for the maximum distance between base pairs was considered. The output consists of the predicted secondary structures together with the minimum free energy of the fold.

### 3.3.2 Nanoparticle modification and separation

The silver nanoparticle dispersion was purchased from Sigma-Aldrich Chemie GmbH (Taufkirchen, Germany). Product specifications can be found on the homepage of the supplier [148]. The particles are stabilized with sodium citrate and exhibit a size distribution as stated in the specification sheet of  $10 \pm 4$  nm. The total concentration of silver is given as 0.02 mg/ml, which corresponds to a nanoparticle concentration of 6040 pM. Nuclear magnetic resonance spectroscopy (NMR) of the AgNP citrate stock solution as purchased from the supplier was performed by the staff of ZEA-3 (Central Institute for Engineering, Electronics and Analytics, Forschungszentrum Jülich) on a Bruker Avance 600 MHz (Bruker Corporation, Billerica, United States) measured in D<sub>2</sub>O with water suppression (see Appendix Figure 8.1).

The protocol for the DNA attachment to citrate-capped silver nanoparticles (AgNPs) can be described as a variation of the 'salt-aging' method reported by Mirkin and co-workers [97,108]. This method was used because it exhibits a high reproducibility and is suitable for in principle any DNA sequence [149]. Figure 3.8 shows a scheme of the modification and separation pro-

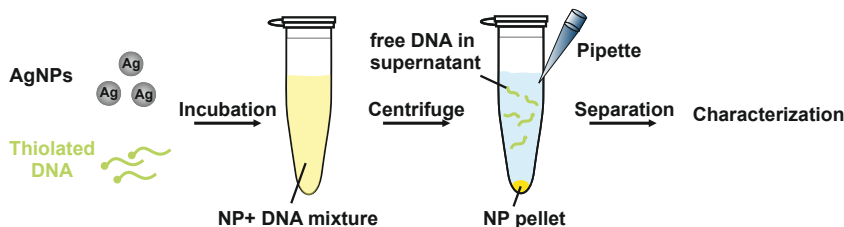


**Figure 3.8:** Scheme of the AgNP-DNA conjugate separation procedure.

cess. For the modification 1 ml AgNPs (diameter 10 nm) was mixed with an excess of DNA (prepared as described in 3.3.1) with AgNPs:DNA ratios between 1:10 and 1:1000. This solution was left for incubation for 24 h in the fridge at 4°C. After incubation the NaCl concentration was adjusted to a final concentration of 0.13 M by adding 1 M NaCl stepwise over a period of 5 days. For the first step, the concentration was only increased to 0.01 M NaCl to be still below the critical coagulation concentration for silver nanoparticles ( $\approx 48$  mM [150]). For the separation of AgNP-DNA conjugates and unbound DNA the mixture was transferred into ultracentrifugation tubes and balanced to a difference below 1 mg. Afterwards the samples were centrifuged with 50.000 rpm for 20 min at 15°C with an Optima MAX-XP tabletop ultracentrifuge (Beckman Coulter GmbH, Krefeld, Germany). The supernatant was carefully collected and the pellet redispersed in phosphate buffer (PBS-50, see Table 3.3) with in total 3 repetitions of the washing process. The nanoparticle samples were stored in the fridge at 4°C until further use. Prior to any measurements the particles were homogenized by ultrasonication for 30 s. The colloidal solutions were stable for about 3-6 months with only a slight decrease in absorption intensity. After longer time periods, the solutions turned clear due to a combination of aggregation and silver oxidation. In order to prevent any interference from these processes, all experiments were performed within four weeks after nanoparticle preparation.

### 3.3.3 UV-Vis spectroscopy

All UV-Vis absorbance measurements reported in this work were performed with a DS-11 FX Spectrophotometer/Fluorometer (DeNovix Inc., Wilmington, United States).

The concentration of AgNP-DNA conjugates was determined by measuring the absorbance at  $\approx 400$  nm, which corresponds to the absorption maximum of the nanoparticles. For the evaluation of the concentration, a calibration curve with known concentrations of the citrate-capped AgNPs was used. The samples were diluted 1:20 with purified and deionized water and measured in a 10 mm path length quartz cuvette (Hellma, Mühlheim, Germany). For a stable modification, the absorbance of the 1:20 diluted samples had to exceed an absorbance of 0.05 in the range of 390-410 nm. For the long-term stability tests, the measurement was repeated after minimum 3 months of storage in PBS-50 at 4°C.

Stability tests in electrolytes with different amount of NaCl were performed with a nanoparticle concentration of 500 pM.

### 3.3.4 Determination of DNA strand density on nanoparticles

The strand density of DNA on the nanoparticles was determined by analyzing the concentration of unbound DNA in the supernatant as reported in the literature [151]. For precise

determination of the DNA concentration calibration curves for known concentrations and 3 repetitions per concentration were measured. The different concentrations were adjusted by diluting the DNA stock solution with PBS-50 (see Table 3.3). Each supernatant from subsection 3.3.2 was measured 3 times and the DNA concentration evaluated with help of the calibration curve. Subtracting the concentration of DNA in the supernatant from the initial concentration allows for the estimation of the amount of DNA conjugated to the particles. The concentration can be converted into the number of DNA strands present in the solution. With the number of AgNPs in the solution, the number of DNA strands per nanoparticle can be calculated. For this, two different methods were applied. Firstly, the DNA concentration was determined by measuring the UV-Vis absorbance at 260 nm with 3 repetitions per supernatant.

The second approach is based on a fluorescence assay with SYBR Green I (SG) as nucleic acid dye. Preferentially, SG binds to double stranded DNA resulting in a fluorescence enhancement. However, it was also reported to bind to single stranded DNA [152] and here the emission fluorescence intensity given in relative fluorescence units (RFU) is used as measure for the DNA concentration. Prior to each experiment set, the SG stock solution (100.000x) was diluted 1:10 with purified and deionized water. The total sample volume was set to 200  $\mu$ l with always 5  $\mu$ l SG (1:10) and 195  $\mu$ l DNA solution. After mixing, the samples were excited with the blue laser ( $\approx$  470 nm) and the emission fluorescence intensity was recorded (Range 1: 514-567 nm, range 2: 565-650 nm, range 3: 665-740 nm). For calculations values in range 2 were used to avoid the emission associated with dsDNA of SG being centred at 520 nm. Each sample was measured at room temperature (RT), at 65°C and again at room temperature after cooling down. Blank measurements were performed with only water, PBS-50 and free SG.

All measurements in this subsection were performed with the DS-11 FX Spectrophotometer/Fluorometer (DeNovix Inc., Wilmington, United States).

#### 3.3.5 Dynamic light scattering and zeta potential

Dynamic light scattering (DLS) and zeta potential were measured employing a zetasizer Nano ZS (Malvern Instruments, Malvern, United Kingdom) with a HeNe laser with a wavelength of 633 nm. Collection of the scattered laser light was performed at a constant angle of 173°. The nanoparticle samples were diluted 1:20 with purified and deionized water and for zeta potentials measurements the NaCl concentration was adjusted to 10 mM. All measurements were conducted at 21°C and repeated two times at 2 min time intervals. Analysis was performed using the instrument software (DTS from Malvern Instruments).

### 3.3.6 Inductively coupled plasma mass spectrometry

Inductively coupled plasma mass spectrometry (ICPMS) of the silver nanoparticles was performed by the staff of ZEA-3 (Central Institute for Engineering, Electronics and Analytics, Forschungszentrum Juelich) in medium resolution mode using a double focussing sector-field ICP-MS Element 2 (Thermo Fisher Scientific, Bremen, Germany). External calibration with Rh as internal standard was used. Microwave assisted chemical extraction was conducted by mixing 100  $\mu$ L of the sample with 400  $\mu$ L  $\text{HNO}_3$  and 100  $\mu$ L  $\text{H}_2\text{O}_2$ . The solution was adjusted to a final volume of 7 ml with ultra pure water. All solutions were measured three times in 1:10 dilution.

### 3.3.7 Scanning transmission electron microscopy

Imaging of the nanoparticles was performed via scanning transmission electron microscopy (STEM) on a Magellan 400 SEM (FEI Company, Hillsboro, United States) in STEM operation mode with the STEM II detector. The images were taken with an acceleration voltage of 28 kV and a current of 0.1 nA in high-angle annular dark field mode. For STEM an ion beam of high-energy electrons is focused on a thin sample and used to scan the sample. The images were taken by the staff of the Helmholtz Nanoelectronic Facility. The nanoparticle samples were prepared as described in subsection 3.3.2 and diluted 1:50 with purified and deionized water. Afterwards, 5  $\mu$ L of the sample solution were dropped onto a copper grid with a formvar mesh as support (SF162-3, Plano GmbH, Wetzlar, Germany) and left under the hood until complete evaporation of the solvent. The particle size distribution was analyzed with ImageJ [153] upon introduction of a threshold to the images.

## 3.4 DNA hybridization

### 3.4.1 SYBR Green fluorescence assay

DNA hybridization in solution and on silver nanoparticles was monitored with a fluorescence hybridization assay using SYBR Green I (SG) as nucleic acid dye. SG preferentially binds to double stranded DNA causing fluorescence enhancement and therefore the transition from single to double stranded DNA in case of hybridization can be evaluated.

Prior to each experiment set, the SG stock solution (100.000x) was diluted 1:10 with purified and deionized water. The total sample volume was set to 200  $\mu$ L with always 5  $\mu$ L SG (1:10). DNA and nanoparticle concentrations were adjusted with PBS-50. For experiments containing only DNA and no nanoparticles, the concentrations ranged from 10 to 2000 nM with details

specified in the respective sections. For hybridization on silver nanoparticles, the DNA concentrations were 10, 100 and 1000 nM with a nanoparticle concentration of  $c_{\text{AgNP}} = 1000 \text{ pM}$ . After mixing and 2 min incubation, the samples were excited with the blue laser ( $\approx 470 \text{ nm}$ ) and the emission fluorescence intensity was recorded. For evaluation of the hybridization process, the emission values in range 1 from 514-567 nm were used due to the emission of SG with dsDNA being centred at 520 nm. Each sample was measured at room temperature, at 65°C (5 min heating time) and again at room temperature after cooling down (5 min). All measurements were performed with the DS-11 FX Spectrophotometer/Fluorometer (DeNovix Inc., Wilmington, United States).

Fluorescence emission spectra were recorded on a QM-7 spectrofluorometer (Photon Technology International, Birmingham, United Kingdom) using quartz cuvettes with a 3 mm path length (Hellma, Mühlheim, Germany). All measurements were performed with a DNA concentration of 2000 nM. The slit widths were adjusted to 0.5 mm for excitation and 0.75 mm for emission. The samples were excited at a wavelength of 485 nm and the spectra recorded from 500 to 700 nm.

#### 3.4.2 Nanoparticle impact electrochemistry

Impact electrochemistry based detection of DNA hybridization was performed following the procedure described in section 3.2. Samples were prepared in a total volume of 50  $\mu\text{l}$  and concentrations adjusted with PBS-50. The DNA concentrations ranged from 10 to 1000 nM with a concentration of 370 pM for the DNA-capped nanoparticles (corresponds to 23 pM when measured in a final chip volume of 800  $\mu\text{l}$ ). After 20 min incubation at room temperature, the nanoparticle impacts were measured at a potential of 0.4 V in PBS-200 as background electrolyte. A measurement set consisted of a blank measurement with only DNA-capped silver nanoparticles, the actual hybridization with complementary DNA and a control with non-complementary DNA.

### 3.5 Buffers, chemicals and reagents

**Table 3.3:** Summary of used buffer solutions with composition and pH values. pH values adjusted with HCl or NaOH, accuracy:  $\pm 0.05$  pH units.

Name	Composition	pH-Value
PBstock	0.5 M $\text{Na}_2\text{HPO}_4$ , 0.5 M $\text{KH}_2\text{PO}_4$	not adjusted
PBS-50	0.01 M phosphate (from PBstock), 0.05 M NaCl	7.4
PBS-100	0.01 M phosphate (from PBstock), 0.1 M NaCl	7.4
PBS-200	0.01 M phosphate (from PBstock), 0.2 M NaCl	7.4

**Table 3.4:** List of used chemicals and suppliers.

Chemical	Company	Purity [%]
Polydimethylsiloxane (PDMS), Sylgard 184	Dow Corning GmbH	-
KCl	Sigma-Aldrich	99.0
$\text{Fc}(\text{MeOH})_2$	Sigma-Aldrich	98.0
$\text{H}_2\text{SO}_4$ , 96 %	Merck KGaA	-
Silver dispersion 10 nm	Sigma-Aldrich	-
$\text{NaNO}_3$	Sigma-Aldrich	99.0
$\text{KH}_2\text{PO}_4$	Carl-Roth GmbH	98.0
$\text{Na}_2\text{HPO}_4$	Sigma-Aldrich	98.5
NaCl	Sigma-Aldrich	99.5
$\text{MgCl}_2 \cdot 6 \text{H}_2\text{O}$	Sigma-Aldrich	98.0
TCEP, $\text{C}_9\text{H}_{15}\text{O}_6\text{P} \cdot \text{HCl}$	Sigma-Aldrich	98.0
SYBR Green I	Lonza Group	-
Acetone	Sigma-Aldrich	>99.5
Isopropanol	Sigma-Aldrich	>99.5



### 3.6 Statistics and python based data evaluation

All nanoparticle modifications for the different DNA strands and concentrations were at least performed three times. Every measurement reported with a value and a corresponding error bar was at least performed three times. The exact number of replicates is given in the respective section. The nanoparticle size distributions are stated as mean value with standard deviation (std). All other values represent the mean and the standard error of the mean (sem). All statistical data evaluation and plotting was performed in *python*. A list of the relevant functions is given in the following table.

**Table 3.5:** Python functions used for data evaluation and plotting.

Parameter	python function
Mean value	numpy.mean
Standard error of the mean (sem)	scipy.stats.sem
Standard deviation	numpy.std
Line or marker plot	matplotlib.pyplot.plot
Errorbar plot	matplotlib.pyplot.errorbar
Histogram + kernel density estimation	seaborn.distplot
Linear fit	numpy.polyfit, scipy.stats.linregress
Power spectral density	scipy.signal.welch
Langmuir fit	scipy.optimize.curve_fit
Integration of area	numpy.trapz

## 4 Particle modification and characterization

DNA functionalized metallic nanoparticles are widely employed for bioanalytical purposes. Key prerequisite for any application is a reliable and reproducible preparation method resulting in stable DNA-nanoparticle conjugates. Most research in this field has focused on gold nanoparticles due to a relatively easy modification procedure and good particle stability [154,155]. However, for applications based on electrochemical detection silver nanoparticles represent a more suitable choice because of their superior electrochemical activity in comparison to gold nanoparticles [156]. DNA-silver nanoparticle conjugates have been reported to have nearly identical properties and it is generally assumed that the theories and models developed for gold nanoparticles can be applied to silver nanoparticles [157]. However, the well-established 'salt-aging' preparation method reported for gold modifications cannot be easily transferred to silver nanoparticles and a modification of silver with DNA is challenging [154, 155, 158–160]. This accentuates the need for a reliable and reproducible preparation method for synthesizing stable DNA-AgNP conjugates. Ideally, the method is applicable to different DNA strands and concentrations in order to give access to varying DNA ligands. Besides preparation a careful characterization of the physical and chemical properties is essential for any subsequent application. Important aspects are surface charge, size distribution or the ligand surface density. Especially, the DNA surface coverage is crucial for bioanalytical applications with the DNA as probe element since it strongly influences target binding. The most common approaches for determination of DNA densities are invasive and the nanoparticles cannot be reused [107, 159, 161]. This usually requires preparation of duplicates or larger amounts of samples. Non-invasive methods could decrease operating expenses and material consumption. In the following sections, the silver nanoparticle modification and subsequent characterization will be described in detail. In particular, the determination of the ligand surface density with non-invasive techniques will be discussed and compared to literature reports.

## 4.1 Physical and chemical properties

In this work, citrate stabilized silver nanoparticles with a diameter of 10 nm were modified with thiolated single stranded DNA, following a modified 'salt-aging' protocol. The number of nucleotides per ssDNA molecule ranged from 10 to 26 and the ratio of nanoparticles to DNA during modification (NP:DNA ratio) was varied from 1:10 to 1:1000 as given in Table 4.1. A nanoparticle diameter of 10 nm was chosen in order to obtain adequate electrochemical signals (the lower detection limit for impact electrochemistry is  $\geq 9$  nm), while keeping the amount of receptor molecules low to ensure efficient target binding. Modification of larger nanoparticles with DNA via the salt-aging method is more challenging and low ligand densities are difficult to achieve [162].

The conjugation of thiolated DNA to nanoparticles has been firstly reported in 1996 [96,97] and is based on the strong affinity of thiol groups to the surfaces of noble metals such as gold or silver [71,163]. In contrast to adsorption of short thiol molecules such as alkanethiols, the process is more complex for DNA attachment due to a negative surface charge on both, nanoparticles and DNA. To overcome this issue, Mirkin and co-workers developed a procedure called 'salt-aging' [164], which is depicted in Figure 4.1. The addition of salt to the reaction solution leads to a screening of negative charges at the DNA surface according to Debye-Hückel theory, which predicts a decrease of the Debye length with increasing ionic strength [165]. On the one hand, the addition of salt reduces the repulsive forces between nanoparticles and DNA as well as between individual DNA strands. As a result, DNA adsorption onto the nanoparticle surface is enhanced and high DNA loadings can be obtained. On the other hand, salt also impairs the electrostatic repulsion between nanoparticles, which decreases the colloidal stability and causes aggregation. Therefore, a successful DNA-nanoparticle conjugation requires careful balancing of charge screening by adding salt while maintaining colloidal stability [108,149,162,166]. The term aggregation here is used to describe irreversible clustering of nanoparticles, whereas agglomeration refers to a reversible sticking process [167]. Typically, a mixture of DNA and nanoparticles is incubated overnight followed by a stepwise increase in salt concentration to a final concentration of 1 M NaCl. However, this procedure has been reported to result in aggregation of silver nanoparticles [154,155,158–160].

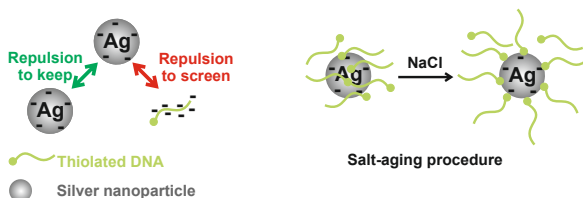


**Figure 4.1:** Scheme of the nanoparticle modification with thiolated single stranded DNA via the salt-aging procedure to screen the repulsive negative charges.

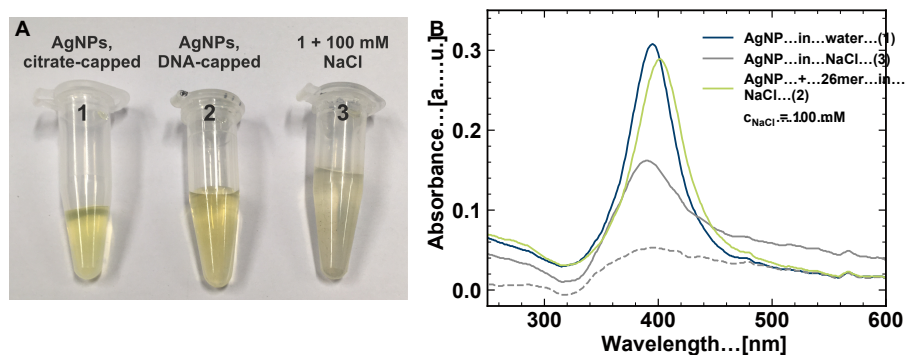


**Figure 4.2:** A) 1. Citrate-capped AgNP solution; 2. DNA-capped AgNP solution; 3. Citrate-capped AgNP solution in 100 mM NaCl. B) UV-Vis spectra of citrate-capped AgNPs in water (blue), 100 mM NaCl (grey) and spectra of DNA-capped AgNPs in 100 mM NaCl (green). Solid line:  $t = 0$  min, dashed line:  $t = 10$  min.

In order to address this issue, a more gentle approach was used. The stepwise salt addition was distributed over 5 days with an incubation time of 24 h between each step. This provided a sufficient level of stabilization by the DNA molecules before further increasing the salt concentration. The first increment was kept below the critical coagulation concentration ( $\approx 48$  mM [150]) to prevent immediate nanoparticle aggregation. The modified procedure as described in subsection 3.3.2 results in stable DNA-AgNP conjugates for all tested DNA length and over a wide range of initial DNA concentrations. The as prepared samples were characterized by UV-Vis spectroscopy. Figure 4.2 shows an image and the corresponding UV-Vis spectra of citrate and DNA-capped AgNPs in different electrolytes. The blue spectrum gives the absorbance for citrate-capped AgNPs with a distinct absorption band at 393 nm, corresponding to a bright yellow colour of the solution. This is a result of the strong surface plasmon resonance of silver nanoparticles. Upon DNA modification and the addition of 100 mM NaCl, the resonance peak undergoes a red shift of  $\approx 9$  nm, which is caused by the surface modifications [157], or a change in the surrounding medium due to the presence of electrolyte [155, 164, 168]. The spectrum for citrate-capped AgNPs in 100 mM NaCl exhibits lower absorption intensities and a broader peak, which disappears nearly completely within 10 minutes. The reason for these observations is salt-induced nanoparticle aggregation as described earlier in this section. This can also be confirmed by a colour change of the solution from bright yellow to nearly transparent. The aggregation behaviour in PBS with 100 mM NaCl is identical (see Appendix Figure 8.3) being in accordance to literature findings, where charge screening by NaCl was identified to be the main reason for aggregation [169].

The fact that the DNA-capped AgNPs are stable in PBS whereas the citrate-capped AgNPs aggregate indicates that the DNA is attached to the nanoparticle. The DNA molecules are bulkier and carry more negative charges, which increases steric and electrostatic repul-

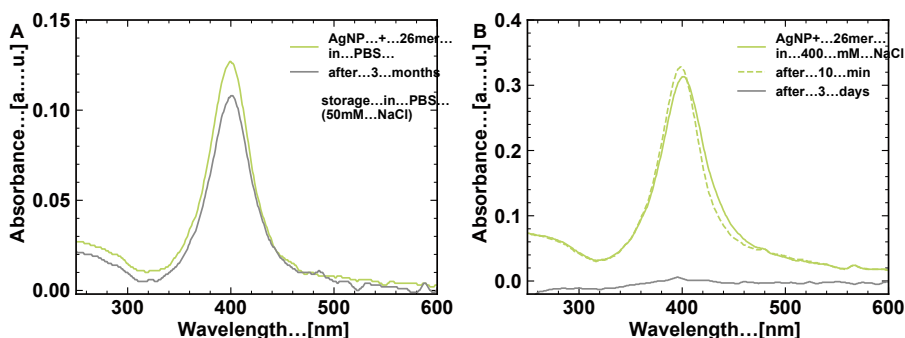


**Figure 4.3:** A) UV-Vis spectra of DNA-capped nanoparticles after centrifugation (green) and 3 months storage in PBS (50 mM NaCl) (grey). B) UV-Vis spectra of DNA-capped nanoparticles in 400 mM NaCl after mixing (green), 10 min (green, dashed) and 3 days (grey).

sion [156]. This could be additionally verified by inductively coupled plasma mass spectrometry. In all samples of DNA-AgNP conjugates, phosphorus could be detected whereas only amounts close to the detection limit were found in the nanoparticle stock solution (see Appendix Table 8.1). Quantification of the ligand density as reported in the literature was not possible due to variations in the amount of detected silver [161].

Additionally, the long-term stability and resistance to elevated salt levels were investigated. In Figure 4.3A, the UV-Vis spectra for DNA-capped nanoparticles (26mer, 1:50) directly after preparation and after three months storage in PBS are depicted. The spectrum measured after three months shows only a slight decrease in absorbance, demonstrating good long-term stability. The reason for the decrease in intensity could be dissociation of DNA from the nanoparticle due to a cleavage of the thiol bond, which reduces the electrostatic repulsion and thus the colloidal stability [170]. On average the samples lost  $16 \pm 2\%$  in absorption intensity within three to six months, which did not interfere with any measurements since most experiments of this work were conducted within four weeks after nanoparticle preparation. Figure 4.3B gives the spectra for DNA-capped nanoparticles (26mer, 1:50) in presence of 400 mM NaCl, showing no changes of the optical properties within 10 minutes. This corresponds to the time frame of a typical impact experiment. However, after three days storage in this electrolyte the AgNPs aggregated completely, indicating that the DNA loading at lower incubation concentrations is not sufficient to protect the AgNPs against high salt concentrations.

Table 4.1 gives the success rate for stable nanoparticle modifications in relation to all performed modifications. The data show nearly no stable modifications at the lowest DNA concentration, good stabilities for the middle ranges and a decrease in modification success for the highest ratio. The low success rates for a ratio of 1:10 indicate that the DNA loading for low modification concentrations is not sufficient to protect the nanoparticles from

**Table 4.1:** Molar ratio (NP:DNA) and success rate for stable nanoparticle modifications in percentage with single stranded DNA of different length.

Ratio	1:10	1:50	1:100	1:200	1:300	1:400	1:500	1:1000
c <sub>DNA</sub> [ $\mu$ M]	0.06	0.3	0.6	1.2	1.8	2.4	3	6
DNA strand	Success rate [%] <sup>1</sup>							
10mer	0	67	100	100	100	100	67	33
13mer	0	100	100	100	100	100	100	100
17mer	33	57	83	86	100	100	100	50
20mer	33	100	100	100	100	100	100	33
26mer	33	100	100	100	100	100	80	83

<sup>1</sup> Percentage of stable modifications out of the total amount of performed modifications. For a stable modification, the absorbance of the 1:20 diluted samples had to exceed a value of 0.05 in the range of 390-410 nm.

aggregation during salt addition [162]. Upon increasing the DNA concentration, stable DNA-nanoparticle conjugates form, due to higher DNA loadings. The diminishing success rate for the highest DNA concentrations can be explained by the addition of a larger volume of TCEP, which can cause particle aggregation as demonstrated by UV-Vis spectroscopy (see Appendix Figure 8.4) [171]. The larger amount of TCEP is a result of the 1:1 DNA:TCEP incubation for cleaving the disulfide moieties prior to particle modification.

The size and morphology of the AgNPs was investigated with scanning transmission electron microscopy (STEM). A STEM image of DNA-capped AgNPs and the density plots for the size distribution of citrate and DNA-capped AgNPs are depicted in Figure 4.4. Most AgNPs exhibited a spherical shape with a size distribution of  $10\pm 3$  nm for citrate-capped and  $10\pm 4$  nm for DNA-capped AgNPs. This conforms with the details provided by the supplier ( $10\pm 4$  nm, see subsection 3.3.2) and reveals that the DNA-conjugation protocol does not alter the size and shape of the nanoparticles. Evaluation of the hydrodynamic radius via dynamic light scattering did not provide consistent data due to a polydispersity of the samples (see Appendix Figure 8.5). Previously, it has been demonstrated that the light scattering from a small percentage of larger particles could almost completely conceal the scattering signal from smaller particles [172]. Zeta potential measurements were performed to estimate the nanoparticle charge (see Appendix Figure 8.6). Citrate-capped AgNPs in water had a zeta potential of  $-31\pm 3$  mV, which is in accordance to the values reported in literature [173] and by the supplier ( $-36$  mV). Upon addition of 10 mM NaCl as background electrolyte, the value shifted to  $-19\pm 2$  mV. For DNA-capped AgNPs in 10 mM NaCl, the average zeta potential was  $-37\pm 1$  mV (17mer and 26mer, ratios 1:50 and 1:100). As rule of thumb colloidal suspensions with a zeta potential higher than  $+30$  mV or lower than  $-30$  mV are considered as stable [174, 175]. Taking this into account, the AgNP stock solution is stable in absence of background electrolyte but destabilized upon the addition of salt. On the contrary, the DNA-

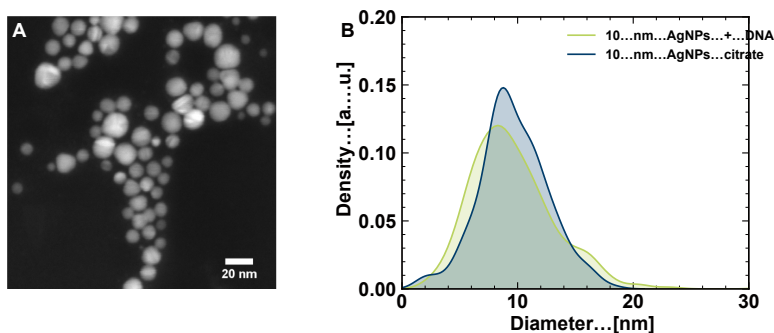


**Figure 4.4:** A) STEM image of DNA-capped nanoparticles. B) Density estimation plot of nanoparticle diameters derived from STEM images for citrate (blue) and DNA-capped (green) 10 nm silver nanoparticles (17mer and 26mer).

**Table 4.2:** Summary of physical and chemical nanoparticle properties. The values for DNA-capped particles are averaged from results for 17mer and 26mer.

capping agent	$\lambda_{max}$ [nm]	diameter [nm]	$\zeta$ -potential [mV]
citrate	$393.2 \pm 0.2$	$10 \pm 3$	$-19 \pm 2$
ssDNA	$402.2 \pm 0.2$	$10 \pm 4$	$-37 \pm 1$

capped AgNP solution is stable in the presence of background electrolyte, which conforms with the UV-Vis results. Table 4.2 gives a summary of the characteristic nanoparticle properties described in this section.

Overall, a modified salt-aging procedure could be successfully adapted to attach thiolated single stranded DNA to silver nanoparticles. The modified protocol is based on a slow step-wise increase of the NaCl concentration in combination with longer incubation periods. This ensures a sufficient particle stabilization by the DNA molecules before further increasing the salt content. Evidence for the presence of DNA on the nanoparticle surface was provided indirectly via UV-Vis spectroscopy and zeta-potential measurements and directly by mass spectrometry.

## 4.2 Density of DNA strands on nanoparticles

An important characteristic of DNA-nanoparticle conjugates is the surface coverage of DNA on the nanoparticle surface. It influences properties such as stability or the accessibility for target binding, which play a crucial role for nucleic acid based detection strategies. The surface coverage is always related to the total amount of available binding sites, which is determined by the space requirement of the anchoring group and the lattice constant of the

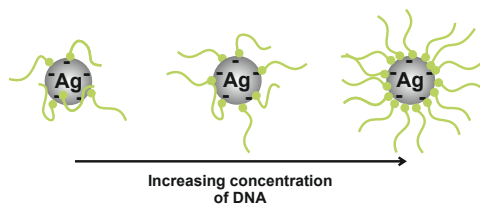


**Figure 4.5:** Nanoparticle modification with different DNA concentrations. An increasing DNA concentration results in higher DNA densities on the nanoparticle surface and upright orientation of the strands.

metal. Experimentally, the DNA loading capacity is governed by solution conditions such as DNA and salt concentration but also the length of the oligonucleotide [107, 166, 176]. In general, self assembly of thiolated molecules onto metallic surfaces is considered to follow a Langmuir adsorption model with monolayer adsorption and establishing of an adsorption/desorption equilibrium [71, 177–179]. Such a behaviour has also been reported for thiolated and non-thiolated single stranded and double stranded DNA. Accordingly, the surface coverage increases with increasing DNA concentration until eventually reaching saturation [166, 180–183]. The attachment of DNA to the nanoparticle surface is dominated by the thiol-Ag bond formation, providing the possibility for single-point attachment. However, requirement for the attachment is a close approach in space of DNA molecules and the nanoparticle, which is facilitated at higher salt concentrations due to the charge screening effect. Already adsorbed strands impose steric and electrostatic hindrance to arriving strands. As a consequence, at a given salt concentration only a certain DNA loading can be reached. An increase in the salt concentration induces additional charge screening and more strands can be attached. Thus, the maximum density is not governed by the reactivity of the attachment group but by steric and electrostatic effects between individual DNA strands [162, 166, 176]. The conformation of the strands changes from lying flat on the surface due to non-specific interactions to upright with increasing initial DNA concentration as depicted in Figure 4.5 [162, 184–186].

Different methods can be utilized for determining the DNA coverage, such as using DNA molecules labelled with a fluorophore [107], gel electrophoresis [183] or determination of the amount of unbound DNA in the supernatant [151]. The latter was employed to determine the DNA surface coverage of the prepared DNA-AgNP conjugates reported in the previous section. Two different spectroscopic strategies were used and compared. The first one is based on a fluorescence assay with SYBR Green I (SG) as nucleic acid dye. Preferentially, SG binds to double stranded DNA, resulting in a fluorescence enhancement. However, it was also reported to bind to single stranded DNA [152] and this was used to establish a calibration curve for determining the concentration of DNA (see Appendix Figure 8.8). The second approach is based on measuring the UV-Vis absorption at 260 nm, which is typically used to calculate DNA concentrations. Again a calibration curve was used to determine the concen-



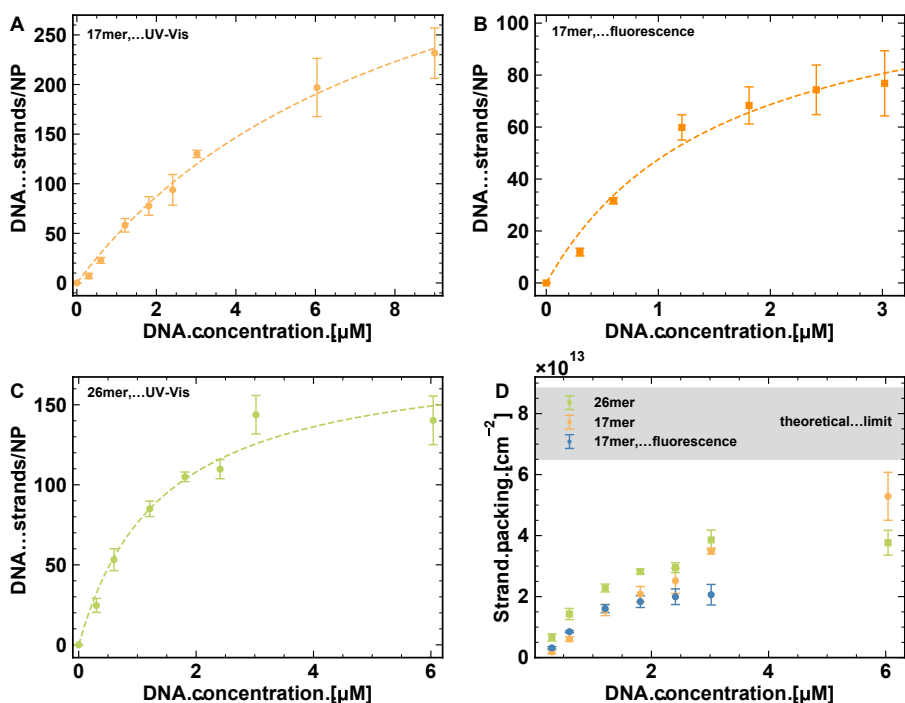


**Figure 4.6:** Adsorption isotherm for ssDNA strand adsorption onto AgNPs, dashed line shows the fit derived from Equation 4.1. A) 17mer (derived from UV-Vis data), B) 17mer (derived from fluorescence data), and C) 26mer (derived from UV-Vis data). D) DNA strand packing per nanoparticle surface area for 17mer (orange), 17mer, fluorescence (blue), and 26mer (green) DNA. The grey area gives the theoretical limit calculated with the estimated cross-sectional radius of a ssDNA strand [184].

tration of unbound DNA (see Appendix Figure 8.9). A control of all supernatants collected during nanoparticle preparation proved the presence of unbound DNA only in the first one (see Appendix Figure 8.7). The concentration of adsorbed DNA was obtained by subtraction of the measured DNA concentration in the supernatant from the initial DNA concentration added for modification. The concentration was converted into the number of DNA strands. With the number of AgNPs in the solution, the number of DNA strands per nanoparticle could be derived.

The DNA coverages, expressed as DNA strands/NP, plotted against the initial DNA concentration for 17mer (A+B) and 26mer (C) are given in Figure 4.6. For all experiments, the final salt concentration was 0.13 M. For the lowest DNA concentration (0.06  $\mu\text{M}$ ) measurements were not possible, due to the initial concentration being below the absorbance limit of the spectrometer. Expectedly, for both oligonucleotides the number of strands/NP increases with initial DNA concentration independent of the measurement procedure. As already mentioned, the adsorption of thiolated molecules can be described by the Langmuir model, which

is frequently used to fit experimental data [178, 179, 182, 187]. The model assumes a fixed number of equivalent adsorption sites and an approximately constant concentration of thiolated ligands. Additionally, an adsorption/desorption equilibrium has to be formed and the adsorbed molecules do not interact with each other [38, 181, 182]. However, DNA molecules carry a negative net charge, which induces electrostatic repulsion between individual DNA molecules. Therefore, adsorption of one molecule can influence the adsorption at a neighbouring site. Molecule adsorption in this case can be described by the Frumkin isotherm, accounting for intermolecular interactions [38, 188]. For an adequate description of the employed salt-aging modification, two different aspects have to be considered: the electrostatic interaction between DNA and the charge screening by the added salt. The Debye length for the used concentration of 130 mM NaCl is below 1 nm [189]. Accordingly, it can be assumed that the charges are effectively screened, which diminishes the electrostatic interactions. With this assumption, the Langmuir model was used to analyze the data. Establishment of an adsorption/desorption equilibrium can be assumed for the used modification protocol due to the overall incubation time of five days and the 24 h waiting period in between two salt increments.

The dashed line in Figure 4.6 corresponds to a fit of the data to the Langmuir isotherm (Equation 4.1). A summary of the adsorption parameters can be found in Table 4.3. The fitting is adequate as can be judged from the values of adjusted R squared. Considering the relative large error bars for the determined coverages, it can be expected that the experimental error is larger than the error stemming from the simplification of the model. For the UV-Vis based data for the 17mer, no saturation can be observed in the investigated concentration range. Accordingly, Langmuir fitting gives a high value for the maximum loading, which exceeds the geometrically possible loading of 200-300 strands given in Table 4.3. This limit was calculated with the estimated cross-sectional radius of a ssDNA strand and the surface area of a 10 nm AgNP [184]. Reasons for this could be irregularities during preparation or adsorption above the monolayer level due to interstrand interactions. The fluorescence results and the ones for 26mer both reach surface saturation for an initial DNA concentration of 2-3  $\mu$ M. Overall, the observed values for maximum loading range between 80-160 strands and are in accordance with the fitted values and literature results, where  $\approx$  220 strands have been reported for 20 nm silver nanoparticles [159]. However, a comparison with literature values is difficult since the adsorption highly depends on the solution parameters and a variety of different loadings have been reported for different adsorption parameters and nanoparticle sizes.

A comparison of the different methods and possible limitations are discussed in the following. The strand packing per nanoparticle surface area is plotted in Figure 4.6D, together with the theoretical limit derived from geometrical considerations (grey area). This limit was calculated using the estimated cross-sectional radius of a ssDNA strand (0.6 to 0.7 nm) and ranges between  $6\text{-}9 \times 10^{13}$  strands/cm<sup>2</sup> [184]. It corresponds to a closely-packed conformation but likely overestimates the maximum coverage, since it neglects steric effects of hydration and

$$y = \left( \frac{y_{max} K_a C_{DNA}}{1 + K_a C_{DNA}} \right), \text{ with } 0 < y < y_{max} \quad (4.1)$$

**Table 4.3:** Parameters for DNA adsorption onto AgNPs obtained by fitting Equation 4.1 to the DNA adsorption isotherms.

	$y_{max}$ [strands/NP]	$K_a$ [ $\mu\text{M}^{-1}$ ]	Adj. $R^2$
17mer, UV-Vis	464±45	0.12±0.02	0.99
17mer, fluorescence	124±18	0.62±0.20	0.97
26mer, UV-Vis	185±17	0.71±0.17	0.97
theoretical geometrical loading	240 - 330		

counterions. The coverage values for 17mer show good accordance until 2-3  $\mu\text{M}$  when comparing data from UV-Vis and fluorescence experiments. For the higher DNA concentrations, evaluation based on the fluorescence assay is not possible because the fluorescence calibration curve only shows linear behaviour until 3.5  $\mu\text{M}$ . If we compare the adsorption isotherms for 17mer and 26mer, the values for 26mer are a bit higher but overall the coverages for both strands are in reasonable accordance until 2.4  $\mu\text{M}$ . The larger values for 26mer are most likely an artefact of the measurement procedure and not caused by the different length of the strands. With more nucleotides the absorption at 260 nm increases, as can be seen from the respective calibration curves (see Appendix Figure 8.9). This results in a better detectability for the longer strand, especially in the lower concentration regime. For all three data sets, the strand packing increases with initial DNA concentration up to values of around 1.5  $\mu\text{M}$ . With increasing concentration ( $\approx 2 \mu\text{M}$ ) surface saturation starts. For strand packings above  $2 \times 10^{13}$  strands/ $\text{cm}^2$ , it can be expected that the probes are densely packed and solely attached via the thiol group [184]. Such packings have been obtained for DNA concentrations around 2  $\mu\text{M}$ , which fits well with the observed starting point for saturation.

Overall, the results for the different strands and methods are in reasonable agreement considering the reported limitations. They follow the expected trend of increasing DNA surface loading with increasing initial DNA concentrations until surface saturation is reached. Increasing densities could be observed until  $\approx 1.5 \mu\text{M}$  and surface saturation starts for higher concentrations. In the concentration regime below 1  $\mu\text{M}$  the strand packing is relatively low, which can explain the observed low stability of the AgNP-conjugates in this range. The adsorption isotherms also allow for inference of the DNA strand conformation on the surface. For low packings, a parallel orientation to the nanoparticle surface due to non-specific interactions is supposable. In the saturation regime it can be assumed that the strands are densely packed and only attached via the thiol group resulting in an upright conformation.

## 4.3 Summary

In summary, the findings reported in this chapter validate a stable and reliable conjugation of thiolated DNA to silver nanoparticles with a modified salt-aging procedure. Preparation could be demonstrated for different DNA strands and a variety of different concentrations. The resulting DNA-AgNP conjugates exhibit long-term stability for several months and resistance to elevated salt concentrations, which is crucial for samples intended for measurements in biological media. Furthermore, the conjugation protocol does not alter the size distribution, which is important for stochastic nanoparticle impact electrochemistry in order to discriminate between individual AgNPs and aggregates or between different nanoparticle sizes.

It was possible to determine the DNA density on the nanoparticles with two different spectroscopic methods based on analyzing the amount of unbound DNA in the supernatant. A benefit of this non-invasive approach is, that no costly fluorescence tag on the DNA strand is required. No separate nanoparticle modification exclusively for determination of the DNA loading is necessary, which reduces material consumption and preparation time. The obtained values for both methods are in good agreement with literature results and double checking with two different methods generally increases accuracy. Thus, the reported methods represent a straight-forward and efficient procedure for determining the DNA loading on nanomaterials. The preparation method follows the expected trend of increasing DNA surface loading with increasing initial DNA concentrations until surface saturation is reached. With this finding it is possible to correlate the DNA concentration during preparation with characteristic properties of the later formed DNA-AgNP conjugate. This is important for tailoring the nanoparticle properties as required for specific applications. For example the increase in strand packing matches with the observed trend in enhanced conjugate stability with higher DNA concentrations. Additionally, it allows for predictions of the DNA conformation, which is relevant for target binding assays.



## 5 Stochastic nanoparticle impact electrochemistry

Stochastic nanoparticle impact electrochemistry represents a versatile analytical tool for the detection and characterization of nanoparticles as well as for monitoring of biomolecular binding and recognition processes. A crucial step for any analytical application is a careful and detailed characterization of the system and its individual components.

The measurements performed in this work are based on the stochastic amperometric detection of AgNPs as previously reported by our group [27]. The main part of the experimental setup consists of a combination of low noise microelectrode arrays with a highly sensitive current amplifier system. The expected current is in the range of picoamperes. Such low currents can be easily exceeded by the background noise of the electrochemical measurement system. Thus, a careful evaluation of the noise behaviour is required in order to determine the current range for reliable detection and possible limitations. In addition to the background noise, also other parameters such as the nanoparticle concentration, applied potential or electrolyte composition are important and have to be adjusted carefully. For citrate-capped silver nanoparticles, several studies have worked on the identification of critical parameters and the system is relatively well-understood [27, 29–32]. The modification with ligands others than citrate can have a strong influence on the oxidation behaviour, as it has been demonstrated for DNA [22]. However, most research related to DNA modifications focused on electrocatalytic impacts with platinum nanoparticles [21, 190, 191]. Thus, several questions with regard to direct Faradaic impacts remain:

- How does the DNA effect Faradaic impacts and does this eventually require an adjustment of measurement parameters?
- What is the influence of DNA length and DNA density on the nanoparticles?

This chapter gives a characterization of the experimental setup and the AgNP based detection scheme. Additionally, a detailed evaluation of the influence of DNA functionalization on the AgNP impact behaviour and the effect of the measurement parameters, such as applied potential or background electrolyte is presented. This investigations are complemented with a comprehensive study on the influence of different DNA length and densities.

## 5.1 Characterization of the BioMAS measurement device and experimental procedure

### 5.1.1 Noise analysis

Microelectrode arrays (MEAs) are widely used for the detection of small extracellular voltages in electrophysiology measurements [192, 193]. However, their potential for the amperometric detection of neurotransmitter release has also been demonstrated [194, 195]. In our group, this amperometric sensing concept was employed for the detection of individual silver nanoparticle impacts. One of the main limitations for low current measurement systems is the background noise. It is commonly measured as root mean squares of the current and determines the smallest detectable signal [196]. In case of nanoparticles it imposes a lower size limit [27]. Therefore, a careful analysis of the system's noise behaviour is crucial in order to perform reliable measurements. The sensing element of the in-house built amplifier used in this work is a transimpedance amplifier consisting of a low-noise operational amplifier in combination with a feedback resistor. The noise performance of this element is decisive for the overall noise behaviour, since it is the main building block of the circuit. The possible noise sources are the feedback resistor, the transistors in the operational amplifier (op amp) and the input impedance. In the equivalent circuit, a complex impedance model is always present between the input current and the measurement system, which corresponds to the impedance of the solution and the electrode [197]. Thus, the properties of the working electrode such as material, size and shape also have an effect on the current noise [198]. Prior to any noise measurements, the MEA electrodes were characterized with cyclic voltammetry to verify their electrochemical activity and to get an estimate of the electrochemical surface area (ESA). Exemplary cyclic voltammograms are given in Appendix Figure 8.10. Only MEA chips showing electrochemical activity and overall reliable performance were used for further analysis. A detailed noise analysis was performed for nine MEA chips from two different fabrication batches. In total five measurements for different potentials and electrolytes were used to evaluate the noise performance of a single chip. Additionally, the noise originating from the amplifier system was investigated. Table 5.1 summarizes the obtained values. The setup without any connected cell has a root mean square (rms) current noise of 0.48 pA and

**Table 5.1:** Average root mean square (rms) and peak to peak (pk2pk) noise for picoAmp headstage and MEA chips (potential = 0.4 V vs. Ag/AgCl, gain = 10).

	rms [pA]	pk2pk [pA]
Headstage	0.48±0.00	4.00±0.03
MEA chip	2.01±0.11	18.17±0.74

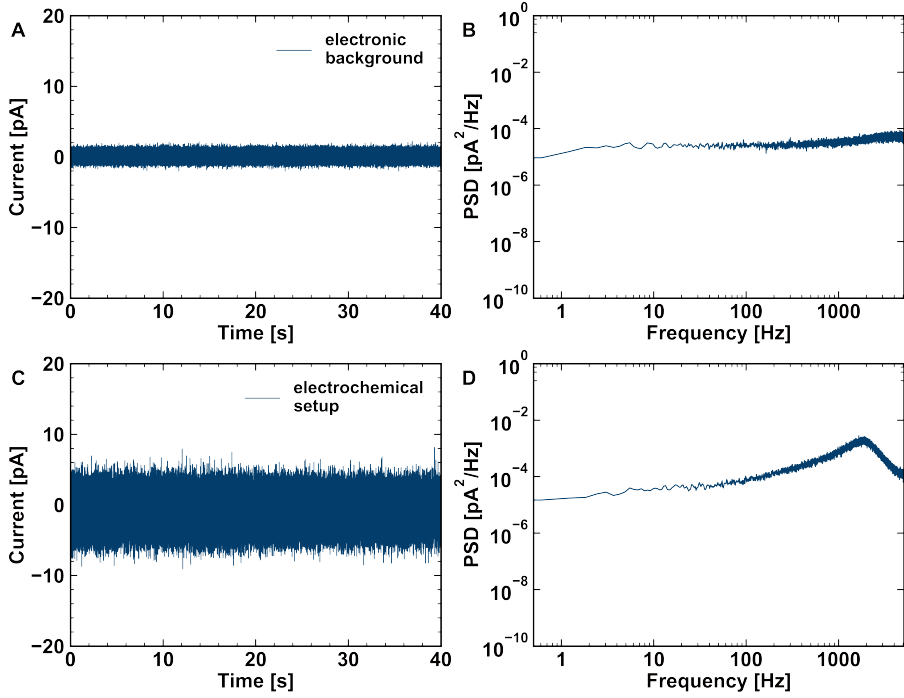


**Figure 5.1:** A) Current-time trace and B) power spectral density of an individual channel for only the BioMAS setup and C) current-time trace and D) power spectral density for the whole measurement setup consisting of BioMAS, MEA electrode, electrolyte and reference electrode. Potential = 0.4 V vs. Ag/AgCl. Measurement parameters as described in Table 3.1.

a peak to peak (pk2pk) noise of 4 pA. Upon connection of an electrochemical cell, the noise increases to a rms of 2 pA and a pk2pk of 18 pA. The overall current rms noise for the system is thus assumed to be  $\approx 2$  pA. The chips showed a stable noise behaviour up to one year of experimental usage. Prior to each measurement set, the noise behaviour and overall chip performance was checked. In case of any irregular peak behaviour, the chip was sorted out and not used for any experiments in order to ensure reliable measurements.

An exemplary current time trace and the calculated power spectral density (PSD) for the amplifier system (A+B) and the electrochemical setup (C+D) consisting of amplifier, MEA, electrolyte and reference electrode are given in Figure 5.1. Having a look at the current traces illustrates the increase in current noise upon connecting an electrochemical cell. An important information that can be derived from the PSD is the absence of a peak at 50 Hz. This indicates that the shielding and the low noise power supply work efficiently and no line interference (pick up of capacitive AC signals from lights and other equipment) disturbs the measurements [194]. The PSD for the amplifier is nearly constant over the frequency spectrum and only shows a slight increase for higher frequencies. From this it can be con-



cluded that especially at lower frequencies the thermal noise of the feedback resistor, being approximately white in nature, is the main noise source [197]. Once the electrochemical cell is connected, the amplitude increases slowly until around 100 Hz. This is followed by a clear increase until 2 kHz, where the noise peaks and decreases for higher frequencies. The increase at higher frequencies can be attributed to the input parasitic and cell capacitances. This high frequency noise dominates the overall current noise, which explains the clear change in rms from 0.48 to 2 pA for connecting an electrochemical cell. With the high frequency noise as dominant component, it is necessary to carefully balance the bandwidth and the current noise. If possible, more bandwidth is always desirable, which in turn increases the current noise [197]. The temporal resolution of a signal is determined by the bandwidth, which has to be sufficient to ensure accurate data acquisition. For the BioMAS system, the bandwidth depends on the analogue-digital-converter (ADC), featuring a maximum sampling frequency of 1.25 MHz. A sampling rate of 10 kHz per electrode provides sufficient resolution for detection of the nanoparticle impacts. If a higher resolution is required, for example to identify different spike shapes, it is possible to increase the sampling rate to 100 kHz. However, this strongly decreases the number of recording channels (6 instead of 64). Therefore, the benefit of simultaneous recordings from a large number of channels is lost. A way to decrease the background noise could be a reduction of the electrode size, since the current noise scales with the electrode size [194, 198]. This could decrease the current noise but especially for detection of low nanoparticle concentrations a larger electrode area is beneficial to increase the number of impacts [140]. Consequently, the electrode size has to be adjusted according to the specific measurement intention.

Overall, the investigated MEA chips show a reproducible noise behaviour and the current rms is sufficiently low in order to ensure reliable detection of 10 nm AgNPs, as will be discussed in detail in section 5.2. The measurement system is shielded effectively and exhibits a certain insensitivity towards external influences such as vibrations. The 10 kHz sampling rate used for the measurements represents a good compromise, allowing for sufficient resolution of the impacts while keeping the noise level relatively low.

### 5.1.2 Experimental procedure

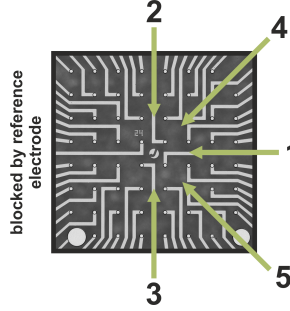


**Figure 5.2:** Insertion scheme for AgNP impact experiments with the MEA centre and different positions for the AgNP insertion (1-5). The left side of the MEA chip is always blocked by the reference electrode.

According to the measurement procedure described in subsection 3.2.3, the AgNPs are inserted manually for every impact experiment and slight deviations in insertion speed, angle or position are inevitable. In order to assess the influence of such deviations on the measurements and the obtained results, a set of control experiments was performed. A careful evaluation of the measurement procedure is crucial to exclude systematic influences, that might bias the results. Figure 5.2 shows the centre of a MEA chip with five different positions for AgNP insertion during the experiment with position 1 as standard position. In total, six measurements per individual position were performed and the current traces analyzed as described in subsection 3.2.4. Additionally, the insertion speed was reduced for insertion at position 1. Table 5.2 gives the total number of impacts, the impact frequency per chip and electrode [Hz] and the number of active, inactive and noisy channels out of 63 along with the standard error of the mean and the average over all positions. As expected, the number of impacts and accordingly the frequency fluctuates within the measurements for one position as well as between different positions with an error ranging from 6 to 18%. Such a level of variation has been reported previously and is believed to be an intrinsic feature of impact measurements, especially for relatively short time scales [21]. Upon averaging over all positions, the measurements show an error of 6% without any influence or trend induced by the different insertion positions. Interestingly, the number of active and inactive channels is relatively constant and shows no dependence on insertion position. On average 54 electrodes showed nanoparticle impacts, three were inactive and six showed noisy behaviour. This yields in 86% of working electrodes, which is sufficient for measuring a significant number of impacts simultaneously. The reasons for inactive channels could be inoperable electrical contacts, fabrication residues, the formation of bubbles during addition of the electrolyte or the absence of colliding particles at this electrode. All together the results demonstrate a reliable measurement reproducibility and insusceptibility to deviations in the nanoparticle insertion process.

**Table 5.2:** Averaged values for the total number of impacts, impact frequency in Hz per chip and electrode, number of active, inactive and noisy channels (of 63) for different measurement positions (1-5). Potential = 0.4 V vs. Ag/AgCl. Measurement parameters as described in Table 3.1.

Position	Total number of impacts	Impact frequency (chip) [Hz]	Impact frequency (electrode) [Hz]	Active channels (of 63)	Inactive channels (of 63)	Noisy channels (of 63)
1	5715±1039	143±26	2.3±0.5	52±2	5±2	6±0
1, slow	7599±438	190±11	2.8±0.1	54±2	2±1	7±1
2	7393±676	185±17	2.5±0.5	57±1	0	6±1
3	4596±555	115±14	1.5±0.2	55±2	3±2	5±1
4	4707±440	118±11	1.5±0.2	50±4	7±4	6±1
5	3330±350	83±9	1.1±0.2	55±2	3±2	6±1
Average	5562±355	139±9	2.0±0.2	54±1	3±1	6±0

With the error decreasing for an increasing number of measurements  $n$  the measurements follow the rules of basic statistics [199]. The replicable behaviour of one chip is important in order to be able to identify changes and trends originating from the nanoparticles and their modifications. However, the chip to chip variance, especially for different fabrication batches, is rather large and the total number of impacts and thus also the impact frequency can vary strongly for measurements on different chips. In Table 5.3, a summary of the obtained values for 3 measurements per chip on three individual chips from different batches are given. The results show a good reproducibility within the measurements on one chip. Comparing the values for different chips shows a large variation in the total number of impacts. The variation is independent of the number of active channels and a chip with more available channels does not necessarily show higher impact frequencies. Due to this large variance, averaging over different chips results in large errors. The most likely reason for this behaviour are variations in the fabrication process of the chips. The deposited gold films can consist of gold grains with differing sizes, resulting in different surface roughness. Overall, the changes are expected to be in the nanoscale range. This could have influence on the nanoparticle impact experiments, which happen at the nanoscale and depend on the composition of the nano-interface. To exclude measurement artefacts originating from variations in the chip fabrication process, all experiments were reproduced on different chips from different batches.

All together, the results confirm a stable and reproducible measurement procedure and no susceptibility to the nanoparticle insertion process. Within a measurement set on one chip the results show some variation, which can be attributed to the nature of the collision experiments. In addition to that, the measurements feature a variance from chip to chip. In combination, these effects can result in rather large errors. In order to address this,

**Table 5.3:** Averaged values for the total number of impacts, impact frequency in Hz per chip and electrode, number of active, inactive and noisy channels for different MEA chips. Potential = 0.4 V vs. Ag/AgCl. Measurement parameters as described in Table 3.1.

Chip	Total number of impacts	Impact frequency (chip) [Hz]	Impact frequency (electrode) [Hz]	Active channels	Inactive channels	Noisy channels
1 <sup>1</sup>	3688±84	92±2	1.9±0.1	49±1	1±1	3±0
2	2162±79	54±2	0.5±0.1	58±2	2±1	3±1
3	5861±155	147±4	2.3±0.1	60±0	0	4±0
Average	3904±461	98±12	1.6±0.2	56±2	1±1	3±0

<sup>1</sup> from the beginning only 53 channels available due to fabrication process.

discussion and interpretation is focused on observable trends and not on absolute values.

## 5.2 Amperometric detection of silver nanoparticle oxidation

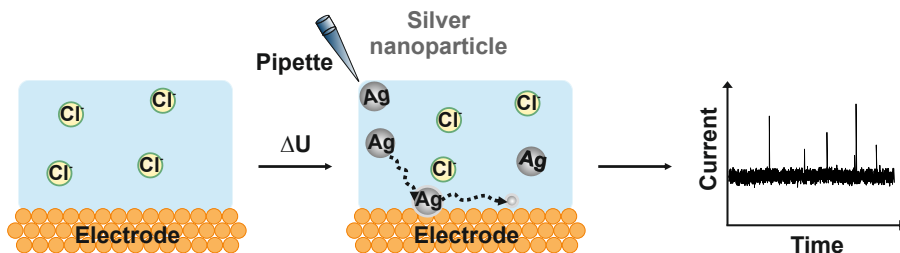


**Figure 5.3:** Scheme of the nano impact based electrochemical detection of silver nanoparticles and an exemplary current time trace recorded with the BioMAS measurement device used in this work.

For a typical nano impact experiment the reservoir of a MEA chip is filled with electrolyte, the electrodes are biased to 0.4 V vs. Ag/AgCl and the AgNPs inserted into the reservoir. Upon collision with the electrode the AgNPs are oxidized, resulting in oxidative current peaks in the current time trace as depicted in Figure 5.3. The oxidative dissolution of silver nanoparticles can follow different chemical reaction pathways and the propagation of the dissolution process is either charge transfer- or diffusion rate-limited [12,200]. The different oxidation pathways are given by the following equations together with their standard potential in V reported vs. NHE [201]:



The standard potential of the Ag/AgCl reference electrode is 0.222 V and can be used for converting the potentials from NHE to Ag/AgCl [202]. For measurements in chloride containing electrolytes, silver oxidation and formation of silver chloride is the dominant pathway [30,145]. An exemplary current time trace recorded in PBS can be seen in Figure 5.4A. The green part of the trace corresponds to the background current arising from electronics and the electrochemical cell in absence of AgNPs and is used for calculating the current noise level. A control measurement in absence of any particles was performed every time before starting a new measurement series or before using a different chip. Evaluation of the noise behaviour is crucial to provide a reproducible and reliable peak detection based on the current rms. The insertion of nanoparticles generates a large capacitive spike indicated by the black arrow and after 2 s relaxation time the actual nanoparticle oxidation impacts are recorded (blue) [27]. Figure 5.4B shows a single oxidation peak with three characteristic features: peak amplitude, peak duration and the transferred charge given by the area under the peak. The negative peak after the main peak is an artefact originating from the circuit design and explained in

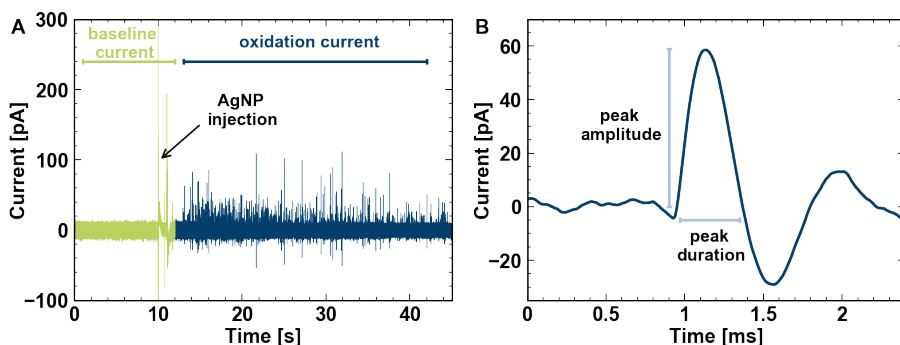


**Figure 5.4:** A) Exemplary current time trace of AgNP oxidation with baseline current used for determination of rms (green), capacitive peak due to NP insertion (black arrow) and analyzed oxidation current (blue). B) Zoom in single oxidation peak. Potential = 0.4 V vs. Ag/AgCl, electrolyte = PBS (100 mM NaCl).

more detail in subsection 3.2.4. The peak amplitude and the transferred charge depend on the particle size, whereas the average peak duration was found to be 0.4 ms independent of the particle size. Equation 3.1 allows for calculation of the nanoparticle diameter [17, 27]. A premise for such calculations is complete oxidation with a single electrode contact. For silver nanoparticles with a diameter of 10 nm this is commonly agreed to be true, whereas larger particles undergo multiple incomplete oxidation events [29, 203–205]. Therefore, all current peaks reported in this work are considered to correspond to individual nanoparticles hitting the electrode. Figure 5.5 shows the mean impact frequency per chip for different concentrations of AgNPs ranging from 0 to 60 pM and the corresponding diameters calculated from the impact charge. Measurements were performed 5 times for 40 s for each concentration at a potential of 0.4 V vs. Ag/AgCl, which is sufficiently high for immediate nanoparticle oxidation upon electrode contact. From the lowest measured concentration up to concentrations of 15 pM, the impact frequency increases linearly as indicated by the linear fit in the inset ( $R^2 = 0.99$ ). For concentrations above 20 pM, the number of impacts/s saturates. A fit for concentrations up to 40 pM still shows good linear relationship with a slightly lower  $R^2$  value of 0.93. As explained in section 2.3, the nanoparticle transport to the electrode is based on diffusion. Thus, the probability of a single nanoparticle colliding with the electrode is determined by its diffusion coefficient and the geometrical design of the electrode. In case of measurements of longer time periods on microelectrodes, the current is expected to approach steady-state with a linear relationship between current and concentration (see subsection 2.1.5). For measurements in sufficiently concentrated chloride based electrolytes ( $c > 50$  mM), a limitation by the diffusion of AgNPs to the electrode is expected, which explains the linear scaling of the impact frequency with the concentration as reported previously [27, 128, 129, 145]. However, this is only true if the diffusive pathways of individual particles are independent [140]. For larger particle concentrations, the chances of particle-particle interactions increase, which

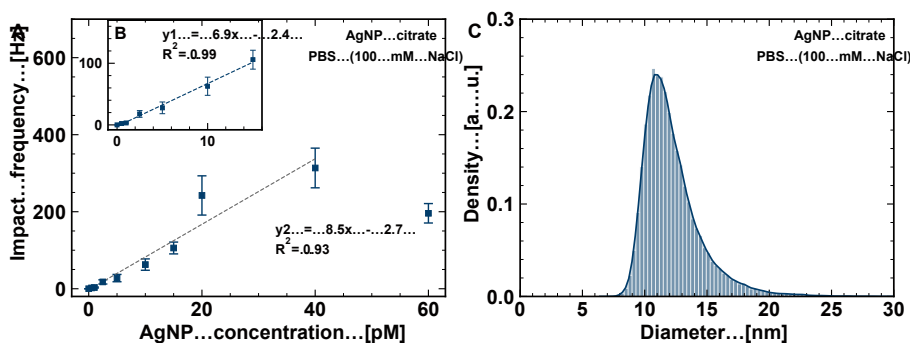


**Figure 5.5:** A) Mean impact frequency per chip for different concentrations of AgNPs with linear fit. B) Zoom and fit of linear part from 0 to 15 pM AgNPs. C) Density estimation plot and histogram of nanoparticle diameters calculated from impact charge (potential = 0.4 V vs. Ag/AgCl, electrolyte = PBS (100 mM NaCl)), mean diameter =  $12 \pm 2$  nm.

can be an explanation for the observed saturation. Particles can cluster together, generating fewer but larger oxidation peaks [206]. Consequently, the size distribution shifts to larger diameters and the number of impacts decreases. Additionally, the evaluation algorithm relies on the detection of impacts at separate time intervals. With increasing impact frequencies, the likelihood of two particles hitting the electrodes at the same time increases, which can result in incorrect impact numbers. This limits the maximum detectable nanoparticle concentration. Another factor that has to be considered for impact based detection is competitive adsorption of particles on the passivation layer used for electrode fabrication, which covers the largest part of the chip. This adsorption has been observed for organic polymeric passivation layers and could be decreased by surface modifications with thiolated molecules [27, 144]. A change to inorganic passivation materials such as  $\text{Ta}_2\text{O}_5$  could further minimize adsorption due to a change in the surface polarity. The  $\text{Ta}_2\text{O}_5$  passivation top layer fabricated by ALD exhibits a negative surface zeta potential ( $-62$  mV, pH = 7.4, 1 mM KCl [207]). Therefore, the negatively charged AgNPs are repelled due to electrostatic repulsion, which decreases the amount of nanoparticle adsorption.

As already mentioned, with the charge transferred during a nanoparticle impact it is possible to calculate the nanoparticle diameter. Figure 5.5B shows the histogram and corresponding density estimation plot for the diameters calculated from 45000 individual impacts for a nanoparticle concentration of 23 pM. The size distribution features a peak maximum at 11 nm and the mean diameter is  $12 \pm 2$  nm. This is in accordance with the size distribution provided by the supplier and the results obtained via STEM. Overall, the sizes derived from impact electrochemistry range from 8 to 25 nm in diameter. Notably, the size distribution is asymmetrical with a sharp drop for diameters below 10 nm. Reason for this is a detection limitation originating from the peak detection algorithm and the current noise level of the measurement setup [27]. With an average rms current noise of 2 pA, the peak current has to be larger than

20 pA for being successfully identified as an impact. The minimum detectable peak charge can be estimated according to the following equation:

$$Q_{min} = \frac{1}{2} \cdot 20 \text{ pA} \cdot 0.4 \text{ ms} = 4 \cdot 10^{-15} \text{ C}$$

assuming a triangular peak shape. Equation 3.1 gives a lower size detection limit of 9.3 nm, which fits well to the experimentally measured size distribution. The particle diameters up to 25 nm can be attributed to larger particles, occurring during the synthesis procedure, or particle aggregates [140]. The critical coagulation concentration of NaCl for silver nanoparticles is  $\approx 48$  mM [150]. Thus, for measurements in PBS (100 mM NaCl) particle aggregation is inevitable as also evidenced by UV-Vis measurements (see chapter 4).

Overall, an approximately linear relationship between impact frequency and the nanoparticle concentration was found. This demonstrates that the reported measurement technique is suitable for nanoparticle quantification, which has been reported previously [27, 145].

### 5.3 Comparison between citrate- and DNA-capped nanoparticles

In order to investigate the effects of DNA-AgNP conjugation on the amperometric detection of nanoparticle oxidation, different DNA-AgNP conjugates were probed and compared to citrate-capped AgNPs. In total five different ssDNA strands with low NP:DNA ratios (1:50 and 1:100) from at least three individual nanoparticle modifications were tested to ensure reproducibility. Figure 5.6A shows the mean impact frequency per chip for citrate-capped and DNA-capped AgNPs (average of 10mer, 13mer and 17mer) as a function of applied potential measured in PBS with 200 mM NaCl. The influence of the different DNA length will be discussed in detail in section 5.5. When comparing the potential dependent frequencies no impacts for both particle types can be observed for a potential of 0 V. Increasing the applied potential to 0.2 V results in  $\approx 100$  impacts/s for citrate-capped particles whereas no impacts are detectable for DNA-capped nanoparticles. Another increase to 0.4 V generates measurable current peaks for DNA-capped AgNPs. Upon further increasing the potential to 0.6 V and 0.8 V, the impact frequency for DNA-capped nanoparticles increases with potential. For citrate-capped AgNPs, the value stays almost constant over the complete potential range once the overpotential is sufficient to drive silver oxidation. In the lower potential range (0.2-0.4 V) the impact frequency for DNA-capped AgNPs is decreased in comparison to citrate-capped AgNPs. For 0.6 V the values are in the same range and for the highest potential the impact frequency for DNA-capped AgNPs is even higher than for citrate as capping agent. A comparison of the impact frequencies for the different particle capping demonstrates, that the DNA modification induces a decrease of the impact frequency in the lower potential range.



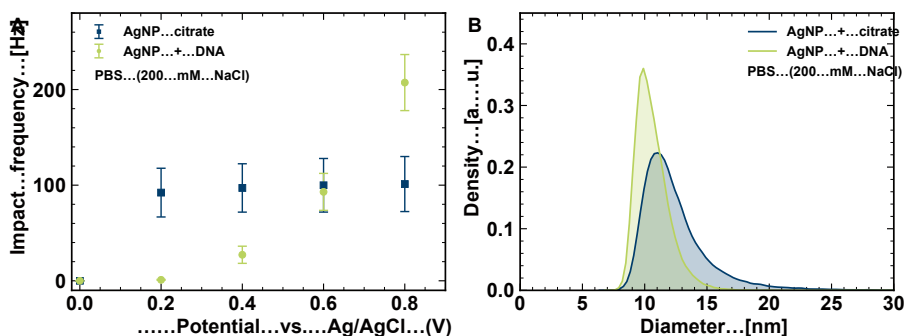


**Figure 5.6:** A) Mean impact frequency per chip for citrate- and DNA-capped AgNPs with a variation in applied potential ( $c_{\text{AgNP}} = 23 \text{ pM}$ , electrolyte = PBS (200 mM NaCl)). B) Density estimation plot of nanoparticle diameters for citrate- and DNA-capped AgNPs calculated from impact charge (potential = 0.4 V vs. Ag/AgCl, electrolyte = PBS (200 mM NaCl)).

In the following this observed lower activity of DNA modified nanoparticles will be discussed. Remarkably, this is already the case for relatively low DNA loadings (here:  $\approx 20$  strands/NP). Such an influence of DNA on the silver oxidation during collision experiments has already been reported and our results confirm this finding [22]. The attached DNA strands are longer and bulkier than the citrate molecules and a single molecule covers a larger fraction of the surface. As a consequence, the electrochemically accessible surface area is reduced, which influences time and quality of the particle-electrode contact [22, 31, 33]. The DNA shell surrounding the nanoparticles can reduce the chance of AgNPs reaching the tunnelling distance of the electrode [21, 151]. Accordingly, the charge transfer rate decreases due to a reduced probability for tunnelling [114, 138, 208]. Furthermore, the silver oxidation pathway could be influenced. For measurements in chloride containing electrolytes, AgNPs are oxidized to AgCl according to the following equation:



The reaction pathway consists of different processes involving chloride ions such as the diffusion of chloride ions to the particle surface (1), the nucleation and growth of AgCl (2), the diffusion of chloride ions through a shell of solid AgCl surrounding the AgNP (3) or the solubility of the reaction product AgCl in direct vicinity to the electrode (4) [30, 31]. An important aspect to mention here is that nanoparticles are influenced by their local environment and in turn also change this environment. According to the Guoy-Chapman model, nanoparticles with charged ligands attract counterions forming a diffuse cloud of charges. For negatively charged ligands such as citrate or DNA, this results in the depletion of negatively charged ions (e.g.  $\text{Cl}^-$ ) in proximity to the nanoparticle [165]. With a higher negative charge, the

DNA shell on the particle surface could also act as electrostatic barrier, hampering diffusion of negatively charged  $\text{Cl}^-$  to the particle surface to a much greater extent than the citrate shell [209]. Additionally, the DNA could introduce steric hindrance, impeding ion diffusion to and from the nanoparticle [210,211].

In order to understand the dependence of the impact frequency on the applied potential, it is necessary to have a closer look on the electrochemical standard potential. It depends on the chloride concentration and can be calculated according to the following equation assuming a chloride concentration of 3 M in the Ag/AgCl reference electrode:

$$E(0.2\text{ M}) = 59\text{ mV} \cdot \log\left(\frac{0.2}{3}\right) = 69\text{ mV vs. Ag/AgCl}$$

From this it can be seen that at 0 V no nanoparticle impacts should be observed due to the potential being below the electrochemical standard potential. This is the case for the investigated system. For a potential of 0.2 V the overpotential is high enough to oxidize citrate-capped AgNPs as indicated by the observed current peaks. This onset potential for citrate-capped AgNP oxidation is in accordance to literature results, where values above 100 mV are necessary for reliably detectable AgNP oxidation [145]. The constant and potential independent impact frequency indicates limitation by the diffusion of AgNPs to the electrode, which is expected for measurements in high salt concentrations [30]. For DNA capped-AgNPs at an applied potential of 0.2 V, the overpotential is either not sufficient to drive silver oxidation or the current peaks are masked by the background noise due to incomplete oxidation. Furthermore, the oxidation rate could be slower than the electrode-contact time and not every collision causes AgNP oxidation [31]. The first impacts can be observed for a potential of 0.4 V, demonstrating that a higher overpotential (more positive potential) is required for the oxidation of DNA-AgNP conjugates. Charge transfer tunnelling depends not only on the distance but also on the applied overpotential. An increase in potential results in an increasing potential drop at the electrode, providing a higher driving force to the occurring reaction. Consequently, the charge transfer rate increases with overpotential and thus also the impact frequency [12,38,212]. This behaviour has already been reported for stripping voltammetry of AgNPs modified with 2000 bp DNA, but due to 100 times larger DNA fragments direct comparison is difficult [33].

Figure 5.6B shows the density estimation plots for the diameters calculated from the charges of 50000 individual impacts. The size distribution for DNA-capped AgNPs shows a narrow distribution with a mean diameter of  $11 \pm 1$  nm. The distribution for citrate-capped AgNPs is broader and shifted towards larger diameters with a mean diameter of  $12 \pm 3$  nm. The size distribution for DNA-capped nanoparticles reveals, that once the applied potential is sufficient for driving silver oxidation, the particles undergo complete oxidation in a single electrode contact. At an applied potential of 0.8 V the impact frequency for DNA-capped AgNPs is even higher compared to citrate-capped AgNPs. Intuitionally, one would expect higher impact

frequencies for the citrate-particles due to easier oxidation, which is not the case. Reason for this is the salt-induced aggregation of citrate-capped AgNPs, as evidenced by the broader size distribution and the shift towards larger nanoparticle diameters. Large aggregates sediment before reaching the electrode and overall the impact frequency decreases [70, 169]. As reported in chapter 4, DNA-AgNPs exhibit an increased resistance to aggregation, which matches well with their narrow size distribution. The increased stability could be of importance for measurements in biological media with typically relative high salt concentrations and could overcome the limitations for citrate-capped AgNPs [213].

The reported observations illustrate, that a nanoparticle surface modification with DNA has crucial influence on the oxidation behaviour of AgNPs, even for already relatively low surface loadings. Charge transfer is diminished and the CT rate shows a strong dependence on the applied overpotential indicating a limitation by charge-transfer tunnelling. In case of citrate-capping the impact frequency is constant and thus diffusion-limited. This conforms to the expected behaviour for measurements at high overpotentials and high salt concentrations.

## 5.4 Influence of supporting ion identity and concentration

The impact frequency for stochastic nanoparticle collision experiments depends on the identity and the concentration of the supporting ions as well as on the applied potential. For citrate-capped AgNPs different studies have investigated the influence of the mentioned parameters in detail. Especially, the concentration of chloride ions and the conductivity of the medium were found to play a crucial role [30, 31, 212]. After having demonstrated that the introduction of DNA substantially changes the oxidation behaviour, it is likely that also the influence of the afore-mentioned parameters is different. To gain insight into this behaviour, the experiments were repeated with a concentration of 100 mM NaCl in the electrolyte and in 100 mM NaNO<sub>3</sub>. Again, the values for the DNA modified AgNPs represent an average over the results for 10mer, 13mer and 17mer. Figure 5.7A compares the mean impact frequency per chip for citrate-capped and DNA-capped AgNPs as a function of applied potential in the presence of 100 mM NaCl. Notably, the impact frequencies for DNA-capped AgNPs are much lower compared to citrate-capped AgNPs and to measurements for DNA-capped AgNPs in 200 mM NaCl (see Figure 5.6). When comparing the potential dependent frequencies, no impacts for both particle types can be observed for a potential of 0 V. Increasing the applied potential to 0.2 V results in  $\approx 120$  impacts/s for citrate-capped particles, whereas no impacts are detectable for DNA-capped nanoparticles. Another increase to 0.4 V generates measurable current peaks for DNA-capped AgNPs, while the frequency for citrate-capped AgNPs stays nearly constant. Upon further increasing the potential to 0.6 V and 0.8 V, the impact frequencies for both, citrate and DNA-capped nanoparticles increase with potential.

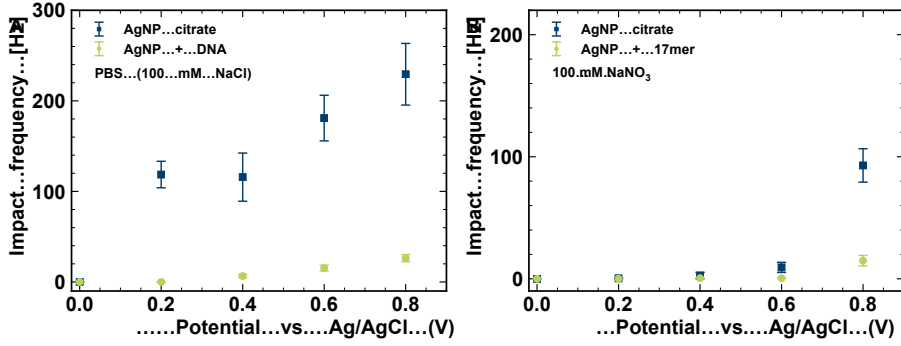


**Figure 5.7:** Mean impact frequency per chip for citrate (blue) and DNA-capped (green) AgNPs in PBS buffer containing 100 mM NaCl (A) and in 100 mM NaNO<sub>3</sub> (B) and different oxidation potentials ( $c_{\text{AgNP}} = 23 \text{ pM}$ ).

The most apparent observation for DNA-capped AgNP oxidation in 100 mM NaCl is a decrease of the impact frequencies over the complete potential range compared to the measurements in higher concentrated chloride solutions reported in the previous section (see Figure 5.6). This indicates suppression of the oxidation process for lower NaCl concentrations. Consequently, the charge transfer rate critically depends on the chloride concentration. With the impact frequency depending on the applied potential, the process is charge transfer rate-limited. Interestingly, also the impact frequencies for citrate-capped AgNPs increase for raising the potential from 0.4 V to 0.8 V. This indicates that the investigated oxidation process is not exclusively controlled by diffusion of AgNPs to the electrode in this potential range, since diffusional impacts are considered as potential-independent as it is the case between 0.2–0.4 V [30,214]. Reason for this observation could be the occurrence of an alternative reaction pathway, which is charge-transfer limited. This behaviour will be further elucidated in the following.

For measurements in NaNO<sub>3</sub> (Figure 5.7B), the first AgNP impacts can be observed at an applied potential of 0.6 V for citrate and 0.8 V for DNA-capped AgNPs. For citrate-capped AgNPs, the impact rate increases to  $\approx 100$  impacts/s with increasing potential, which is in the same range as for oxidation in chloride containing electrolytes. As already observed for measurements in the presence of chloride, the impact frequency for DNA-capped AgNPs is strongly decreased in comparison to citrate capping. The fact that oxidation impacts can be observed in chloride free electrolytes proves that both citrate and DNA-capped AgNPs can be oxidized following an alternative pathway.

Considering the onset potential between 0.6 and 0.8 V the oxidation takes place via the formation of  $\text{Ag}^+$  according to:



Once the overpotential is sufficient for AgNP oxidation, the impact frequencies for citrate-capped AgNPs are comparable to the chloride based oxidation. For DNA-capped AgNPs the impact frequency is again much lower when compared to citrate-capped AgNPs. This evidences that the DNA also blocks this reaction pathway without participation of any electrolyte phase reactant and thus the overall charge transfer process. With the results for measurements in  $\text{NaNO}_3$ , it is now also possible to fully explain the observations for citrate-capped AgNPs in 100 mM NaCl. The onset potential of 0.6 V for oxidation with  $\text{Ag}^+$  as reaction product matches with the potential-dependent impact behaviour reported in Figure 5.7A. Thus, it can be assumed that the nanoparticle oxidation in 100 mM NaCl takes place via two different reactions. For potentials up to 0.4 V the chloride based pathway is dominating. In case of higher overpotentials, chloride-free oxidation starts, which is potential-dependent. Due to the additionally generated impacts, the overall frequency increases with applied overpotential. This behaviour can not be observed for measurements in 200 mM NaCl, since sufficient chloride is provided and the chloride based oxidation dominates over the complete potential range [30, 145].

The reported results reveal that a decrease in sodium chloride concentration from 200 to 100 mM has a strong influence on the oxidation behaviour of DNA-capped AgNPs. Since the increment is rather large it is not possible to give a definite value for the NaCl concentration at which the activity for DNA-capped AgNPs is reduced or where citrate-capped AgNP aggregation becomes relevant. In order to identify the optimum NaCl concentration range for DNA- and citrate-capped AgNPs, the impact frequency was measured as a function of the NaCl concentration in the range from 1 to 400 mM. The findings for citrate and 17mer-capped AgNPs (ratio NP:DNA 1:100) are given in Figure 5.8. The 17mer was chosen despite the secondary structure in the DNA strand because it exhibits higher oxidation activities over a wider range of DNA concentrations. A certain level of redox activity is necessary in order to ensure reliable detection and sufficient impacts for data evaluation. A potential dependent measurement confirmed that the 17mer also follows the previously described trend with strongly increasing frequencies for higher overpotentials comparable to the results for the other strands (see Appendix Figure 8.13). Due to variations in the impact frequency with different MEA chips, the results for one measurement series are normalized with the maximum value for this series, resulting in a value of 1 for the respective impact frequency at this concentration. A zoom in the lower concentration range can be found in Figure 8.12. The overall trend for both ligands can be described as an increase in impact frequency with NaCl concentration until reaching a plateau followed by a decrease with further increasing NaCl

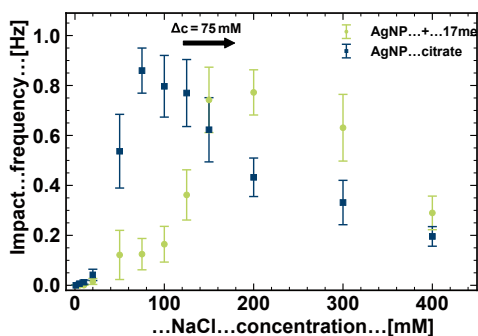


**Figure 5.8:** Mean impact frequency per chip (normalization by maximum number of impacts) for oxidation of citrate- and DNA-capped AgNPs with varying concentration of NaCl in the electrolyte ( $c_{\text{AgNP}} = 23 \text{ pM}$ , potential = 0.4 V).

concentration. The onset concentration for the observation of impacts for citrate-capped AgNPs is 5 mM NaCl. The impact frequency increases slightly until 20 mM followed by a strong increase for a concentration increment from 20 to 75 mM. From 75 to 125 mM the impact frequency stays almost constant and decreases continuously for concentrations of 150 mM and higher. For DNA-capped AgNPs the onset concentration is 20 mM NaCl followed by a slight increase until 100 mM. Increasing the NaCl concentration from 100 to 150 mM results in a strong increase in impact frequency followed by a plateau until 200 mM. For higher concentrations the frequency decreases. Overall, the impact frequencies for DNA-capped AgNPs are shifted towards higher concentrations by about 75 mM with respect to the results for citrate-capped AgNPs.

The low impact frequencies for NaCl concentrations below 20 mM have been reported previously and are caused by the mass-limited chloride diffusion to the nanoparticle [30]. This generates a reduction in peak amplitude together with an increase in width and the peaks can not be distinguished from the background current. The effect becomes more pronounced for smaller nanoparticles. Increasing the chloride concentration results in a strong increase in impact frequency up to 75 mM for the citrate-capped AgNPs. This can be attributed to a dependence on the electrolyte conductivity up to values of around 0.75-1 S/m [30]. From 75 to 125 mM NaCl, the impact frequency stays almost constant despite a minor decrease for the higher concentrations. In this range, the chloride concentration is sufficiently high and the process is limited by the nanoparticle diffusion to the electrode [30,140]. The minor decrease between 75 and 125 mM marks the onset for salt-induced aggregation [150,169]. As confirmed by UV-Vis measurements (see Appendix Figure 8.11), this effect becomes more distinct upon further increasing the salt concentration. Accordingly, the impact frequency decreases continuously from 125 to 400 mM. An additional process reducing the impact frequency is the mentioned particle adsorption at the electrode passivation. The likelihood of adsorption for electrostatically stabilized nanoparticles is expected to increase with increasing electrolyte

concentration. This is a result of decreased electrostatic repulsion and the Van der Waals attraction becomes dominant [140,165]. This expectation can be confirmed by having a look on the surface charge of the Ta<sub>2</sub>O<sub>5</sub> passivation. In very dilute electrolytes, the zeta potential is around -60 mV and decreases to around -20 mV for 100 mM NaCl [207,215]. Increasing the chloride concentration should further decrease the zeta potential (closer to zero) and accordingly the electrostatic repulsion between passivation and nanoparticles decreases.

The impact frequency for DNA-capped AgNP increases almost linearly until 100 mM NaCl. As reported for the citrate particles this is caused by an increase in conductivity. However, the slope is much lower than for the citrate-capped AgNPs. This matches well with the observed strong suppression of the oxidation for the DNA-AgNP conjugates for measurements in 100 mM NaCl. Therefore, it can be suggested that the impact frequency for DNA-capped AgNPs increases as well with increasing conductivity. However, this increase is countered by a large depletion zone of chloride around the nanoparticles and slow charge transfer kinetics. Additionally, the rigidity of single stranded DNA, characterized by the persistence length, is influenced by the ionic concentration [216,217]. At lower salt concentrations, the electrostatic interactions between charged chain segments prevail, resulting in an increased chain rigidity and a more stretched conformation [218,219]. This can induce suppression of charge transfer processes. Upon increasing the ionic strength of the solution, the electrostatic interactions are screened and the persistence length decreases [217]. This reduces the spatial extension of the DNA shell and enables closer electrode contact. Therefore, charge transfer is facilitated, which could explain the increase in impact frequency with increasing salt concentration. From 100 to 150 mM NaCl, the impact frequency increases strongly. The conductivity in this range is already relatively high and should not be the limiting factor. Most likely, the strong increase is a result of accelerated charge transfer combined with a compression of the chloride depletion zone around the charged nanoparticle surface [165] and the described change of the DNA rigidity. The plateau from 150 to 200 mM NaCl indicates a limitation by particle diffusion. The decrease in impact frequency for higher chloride concentrations can be again attributed to adsorption processes at the passivation layer. However, the decrease is slower due to a higher resistance to elevated chloride levels for DNA-capped AgNPs. Furthermore, it can be assumed that additional processes are involved for DNA-capped AgNPs. As already mentioned, single stranded DNA undergoes compaction at elevated salt concentrations or even collapses into a condensed phase. Reason for this is screening of the negative charges in the phosphate backbone, resulting in non-native base pairing and secondary structure formation [220,221]. The resulting compact DNA shell could be too dense for charge transfer or the diffusion of ions, which decreases the impact frequency.

In summary, the optimum chloride concentration for detection of citrate-capped AgNPs is between 75-100 mM and 150-200 mM for DNA-capped AgNPs. This allows a precise adjustment of the chloride concentration according to the special needs of differently functionalized nanoparticles. With this, the impact frequency can be maximized by avoiding adverse effects

such as aggregation or adsorption. Overall, the results highlight the importance of the chloride concentration for the amperometric detection of silver oxidation and the need for careful adjustment of the electrolyte composition. The observed lower impact frequencies for DNA-capped AgNPs support the strong influence of DNA on the oxidation of silver nanoparticles by hampering charge transfer.

## 5.5 Influence of DNA density and length

As evidenced in the previous section, the oxidation behaviour of AgNPs is strongly influenced by a surface modification with ssDNA. In an attempt to identify the effect of the surface strand density on the oxidation behaviour, varying initial DNA concentrations were tested during nanoparticle modification. Additionally, DNA strands with different numbers of nucleotides were conjugated to silver nanoparticles to investigate the influence of the ligand length. Overall, AgNP-DNA conjugates with four DNA strands, different in length and sequence, and eight initial DNA concentrations were prepared as described in chapter 4. All results reported in this section are derived from at least three individual nanoparticle modifications. Figure 5.9 shows the mean impact frequency per chip plotted against the initial DNA concentration during NP modification for 10mer (A), 13mer (B), 20mer (C) and 26mer (D). The experiments were performed in PBS buffer containing 100 mM NaCl and for an applied potential of 0.4 V and 0.8 V vs. Ag/AgCl. The shaded areas indicate impaired particle stabilities due to low DNA loadings and the addition of large amounts of TCEP for higher DNA concentrations. For all four DNA strands, the highest impact frequencies can be observed in the low concentration range from 0.06 to 0.3  $\mu\text{M}$ . For the short strands (10mer, 13mer), the modification at the lowest ratio did not work (see Table 4.1) and thus no impacts could be measured. With increasing DNA concentration, the impact frequencies decrease and drop to almost zero for concentrations above 1  $\mu\text{M}$ . This overall trend can be observed for both investigated potentials. The impact frequencies measured for high concentrations for 20mer and 26mer originate from problems with the modification as explained in chapter 4. In the low concentration range, the impact frequencies are influenced by the applied potential and increase with a higher overpotential, which is in accordance to the previous results. Comparing the impact frequencies for the different DNA strands at a concentration of 0.3  $\mu\text{M}$  DNA (2nd point from left side) reveals overall lower values for the two longer DNA strands (C+D). The results reported in section 4.2 allow for correlating the DNA concentration with the surface strand density and higher initial DNA concentrations during modification result in AgNP-DNA conjugates with higher surface strand densities. All four plots of impact frequency versus initial DNA concentration show a decrease in AgNP oxidation with higher DNA concentrations during modification. This is in accordance to literature findings for silver nanoparticles modified with aptamers and indicates that a higher density of DNA strands



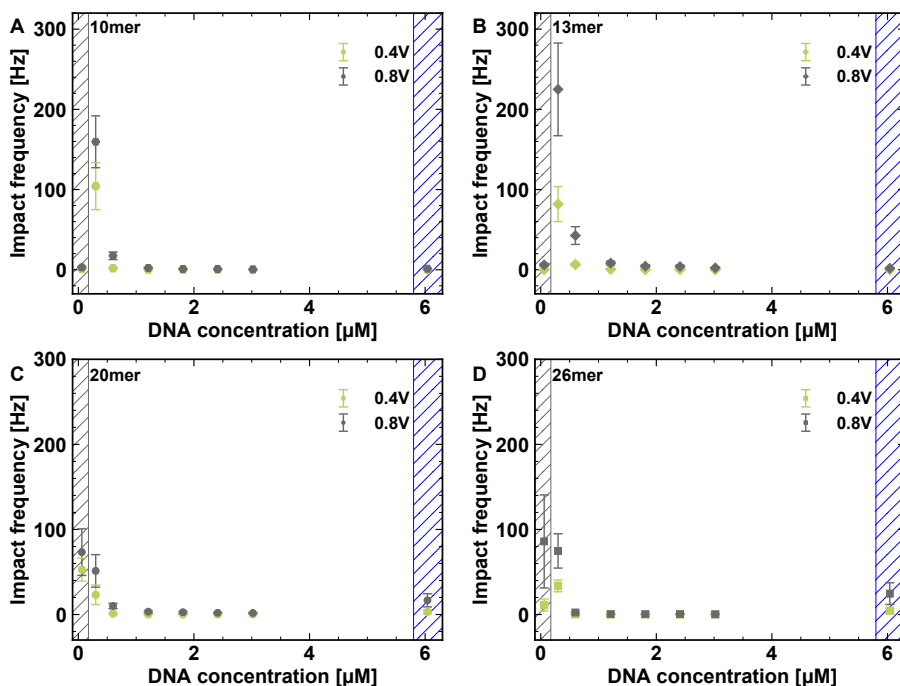


**Figure 5.9:** Mean impact frequency per chip for different concentrations of DNA during AgNP modification with an applied potential of 0.4 V (green) and 0.8 V (grey) vs. Ag/AgCl. A) 10mer, B) 13mer, C) 20mer and D) 26mer, electrolyte = PBS (100 mM NaCl), ( $c_{\text{AgNP}} = 23 \text{ pM}$ ). Shaded areas indicate low particle stability due to low DNA loadings (grey) and the addition of TCEP (blue).

on the nanoparticle surface diminishes the electrochemical oxidation of AgNPs [22]. With more DNA molecules on the surface, a larger surface area is insulated, which hampers the tunnelling probability [22, 151]. Additionally, the shell at high DNA densities is very compact and the transport of chloride ions to the nanoparticle surface could be inhibited. Above a certain DNA loading charge transfer seems to be completely blocked and no oxidation impacts can be observed. Even a higher overpotential is not sufficient to overcome the potential barrier and the redox activity of the AgNPs can not be restored. This confirms, that high DNA loadings on the AgNPs induce very efficient blocking of charge transfer.

Interestingly, the concentration dependent decrease in impact frequency is independent of the DNA length. In general, tunnelling is distance dependent and the charge transfer rate decreases with increasing particle electrode spacing [114, 132, 138, 144]. Introduction of an insulating layer, such as a SAM of  $\gamma$ -alkanethiols, usually blocks charge transfer between the electrode and a solution phase redox species and is commonly used as insulating back-fill [208, 222, 223]. For self-assembled monolayers of ssDNA on gold electrodes, a similar insulating behaviour has been reported [224]. However, for metal/insulator/metal assemblies

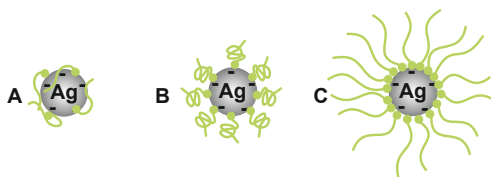


**Figure 5.10:** Scheme of different configurations for ssDNA attached to a nanoparticle surface (adapted from ref. [185]).

**Table 5.4:** Calculated extension of different DNA configurations. The value of contour length includes 1 nm for the thiol anchoring group [185].

Ligand	Nucleotides	Contour length $L_c$ [nm]	Diameter [nm] (from $R_g$ )
citrate	-	layer thickness 0.8-1.4 nm [231]	
10mer	10	5.3	3.0
13mer	13	6.6	3.4
20mer	20	9.6	4.1
26mer	26	12.2	4.6

very efficient distance-independent charge transfer rates for separation distances up to several nanometres have been reported [223, 225–227]. Therefore, one could expect differences in the oxidation behaviour in particular between the shorter and the longer DNA strands, which is only the case for low DNA loadings. In order to understand this observation, it is necessary to have a closer look on the conformation and spatial extension of the ssDNA on the nanoparticle surface. Overall, three limiting DNA conformations can be assumed, which are depicted in Figure 5.10 [185]. The DNA strands can be wrapped around the nanoparticle with the main anchoring via the thiol group (A). Additional contacting points are a result of non-specific binding of individual nucleotide bases and the DNA strands lie flat on the NP surface [102, 228, 229]. This will be mostly the case for low DNA loadings. Binding via the thiol group is stronger than the non-specific interactions and thus covalent attachment is favoured. Due to entropic reasons, the free DNA tail will adopt a random coil form in case of no steric limitations (B). Since the formation of a thiol bond is thermodynamically favoured, as many strands as possible are attached via the thiol group. This reduces the non-specific binding. At a certain DNA loading the strands have to compete for binding sites. In order to pack as many DNA strands per area as possible, the molecules adopt a stretched conformation (C), which will be the case for high DNA loadings. Presumably, a combination of the models B+C will be the best description of what happens in reality for higher DNA loadings [185, 230].

The approximate spatial extension of the DNA strands can be calculated, which can give an estimation of the thickness of the DNA shell and thus the minimum separation distance to

the electrode. For each of the three models different parameters have to be considered for the calculations. In case of DNA wrapping the nanoparticle (A), the thickness of the shell can be represented the best by the diameter of the DNA strand, which is independent of the DNA length. With a cross-sectional radius of 0.6-0.7 nm [184] and assuming a length of 1 nm for the thiol anchoring group [185], the thickness is approximately 2 nm. For a random coil conformation (B), the spatial extension can be assumed as two times the radius of gyration  $R_g$ . This parameter describes the size of an arbitrarily shaped object and can be calculated according to the following equation with the contour length per base  $L_b$  of 0.43 nm and the persistence length  $L_p$  of 1.3 nm [232, 233]:

$$R_g = \sqrt{\frac{L_b \cdot L_p}{3}}$$

The persistence length is a measure of rigidity and describes the distance over which the strand behaves like a rigid rod. For ssDNA, the value is around 1 nm in contrast to approximately 50 nm for dsDNA [234]. The extension of stretched DNA (C) corresponds to its contour length  $L_c$  given as product of the number of nucleotides and the contour length per base  $L_b$  in addition to the length of the thiol anchor [185]. Table 5.4 summarizes the calculated values for the four DNA strands and an estimation for the thickness of the citrate shell as reference. A comparison reveals that the spatial extension of conformation A is in the same range as the citrate shell. For all strands, the contour length is longer than 5 nm and the diameters are  $\approx 3$  nm and more. The threshold for a transition from distance-independent to distance-dependent and thus hindered charge transfer tunnelling for 10 nm nanoparticles has been reported to be in the range of 25  $\text{CH}_2$  groups [226]. This corresponds to 2.5-3 nm assuming  $\approx 0.1$  nm per  $\text{CH}_2$  group [227, 235]. A later study determined a distance of 2 nm as average insulating layer thickness [227]. These results are transferable to ssDNA layers, due to the insulating characteristic of ssDNA [224]. The reported values are in good agreement with the extensions for the citrate shell and DNA in a wrapped conformation. Considering

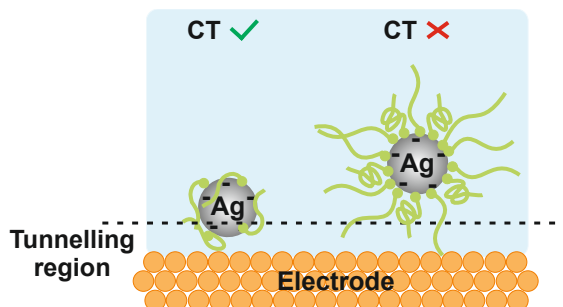


**Figure 5.11:** Scheme of charge transfer tunnelling for AgNPs with DNA modification and different strand conformation.

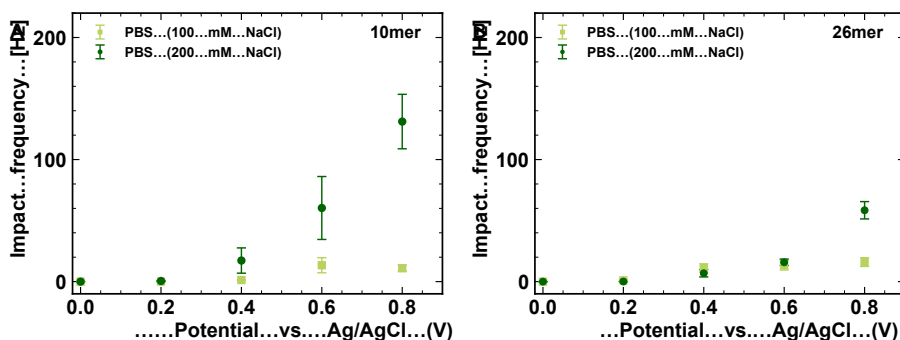


**Figure 5.12:** Mean impact frequency per chip for DNA-capped AgNPs in PBS buffer containing 100 mM NaCl (green) and 200 mM NaCl (darkgreen) and different oxidation potentials ( $c_{\text{AgNP}} = 23 \text{ pM}$ ) for A) 10mer and B) 26mer, (ratio 1:50,  $0.3 \text{ }\mu\text{M}$ ).

that nanoparticle oxidation can be observed in the low DNA concentration ranges, it can be assumed that the DNA strands at low DNA loadings adopt a conformation resembling to model A. With that, the AgNPs can reach within the tunnelling distance to the electrode and charge transfer is possible. For higher DNA loadings a mixture of random coil and stretched molecules is the most probable case. With DNA extensions of  $\approx 3 \text{ nm}$  and larger, the layer thickness is above the reported threshold and charge transfer is hindered. Accordingly, no nanoparticle oxidation can be observed. Since the diameter and the contour length for all four strands are already above the reported threshold of 2-3 nm, an influence of the DNA length can not be observed for higher DNA loadings. A schematic representation of the DNA conformation based charge transfer tunnelling is given in Figure 5.11.

The influence of the DNA length in the lower concentration ranges (conformation A) could be confirmed by potential and salt-dependent measurements as reported in section 5.4. The results for measurements of 10mer and 26mer (ratio 1:50) are given in Figure 5.12. For measurements in PBS buffer containing 100 mM NaCl, both AgNP-conjugates show overall low impact frequencies being almost constant over the measured potential range. With a higher salt concentration, the impact frequencies for the 10mer DNA increase strongly with applied overpotential as already reported previously. For the longer DNA strand (26mer), the values are almost the same up to a potential of 0.6 V and only increase for the last potential step to 0.8 V. Overall, the values for the longer strand are much lower as for the shorter one. For interpretation of this results, two different aspects have to be considered. First, the increased impact frequencies in 200 mM NaCl are a result of enhanced charge transfer as explained in detail in section 5.4. Second, the influence of the DNA length could be due to increased insulation. With a longer DNA strand, the probability for non-specific binding of nucleotides is higher, which could result in more contacting points and better insulation. Additionally, the described conformations are theoretical models. In reality the strands in conformation A

may overlap or a part is attached non-specifically and the rest points towards the surrounding solution. As a consequence, the shell will be heterogeneous and could be thicker at some points and thus closer to the limiting distance for tunnelling. For longer DNA strands the chances for such 'defects' increase and tunnelling could be hindered partly.

In summary, the presented results demonstrate that the initial DNA concentration during NP modification strongly influences the oxidation behaviour of silver nanoparticles. This influence is related with conformational changes of the DNA strands attached to the nanoparticle surface. Based on this findings a model for distance-dependent charge transfer tunnelling in presence of an insulating DNA film on the nanoparticles was developed.

## 5.6 Single stranded DNA with secondary structure

Experimental results from fluorescence spectroscopy indicate that one of the investigated DNA strands exhibits a secondary structure as described in subsection 2.2.2. Theoretical predictions revealed a stem-loop type motif. A detailed discussion of the possible DNA structures can be found in section 6.1. In order to explore if a secondary structure has an influence on the oxidation behaviour, the experiments, as reported in the previous section, were repeated for the 17mer strand. For this, AgNP-DNA conjugates with nine initial DNA concentrations were prepared as described in chapter 4. Again, all results reported in this section originate from at least three individual nanoparticle modifications. The measured concentration dependent impact frequencies for different potentials are given Figure 5.13. Again the shaded areas indicate impaired particle stabilities due to low DNA loadings and the large amounts of TCEP for higher DNA concentrations. Interestingly, the impact frequencies increase with concentration up to values ranging between 0.6 and 1.2  $\mu\text{M}$ . For higher concentrations the impact frequencies decrease until they drop to zero for values above  $\approx 5 \mu\text{M}$ . The threshold concentration for the drop in redox activity is much higher when compared to the other strands (1  $\mu\text{M}$ ). With increasing overpotential (0.8 V) the impact frequencies increase but the overall trend stays the same. This potential dependence is in accordance with previous results. In PBS buffer containing 200 mM NaCl, the impact frequency follows the previously described trend with strongly increasing frequencies for higher overpotentials comparable to the results from the 10mer strand (see Appendix Figure 8.13).

The initial increase in impact frequency could be associated with a lower colloidal stability of the AgNP-conjugates in the lower concentration range. The success rate for the modification reported in Table 4.1 serves as a good indicator for the particle stability and is indeed lowered for the 17mer. The density of DNA strands on the surface in this range is relatively low and possibly not sufficient to stabilize the nanoparticles against aggregation. Considering the findings in the previous section, these results are unexpected. Especially, since a length of 17 nucleotides ranks in between the two groups of short and long oligonucleotides. Out of

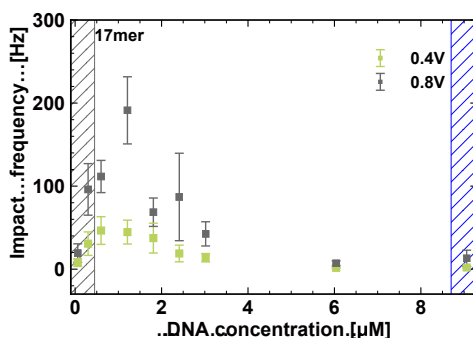


**Figure 5.13:** Mean impact frequency per chip for different concentrations of DNA during AgNP modification with an applied potential of 0.4 V (green) and 0.8 V (grey) vs. Ag/AgCl for 17mer DNA, electrolyte = PBS (100 mM NaCl), ( $c_{\text{AgNP}} = 23 \text{ pM}$ ). Shaded areas indicate low particle stability due to low DNA loadings (grey) and the addition of TCEP (blue).

the five investigated DNA strands, the 17mer is the only one exhibiting a secondary structure stem-loop motif. Such a folding induces formation of a compact configuration, which is in contrast to the flexibility of a single strand [112]. Accordingly, this stem-loop configuration is likely to be the reason for the differences in AgNP oxidation behaviour. A first evidence could be derived from an estimation of the spatial DNA strand extension. In the predicted structure, the stem-loop is located centrally in the sequence, which substantially shortens the strand. The length of the folded strand can be approximated with 8-10 nucleotides resulting in a contour length of  $\approx 3\text{-}5 \text{ nm}$ . With that it compares more to the shorter strands tested. This could also be an explanation for the low success rates for low DNA concentrations, which has also been observed for the 10mer strand. However, estimation of the extension for DNA secondary structure is difficult, due to a higher rigidity of double stranded DNA with much higher persistence length [234, 236, 237]. Giving predictions of the DNA conformation on the surface is complicated and the model described in section 5.5 might not be applicable. Experiments on the adsorption of single and double stranded DNA on AgNPs confirmed that also dsDNA can adsorb via the interaction of individual bases [228, 229]. Considering the single stranded dangling ends, the stem-loop could have additional contacting points via non-specific interactions and resemble a wrapped conformation. Additionally, it was found that the surface density on gold is lower for stem-loop DNA compared to ssDNA for preparation at identical conditions [238]. As a consequence, the surface density of 17mer on the AgNPs could be lower, inducing a shift of the threshold concentration for the drop in oxidation activity towards higher values. Furthermore, the charge transfer properties could change for DNA with secondary structure. Experimentally, it was possible to derive evidence for charge transfer through duplex DNA [239–241]. The conductive properties depend on a variety of parameters, such as sequence, DNA length, base pair interaction and stacking, and can be orders of magnitude higher for dsDNA in comparison to rather insulating ssDNA [239, 241–243]. Pre-

sumably, the different oxidation behaviour for DNA with secondary structure is caused by a complex interplay of several parameters such as DNA conformation and density and a change in charge transfer properties. In order to develop a better understanding of the underlying principles, further experimental investigations are necessary. Especially, data from additional strands with secondary structure would be required to permit systematic conclusions.

The results reveal a remarkably different oxidation behaviour of AgNPs capped with DNA bearing secondary structural motifs. This could be utilized as key detection element and holds potential for stochastic nanoparticle impact electrochemistry based DNA detection.

## **5.7 Summary**

To sum up, a detailed characterization of the measurement system and the experimental procedure revealed, that the system is stable and gives reproducible results. Additionally, the suitability for the detection of silver nanoparticles as small as 10 nm could be demonstrated. Possible limitations, such as MEA performance, have been identified and can be addressed in the future. For measurements with different nanoparticle concentrations, a linear relationship between nanoparticle concentration and impact frequency could be observed. This allows for nanoparticle quantification, which is an important feature for the development of a sensor. Successful particle detection is possible down to concentrations of around 2 pM. For future sensing applications, for example as redox tag, this could be used to generate a calibration curve for evaluation of unknown concentrations of analytes such as biomarkers, pathogens etc. [14]. To ensure reliable detection of individual impacts with this system, the nanoparticle concentrations should be adjusted to values between 5 to 40 pM. This gives rise to a sufficient number of impacts for data analysis and the particles do not interfere with each other. The lower detection limit is determined by the size of the electrodes, the measurement time, and the minimum number of oxidation events required for appropriate statistics. The detection limit could be improved by increasing the measurement time, however, this limits the experimental feasibility at some point [2]. Additionally, it has been demonstrated that the charge transferred during oxidation can be used for accurate nanoparticle sizing, which could be interesting for monitoring of aggregation or other processes altering the nanoparticle properties.

The comparison between citrate and DNA-capped nanoparticles highlights that the presence of DNA on the nanoparticle surface influences the oxidation behaviour of AgNPs in different ways. First of all, the DNA impedes the overall charge transfer during the NP/electrode contact. Reason for this is that the DNA shell prevents the nanoparticles from reaching within the tunnelling region and the overall process is charge-transfer limited. Additionally, the dependence on the electrolyte concentration suggests that the DNA strands influence the transport of chloride ions to the nanoparticle surface due to steric and electrostatic repulsion.

With respect to the experimental parameters, the results reveal that the established parameters for oxidation of citrate-capped AgNPs are not valid if DNA is present on the nanoparticle surface. The required activation overpotential is higher and elevated levels of NaCl are necessary. Investigations on the impact frequency as function of NaCl concentration validate different optimum concentration ranges for NaCl. For citrate-capped AgNPs, the highest impact frequencies can be observed in the range from 75 to 100 mM, whereas the maximum for DNA-capped AgNPs is located between 150 to 200 mM. Overall, this demonstrates that for successful and reliable nanoparticle detection, a careful selection and detailed characterization of the system is inevitable. The identified optimal conditions allow precise adjustment of the applied potential and the chloride concentration according to the requirements of the species under investigation. Thus, the oxidation rate and the likelihood of impacts can be optimized. This is of particular importance for the detection of DNA-modified nanoparticles, since any modification alters and reduces the oxidation activity.

Additionally, the initial DNA concentration during modification, which is directly linked with the density of DNA strands on the nanoparticle surface, has crucial influence on the electrochemical oxidation of silver nanoparticles. Depending on the surface loading, the strands adopt different conformations. As a consequence, the spatial extension of a DNA strand and accordingly the thickness of the overall shell around the nanoparticle changes. This influences the tunnelling probability since charge transfer tunnelling depends on the particle electrode spacing. For lower DNA densities, the suggested conformation is based on DNA strands wrapped around the nanoparticle. The thickness of the resulting shell is in the range, where tunnelling was found to be distance-independent. Upon contact with the electrode, charge transfer is possible and oxidation impacts can be observed. In case of higher densities, the most likely DNA conformation is a mixture of random coil and stretched strands. The formed shell is thicker than the reported threshold and a transition to distance-dependent tunnelling occurs. If an AgNP-conjugate gets in contact with the electrode, it can not reach within the tunnelling distance to the electrode and charge transfer is hindered. Accordingly, no oxidation impacts can be observed. With this findings it was possible to develop a DNA conformation based model for distance-dependent charge transfer tunnelling in presence of an insulating DNA film on the nanoparticles. Interestingly, this behaviour depends almost exclusively on the DNA conformation. For the investigated DNA lengths ranging from 10 to 26 nucleotides, an influence of the length of the DNA could be only observed in the lower concentration ranges. Longer DNA strands exhibit a higher insulating capacity and therefore decrease the extent of nanoparticle oxidation. Experimentally this implies, that nanoparticles with a large amount of DNA or very long DNA strands on the surface are difficult or almost impossible to detect via nanoparticle impact electrochemistry. Overall, the concentration window in which impacts can be observed is relatively narrow ( $\approx 0.5\text{--}1\text{ }\mu\text{M}$  initial DNA) independent of the DNA strand length. This can restrict the applicability for biosensing due to a loss of freedom in probe design. The behaviour strongly differs for DNA strands with internal



secondary structural motifs such as stem-loops. The DNA-AgNP conjugates can be oxidized over a wider range of initial concentration ( $\approx 0.5\text{--}3\text{ }\mu\text{M}$  initial DNA). Different factors can be responsible for this behaviour. First of all, the folding reduces the strand length compared to the values expected for the respective number of nucleotides. Furthermore, the surface density for stem-loop structures was reported to be lower, which could be the reason for a shift towards higher concentrations. Additionally, the charge transfer efficiency through the molecule increases for duplex DNA. The wider concentration window for measuring particle impacts is an attractive feature, which increases the flexibility in probe design and adjustment of DNA surface loadings.

In conclusion the presented results enable the prediction of the AgNP oxidation behaviour in presence of different DNA ligands and varying ligand concentrations. This might be also useful for other biomolecular ligand classes such as aptamers or antibodies.

## 6 Detection of DNA hybridization

DNA hybridization is a very specific molecular recognition process and one of the most fundamental processes in biology. Thus, being able to detect DNA hybridization and associated processes is a key step for a variety of applications such as gene analysis, DNA diagnostics or disease detection. DNA biosensors represent a promising analytical tool and extensive research is performed in the field. The underlying principle is based on recognition of a DNA target sequence by its complementary counter part, which is immobilized onto a surface [244, 245]. Stochastic nanoparticle impact electrochemistry has also been employed to investigate hybridization processes. In this approach, the probe DNA is usually immobilized onto the nanoparticle and hybridization is performed in solution on the nanoparticle. The introduction of the DNA provides specificity for the target DNA and the nanoparticle serves as redox label. This enables the transformation of an otherwise redox inactive target into an electrochemically detectable analyte. For stochastic nanoparticle impact based detection using DNA-functionalized nanoparticles, previous research mostly focused on electrocatalytic impacts [21, 190, 191] and to date only one study on direct Faradaic impacts exists [22]. Important aspects are verification of hybridization itself and in a next step on the nanoparticles. In this chapter, a detailed analysis of DNA hybridization in solution and on the AgNP-conjugates is given, followed by probing stochastic nanoparticle impact electrochemistry for the detection of DNA hybridization.

### 6.1 Experimental evaluation and predictions of single stranded DNA structure

DNA hybridization depends on different external parameters such as temperature and buffer composition but also on the initial conformation of the single stranded DNA. Especially, secondary structural motifs such as stem-loops have been identified to influence the hybridization mechanism and slow down the overall process [85–87]. A secondary structure forms if two or more complementary parts exist within the sequence of a single strand. In an attempt to identify self-complementary strand parts and possible secondary structures, folding predictions based on the Mfold web server were performed for a temperature of 25°C and a concentration of 50 mM NaCl [147]. A summary of the results is listed in Table 6.1. The software gives the

**Table 6.1:** Summary of DNA folding predictions based on the Mfold web server [147].  
T = 25°C, c<sub>NaCl</sub> = 50 mM.

Name	Number of structures	Predicted stable structures	$\delta G$ [kcal/mol]	$T_m$ [°C]
10mer	2	-	2.4-3.4	<0
13mer	2	-	2-3	<0
17mer	1	1	-1.3	43
20mer	2	-	0.7-1.7	<2
26mer	18	-	2-3	<0
17mer cDNA	5	1	-0.1	27
26mer cDNA	13	-	2.7-3.4	<0
30mer cDNA	3	1	-0.1	27

thermodynamic data of possible structures after folding including the change in free energy  $\delta G$  and the melting temperature  $T_m$ . From the data it can be clearly seen, that only the 17mer and its two complementary strands (17mer cDNA = fully complementary, 30mer cDNA = fully complementary +13 bases overhang) can fold spontaneously into a secondary structure. In all three cases the strand folds into a stem-loop with an associated negative change in free energy. The predicted melting temperatures can give additional information on the duplex stability for the given experimental parameters. With a melting temperature of 43°C the stem-loop formed by the 17mer strand should be stable during experiments performed at room temperature. The predicted structure is depicted in Appendix Figure 8.14 with the formed base pairs in red. The stem is closed by a CC/GG duplex and the loop contains four bases. The stability of such a structure might be surprising, due to the short stem and small loop size. However, certain tri- and tetraloop sequences exhibit a notable stability and can occur randomly in probes, targets and primers with a significant probability. Importantly, they can strongly impede hybridization [246]. For identical stem length, smaller loops are more stable than larger ones with hydrophobic interactions of the bases within the loop and the exclusion of water as possible reason for the increased stability [247]. Experimentally, the formation of stable mini-hairpin structures with two GC pairs have been reported. The overall loop stability increases for a CG closing pair and extraordinary stabilities were found with a GC/CG duplex. Structures closing with a CC/GG duplex, showed lower stabilities but with a melting temperature of 65°C (DNA) and  $\approx 40^\circ\text{C}$  (RNA) hairpin formation was still observed [248–252]. Therefore, formation of the predicted stem-loop containing also a CC/GG duplex is reasonable. The predicted melting temperatures of 27°C for the two complementary strands are very close to room temperature and thus, it is likely that they exist in their unfolded form or as a mixture. For all other DNA strands the change in free energy for folding is positive and the calculated melting temperatures are below 0°C. Therefore, those structures should not be present for the given experimental parameters. According to the predictions, hybridization of the 26mer with its complementary strand should work as

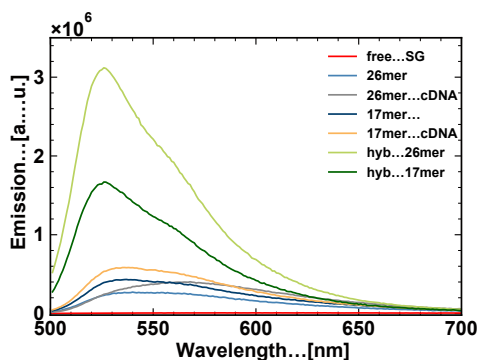


**Figure 6.1:** Fluorescence emission spectra for free SG (red), 26mer (light blue), 26mer cDNA (grey), 17mer (blue), 17mer cDNA (orange), hybridization of 26mer + 26mer cDNA (green) and hybridization of 17mer and 17mer cDNA (darkgreen), excitation = 485 nm,  $c_{\text{DNA}} = 2000 \text{ nM}$ . Hybridization samples are diluted 1:4 with buffer.

expected, whereas the assay for 17mer could be influenced by a secondary structure.

In order to evaluate possible secondary structures and verify the hybridization of the selected probe and target strands, a fluorescence assay based on SYBR Green I (SG) was used. SG is a cyanine dye, which preferentially binds to dsDNA. This binding is accompanied by a strong enhancement in fluorescence intensity [152, 253]. It has been reported that the dye also interacts with ssDNA, but the fluorescence is much lower. Additionally, the emission band when complexed with ssDNA is broader and the maximum shifts towards higher wavelengths [152, 254]. Therefore, evaluation of DNA structure and hybridization is possible via monitoring the fluorescence intensity. In a first step, fluorescence emission spectra of free SG, the individual DNA probe (17mer, 26mer) and target (17mer cDNA, 26mer cDNA) strands as well as for the hybridized samples were recorded. Emission data for excitation at 485 nm are depicted in Figure 6.1. The fluorescence intensity is the lowest for the free dye. For complexation with ssDNA the intensities increase. Two groups of ssDNA can be identified. The 17mer group exhibits a maximum around 535 nm. The spectra of the 26mer group is shifted towards higher wavelengths with a maximum around 565 nm (26mer cDNA). The spectrum for 26mer has the lowest intensity with a large plateau and no clear maximum. The fluorescence intensities for both hybridized samples increase strongly considering that they are diluted four times and have a maximum at 525 nm. This value matches well with the reported maximum at 524 nm. This, together with the strongly increased intensity confirms that both samples hybridized and are present in their duplex form. A shift towards higher wavelengths has been reported for interaction of SG with ssDNA and the maximum ranged between 535 and 550 nm, matching well with the experimental observations. The shift depends on the ratio of dye/base and increases with increasing ratios. In all experiments the amount of dye and DNA concentration were constant. Accordingly, the 26mer has a lower dye/base ratio

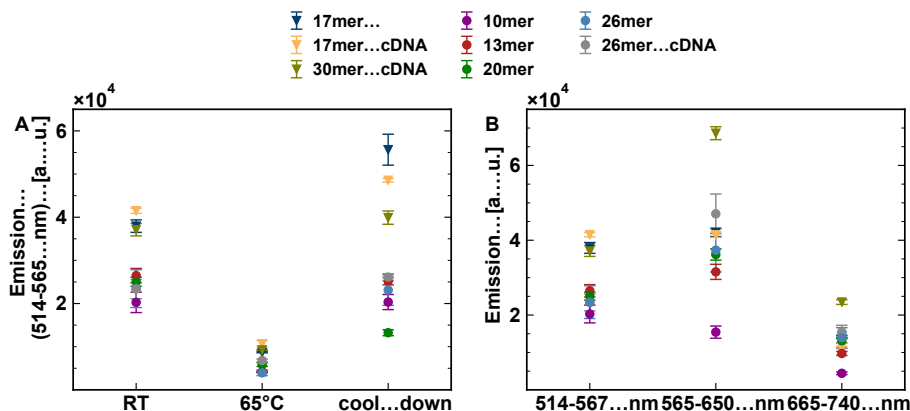


**Figure 6.2:** A) Fluorescence emission for different ssDNA (circle) and with possible secondary structure (triangle). Measured in range 1 (514-567 nm) at RT, 65°C and after cooling down to RT again. B) Fluorescence emission for different ssDNA (circle) and with possible secondary structure (triangle) recorded in range 1 (514-567 nm), range 2 (565-650 nm) and range 3 (665-740 nm),  $c_{DNA} = 2000$  nM.

and should be shifted less [152,253]. However, the opposite is the case and the question arises if the reason could be the predicted secondary structure for 17mer.

Overall, the spectra prove that the hybridization of complementary strands works and can be monitored using SG. Additionally, the intensities for ssDNA are much lower, which allows to discriminate between ssDNA and dsDNA. Before starting with the hybridization detection, fluorescence experiments for all ssDNA strands reported previously were performed. In PCR and most hybridization protocols the samples are heated above the melting temperature in order to break all hydrogen bonds and thus also secondary structures. Upon a slow cooling process, the duplex hybridization is facilitated [81,253]. All fluorescence intensities reported here were therefore measured at room temperature (RT), at 65°C and after cooling down. The intensities after the cooling process are expected to be in the range of the ones for room temperature measurements or even higher if hybridization is facilitated. As explained in subsection 3.4.1, the used fluorometer does not give an emission spectrum but the relative intensities for three different wavelength ranges (range 1 (514-567 nm), range 2 (565-650 nm) and range 3 (665-740 nm)). In presence of double stranded DNA, high intensities in range 1 should be observed. For ssDNA the values in range 1 should be lower and increased intensities in range 2 should be present. In range 3, the intensities should be the lowest since the spectra show only negligible emission above 650 nm. Figure 6.2A gives the emission intensities for all eight ssDNA strands in range 1 measured at RT, 65°C and after cooling down. The fluorescence intensities at RT in range 1 can be divided into two groups. The 17mer and its complementary strands show higher intensities, whereas all other strands exhibit lower intensities. Upon heating to 65°C the intensities for all strands decrease strongly.

After cooling down, the values of 17mer and 17mer cDNA increase compared to RT. For all other strands the intensities are in the range for RT. The higher values for the 17mer group at RT correspond to the observations from the spectra, with a maximum at 535 nm resulting in higher intensities in range 1. The drop for heating the samples is caused by a quenching effect of SG together with complex dissociation for higher temperatures and is independent of the sequence [255,256]. The higher intensities for 17mer and 17mer cDNA after cooling down could be caused by the presence of a duplex part, which hybridizes more efficiently after heat treatment. For the other strands a heat treatment does not induce any structural changes and the values are almost the same before and after heating. The results for the 30mer strand are difficult to interpret, since it is the longest strand and the contributions from the longer single stranded part might be higher than from the short duplex sequence. In Figure 6.2B the intensities for the three different ranges at RT are compared. In range 1 again the two subgroups are displayed. In range 2 the intensities for 17mer and 17mer cDNA stay the same as in range 1. For all other strands the intensities in range 2 are higher than in range 1. Range 3 shows the lowest intensities and can be neglected. The almost identical values in range 1 and 2 for 17mer and 17mer cDNA could be attributed to contributions from a duplex part (range 1) and a single stranded part (range 2). For the other strands the higher intensities in range 2 most likely correspond to a strong contribution of a single stranded sequence part. The wavelength range matches well with the observed maximum in the spectrum for ssDNA around 565 nm.

The experimental results illustrate a different behaviour of the 17mer and the 17mer cDNA. For all experiments the fluorescence intensities in range 1 corresponding to SG/dsDNA interactions, are higher than for all other strands. Additionally, a heat treatment typically used for hybridization assays, results in higher fluorescence intensities. Taking into account the secondary structure predictions, it is justified to attribute the observed behaviour to the formation of a secondary structure involving a duplex part. The predicted stem-loop is reasonable and supposed to be the structural motif present in the 17mer and 17mer cDNA. However, the experimental results don't allow inference of the exact structure and further experiments would be required for giving a definite conclusion.

## 6.2 DNA hybridization in solution

The results reported in the previous section validate that the SG based fluorescence assay is suitable to monitor a transition from ssDNA to dsDNA based on an increase in fluorescence intensity. This method was then employed to investigate DNA hybridization of the selected strands in solution. Such a step is necessary to verify that the hybridization works for the chosen experimental parameters. An important factor is for example the solution composition. Typically, magnesium ions are added to the buffer to facilitate hybridization.

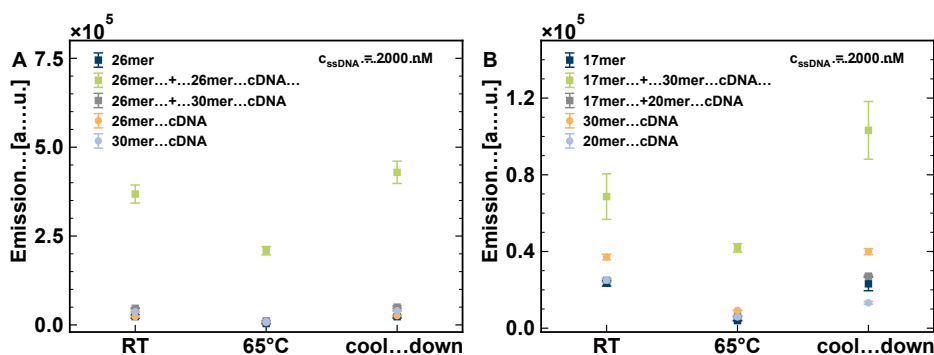


**Figure 6.3:** A) Fluorescence emission for hybridization of 26mer with its complementary 26mer cDNA strand (green). Controls: 26mer (blue), 26mer + 30mer non-complementary DNA (grey), 26mer cDNA (orange), 30mer cDNA (non-complementary) (light blue), B) Fluorescence emission for hybridization of 17mer with its complementary 30mer cDNA strand (green). Controls: 17mer (blue), 17mer + 20mer non-complementary DNA (grey), 30mer cDNA (orange), 20mer cDNA (non-complementary) (light blue),  $c_{ssDNA} = 2000$  nM, measured in PBS (50 mM NaCl).

However, already low amounts of added magnesium result in AgNP aggregation, even for DNA-protected samples as shown in Appendix Figure 8.15 (critical coagulation concentration:  $\approx 3$  mM [150]). Ideally, hybridization should work in the nanoparticle storage buffer without addition of any other compounds. The results of the fluorescence assay for hybridization of 26mer and 17mer with their complementary strands are presented in Figure 6.3. The experiments were performed in particle-free PBS (50 mM NaCl) and the total concentration of ssDNA was 2000 nM. In order to exclude that the measured increase in intensity is caused by interaction of SG with ssDNA and changing DNA concentrations, control experiments were conducted. The fluorescence intensities for the relevant ssDNA strands as well as for incubation with a non-complementary strand are displayed together with the hybridization sample of interest. For both data sets, the hybridization sample (green) shows the highest fluorescence intensity with an increase after heating and cooling. The intensities for ssDNA and in presence of a non-complementary strand (grey) show a  $\approx 10$  fold decrease for the 26mer set, which is in accordance to literature results [152]. This confirms that the increase in fluorescence intensity can be attributed to duplex formation. Importantly, incubation with a non-complementary strand does not give any increase in fluorescence intensity, which is crucial to ensure target specificity. The decrease in intensity for 17mer is only  $\approx 2$  fold. This, together with the much lower fluorescence intensities for hybridization when compared to the 26mer could indicate a lower hybridization efficiency. Reason for this could be the stem-loop secondary structure, which was reported to effect the hybridization kinetics. Overall, the chances for base pairing are decreased and the hybridization process becomes more complex. The presence of a secondary structure imposes a thermodynamic and kinetic barrier to hybridization and the reaction rates are strongly decelerated. Higher temperatures during

hybridization can reduce this effect and the process becomes structure-independent, which could partly explain the increase in intensity after heating and cooling. Additionally, the stability of the resulting duplex is lower and in case of a secondary structure in both, probe and target, the overall affinity is decreased [85–87, 257]. Considering that the probe strand (17mer) and its complementary target both can exhibit a secondary structure, the described effects are likely to be the reason for a lower hybridization efficiency.

All together the results demonstrate that hybridization of 26mer with its complementary strand works well in the storage buffer and could serve as model system for further investigations on DNA hybridization. In case of the 17mer a secondary structure present in the sequence renders hybridization more complicated and the 17mer detection system is not well-suited as model system but should rather be treated as special case.

### 6.3 DNA hybridization on nanoparticles

After confirming that hybridization is possible in the nanoparticle storage buffer, experiments with DNA-AgNP conjugates were conducted. The crucial change here is the immobilization of the probe strand on the nanoparticle surface. In general, DNA hybridization at the solid-liquid interface is more complicated in comparison to the process for free DNA in solution, due to a variety of different factors. Parameters such as surface charge [258], surface strand density [259] or probe length [260] induce a heterogeneity at the surface, which affects the kinetics and stability of DNA hybridization [112]. Electrostatic repulsion between target DNA and the immobilized probe was found to be an important factor. As mentioned previously, the negatively charged DNA on the nanoparticle surface imposes an electrostatic barrier for the attachment of additional strands during nanoparticle modification. This is also true for DNA hybridization. The barrier increases with every hybridization event, due to the constant accumulation of charge and hybridization becomes more difficult with proceeding of the process. However, hybridization at a certain site can change the conformation of a single strand at a distal site, increasing the binding affinity of this strand [113, 261]. Additionally, a high probe density and non-specific adsorption of parts of the probe strand induce steric hindrance and reduce the probe accessibility for target binding. This effect is more pronounced for the bases close to the nanoparticle surface and decreases with increasing distance due to curvature effects. Therefore, a low probe density is more favourable [86, 106, 107, 259]. A proposed reaction pathway at low surface coverages consists of non-specific adsorption of the target ssDNA on the nanoparticle surface, diffusion on the surface until meeting with a probe strand followed by hybridization. The rate-limiting step is the hybridization reaction [112]. Taking into account the increased hybridization efficiency for lower surface coverages together with AgNP-oxidation being only possible at lower surface loadings, the hybridization experiments were only performed for DNA-AgNP conjugates prepared at low initial NP:DNA ratios.



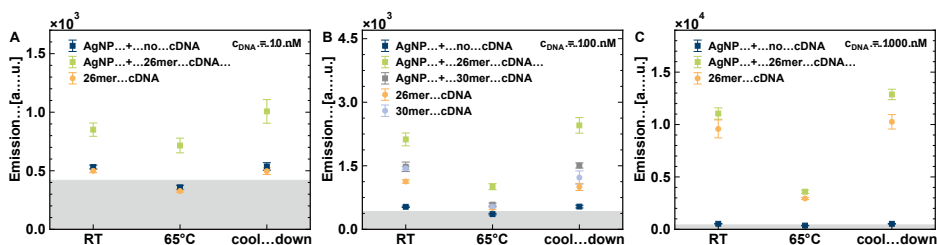


**Figure 6.4:** Fluorescence emission for hybridization of 26mer-capped AgNPs (ratio 1:50) ( $c_{\text{AgNP}} = 1000 \text{ pM}$ ) with its complementary 26mer cDNA strand (green) for A) 10 nM, B) 100 nM and C) 1000 nM target DNA concentration. Controls: 26mer-capped AgNPs (blue), 26mer-capped AgNPs + non-complementary DNA (grey), 26mer cDNA (orange), 30mer cDNA (non-complementary) (light blue). The grey area gives the background fluorescence from free SG.

The ratios of nanoparticles to DNA were 1:50 for 26mer-capped AgNPs and 1:100 in case of 17mer-capped AgNPs. The results for hybridization of 26mer immobilized on 10 nm AgNPs in presence of different concentrations of target DNA are illustrated in Figure 6.4. Control experiments were performed for only the DNA-AgNP conjugates, complementary ssDNA and for incubation with a non-complementary ssDNA strand. The grey area indicates the background fluorescence from free SG. For 10 and 100 nM target concentrations the hybridization sample (green) shows the highest fluorescence intensity with an increase after heating and cooling. All control samples exhibit lower intensities than the hybridization samples, but the difference is much lower when compared to experiments in solution. Again, no unspecific interaction with non-complementary strands can be observed. In presence of the highest target concentration, the intensity of hybridization and ssDNA sample are almost the same at RT and only differ after heat treatment and cooling down. Overall, the fluorescence intensity of the DNA-AgNP conjugates itself is low. Assuming approximately 25 strands/NP for a ratio of 1:50 and a concentration of 1000 pM AgNPs, the total probe DNA concentration is around 25 nM. This value is in the range of the investigated concentration of 10 nM and also the fluorescence intensity of the DNA-capped AgNPs coincides with the experimentally observed fluorescence intensities for 10 nM 26mer cDNA. The increased fluorescence intensity upon incubation of the DNA-AgNP conjugates with the probe strand in comparison to the control samples suggest that hybridization on the nanoparticles takes place. However, the intensities for hybridization are rather low. A combination of two factors could be the reason for this observation. First of all, the DNA probe and target concentration are low and thus, the intensity values that could be expected for duplex DNA are low as well. Secondly, the hybridization efficiency on surfaces was reported to be only about 15-25% in comparison to almost 100% in solution [86, 113]. The main reasons for this behaviour are electrostatic repulsion between probe and target strands as well as surface heterogeneities [112, 261]. As a consequence, the concentration of hybridized DNA is lower than the concentration of available target DNA and most likely close to the detection limit. Another factor could be, that DNA hybridization

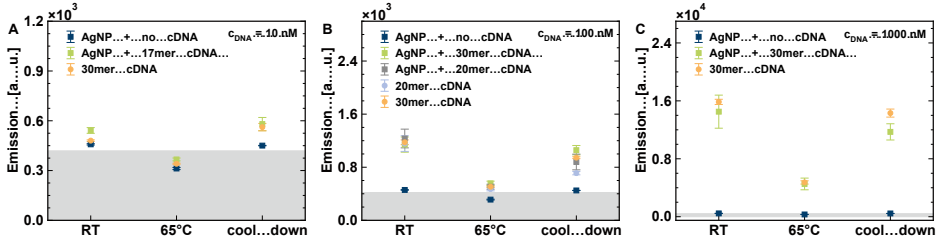


**Figure 6.5:** Fluorescence emission for hybridization of 17mer-capped AgNPs (ratio 1:100) ( $C_{\text{AgNP}} = 1000 \text{ pM}$ ) with its complementary 30mer cDNA strand (green) for A) 10 nM, B) 100 nM and C) 1000 nM target DNA concentration. Controls: 17mer-capped AgNPs (blue), 17mer-capped AgNPs + non-complementary DNA (grey), 30mer cDNA (orange). The grey area gives the background fluorescence from free SG.

does not reach completion within the time frame of the experiment, due to a slower process compared to in solution [113]. Furthermore, the fluorescence intensity resulting from the low amounts of duplex DNA can be easily masked by the presence of larger amounts of ssDNA, which is the case for a target concentration of 1000 nM.

The results for the 17mer strand hybridization set are depicted in Figure 6.5. Here, again the fluorescence intensities for the DNA-AgNP conjugates are the lowest. For the control and hybridization samples, the values are almost the same and don't show any change with temperature. This is the case for all three target concentrations. Overall, these findings suggest that hybridization does not work, or that the increase in fluorescence is completely masked by the presence of ssDNA. Considering the stem-loop configuration and the already low intensities for the 26mer set, this finding seems reasonable. The presence of a secondary structure similarly inhibits hybridization in solution and on surfaces. Experimentally, lower hybridization rates for hairpins were found, indicating the persistence of the secondary structure on the nanoparticle surface. Additionally, the hybridization process for hairpin structures can take hours until completion [86, 112]. Thus, the efficiency should be even lower than for the 26mer, which corresponds to the experimental observations.

To sum up, the outcomes of this section illustrate that DNA hybridization for the 26mer and its complementary strand can also be observed on the surface of nanoparticles. However, the efficiency was found to be much lower in comparison to solution-phase hybridization, which has to be taken into account for any further application. For the 17mer it was not possible to detect hybridization on the nanoparticle surface. The 26mer set represents a suitable model system for the development of a nanoparticle impact based scheme for the detection of DNA hybridization. Additionally, it would be also possible to develop a fluorescence based detection scheme. For both strategies, an optimization of the hybridization efficiency would be beneficial.

## 6.4 Impact based detection of DNA hybridization

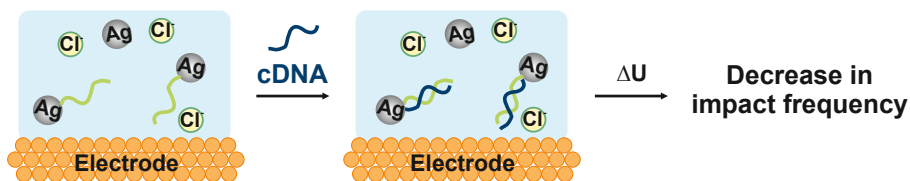


**Figure 6.6:** Scheme of the nano-impact based detection of DNA hybridization on silver nanoparticles relying on a reduction in impact frequency upon target hybridization.

The literature reports for DNA detection based on stochastic nanoparticle impact electrochemistry are scarce and mostly focusing on electrocatalytic impacts with platinum nanoparticles [20,21,191,262]. With silver nanoparticles an aptamer-based detection scheme has been reported based on monitoring AgNP collisions for aggregation/disaggregation in presence of the target [22]. The detection scheme employed in this thesis relies on a modulation of the AgNP redox activity upon probe-target hybridization and is depicted in Figure 6.6. As demonstrated in section 5.5, a slight increase in DNA surface coverage can strongly impede oxidation of silver nanoparticles. Accordingly, DNA hybridization is expected to increase the surface loading by increasing the spatial requirement for a single DNA unit. This process should induce a decrease in redox activity, which could be monitored as a change in AgNP impact frequency.

Each measurement set consisted of a reference measurement of only DNA-AgNP conjugates without addition of any target DNA (blank), the hybridization sample with complementary DNA (hybridization) and a control sample with non-complementary DNA (control). All samples were incubated under identical conditions. This design allows for direct identification of possible changes induced by DNA hybridization via comparison of the impact frequencies within a measurement set. The detection was performed for hybridization of 26mer and 17mer with their respective complementary strands. The 30mer strand complementary to 17mer exhibits a 13 base long overhang intended to increase the thickness of the DNA shell upon hybridization. In total, three different target concentrations were tested. The results for impact based detection of DNA hybridization are illustrated in Figure 6.7. For both target systems and all three concentrations no meaningful differences or a clear trend can be observed. In general, the impact frequencies show some variations but are in the same range within the measurement set for a single as well as for different target concentrations. In case of blank and control measurements, this behaviour indicates reproducibility and the absence of any non-specific interactions. Both are requirements for development of a reliable sensor scheme. However, the hybridization measurements are also in the same range with blank and control and don't show any dependence on target concentration. This is the case for both

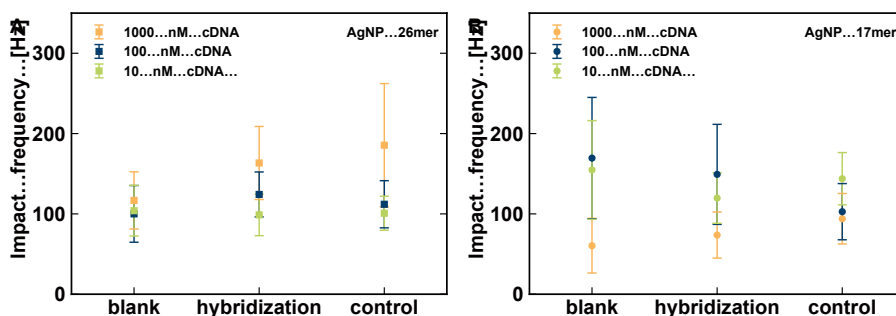


**Figure 6.7:** Mean impact frequency per chip for detection of DNA hybridization for A) 17mer-capped AgNP, B) 26mer-capped AgNPs. Blank: DNA-capped AgNPs, hybridization: + complementary DNA, control: + non-complementary DNA,  $c_{\text{AgNP}} = 23 \text{ pM}$ , potential = 0.4 V vs. Ag/AgCl, electrolyte = PBS (200 mM NaCl).

systems under investigation and could have different reasons. First of all, the previously elucidated drawbacks for DNA hybridization on nanoparticles such as low hybridization efficiencies and slow kinetics apply also to the impact based approach. Therefore, only a small fraction of the probe strands attached to the nanoparticles are expected to hybridize. If we consider a surface loading of 25 strands/NP and a hybridization efficiency of 25% on average only six strands would hybridize. The resulting conformational change of the DNA shell might not be sufficient to alter the nanoparticle oxidation properties in a way that a difference can be measured. Also the approach based on a complementary strand with a large overhang did not induce a measurable change in impact frequency. This seems reasonable considering that the amount of hybridized strands is expected to be even less in the presence of a secondary structure for the 17mer.

The results demonstrate that it was not possible to monitor DNA hybridization for the given experimental parameters. In general, the process of DNA hybridization on nanoparticles is more complex than expected and a variety of different parameters have to be considered.

## 6.5 Summary

In this section, a method to monitor DNA hybridization based on SYBR Green I as dye has been presented. The method relies on a strong interaction of the dye with double stranded DNA resulting in enhancement of the fluorescence. The reported fluorescence emission spectra confirm this effect. Additionally, interaction with single stranded DNA is observed, but with much lower intensities. The characteristics of the spectra are in good accordance with literature findings and reveal differences for intercalation with either dsDNA or ssDNA. This

allows estimation of possible intrastrand secondary structures. Thermodynamic predictions of DNA secondary structure foldings indicate the presence of a stem-loop motif in the 17mer and its complementary strands. At first glance the predicted structure seems rather unstable. However, comparable sequences were found to exhibit extraordinary thermodynamic stability. Comparison of the fluorescence behaviour of all ssDNA strands reported in this section give additional experimental evidence for the presence of a double stranded part. Altogether, the existence of the predicted stem-loop is reasonable and accepted as primary structural motif in this group of DNA strands. However, further experiments are required to give a final conclusion.

Hybridization of the selected strands in solution could be verified by the SG based fluorescence assay. The nanoparticle storage buffer was identified as suitable hybridization medium. An additional separation and transfer of the nanoparticles to another medium as well as addition of hybridization promoting compounds is not necessary. This is important to keep the system as simple as possible. Whereas hybridization in solution is straight-forward the process on surfaces becomes more complex with decreased hybridization efficiencies and impaired kinetics. This is partly reflected in the observations for hybridization on the nanoparticle surface. Hybridization works to a certain extent but the fluorescence intensities are lower than for hybridization in solution. For stochastic nanoparticle impact electrochemistry it is not possible to identify measurable differences or a trend for different concentrations for the given experimental parameters. Overall, this can have several reasons. The total amount of probe DNA available for hybridization is low, due to the low DNA surface loading on the nanoparticles. Together with efficiencies of only around 15-25%, the expected amount of hybridization events is also low and not sufficient to induce a change in oxidation behaviour. The most apparent solution to this problem could be an increase in DNA surface loading. For the fluorescence based assay increasing the DNA surface loading is suitable, whereas not for impact based detection. As reported in chapter 5 the redox activity of the AgNPs is very sensitive towards DNA conjugation. The DNA loading window for detectable oxidation signals is rather narrow and high loadings result in complete particle redox-inactivation. Therefore, the DNA loading on the nanoparticle surface has to be kept low in order to maintain redox activity. A suitable approach could be based on using DNA with a hairpin motif as detection probe. DNA-AgNP conjugates with structured DNA were found to follow a remarkably different oxidation behaviour. The DNA concentration window in which particles can be detected is wider allowing for higher DNA surface loadings. This together with an increased target specificity of structured probe strands [263] could be advantageous for the development of nanoparticle impact based DNA sensors. Special attention has to be paid to the design of the complementary strand in order to avoid secondary structural motifs, which could have adverse effects on hybridization.

## 7 Summary and Outlook

The aim of this thesis was the modification of silver nanoparticles with thiolated single stranded DNA and the employment of the as-prepared nanoparticles for stochastic nanoparticle impact electrochemistry. This impact based strategy should be probed for the detection of DNA hybridization on the nanoparticle surface.

An optimized modification protocol gave access to stable AgNP-DNA conjugates with different DNA length. Additionally, the protocol provided good control over the DNA density on the nanoparticle surface by varying the initial DNA concentration during modification. A detailed nanoparticle characterization gave insight into their physicochemical properties and it was possible to relate DNA length and initial concentration to specific nanoparticle properties. This allows for precise tuning of the nanoparticle properties according to the individual needs and requirements for a specific type of experiment. In the future, it could be interesting to adapt the protocol to different nanoparticle sizes. Larger nanoparticle sizes could give access to additional characterization methods such as nanoparticle tracking analysis (NTA). This method represents a suitable characterization strategy especially for polydisperse samples but features a lower critical particle size of 30 nm [264]. Furthermore, the impact of the final salt concentration during the modification could be investigated. The concentration influences the DNA density on the nanoparticle surface and could be a useful feature for precision tuning of the DNA loading.

A combination of low-noise microelectrode arrays with an ultrasensitive amplifier system was employed for the amperometric detection of silver nanoparticle oxidation. For this detection method a linear relationship between nanoparticle concentration and impact frequency was found. This enables nanoparticle quantification, which is an essential feature for development of a sensor scheme. A comparison between citrate and DNA-stabilized AgNPs revealed a significantly different oxidation behaviour. Overall, the impact frequency for DNA-stabilized nanoparticles is reduced in comparison to citrate-capped AgNPs. However, the surface modification with DNA induces a higher nanoparticle stability in presence of elevated salt concentrations, resulting in an increased impact frequency. This is of ample relevance for measurements in biological media. By variation of the measurement conditions, i. e. the electrolyte concentration and the applied potential, it was possible to identify critical parameters that play an important role for oxidation of DNA-capped nanoparticles. It could be demonstrated that a higher overpotential and elevated salt concentrations are required for reliable detection of

AgNP-DNA conjugates. Optimizing those parameters allowed for maximization of the impact frequency. This is crucial for detection of DNA-capped AgNPs in order to counterbalance their reduced oxidation activity. The reported findings facilitate the individual adjustment of the measurement parameters with respect to the species under investigation and could also be of interest for other ligand classes such as antibodies.

For measurements of AgNP-DNA conjugates with different DNA loadings, a trend of decreasing impact frequency with increasing DNA concentration was found. The dominating reason for this behaviour was identified as a change in DNA conformation on the NP surface with increasing surface loading. This conformation change modulates the probability for charge transfer, which undergoes a transition from distance-independent to distance-dependent with increasing DNA density. Overall, the impact frequency decreased already for low DNA loadings. The DNA length only has minor influence on the oxidation process. Interestingly, DNA with a stem-loop motif showed a remarkably different oxidation behaviour. The decrease in impact frequency was less pronounced and good oxidation activity could be maintained over a wide range of DNA densities. In order to acquire a deeper understanding of this phenomenon, experiments with different stem-loop structures are required. A suitable approach could be an experiment series similar to the one performed here, which investigates DNA stem-loops with different stem length and loop sizes. Evidence for the presence of a stem-loop motif was obtained by folding predictions and fluorescence spectroscopy. In the future, this observation could be complemented by circular dichroism spectroscopy, which is frequently used for identification of different DNA conformations [265].

Hybridization of the probe and target strands selected for the hybridization detection scheme could be verified in solution and on the silver nanoparticle surface. However, a low hybridization efficiency was found for experiments on the nanoparticle surface. Initial tests for impact based detection of hybridization events showed no change in impact frequency. The observations revealed a much more complex process on surfaces in comparison to solution phase hybridization due to steric and electrostatic constraints. For the development of an impact based detection scheme, the surface hybridization has to be optimized in the future. A possible solution could be the introduction of a spacer sequence between the thiol anchor and the probe part. This relocates the site for hybridization and reduces steric constraints, which are the strongest near the nanoparticle surface. Furthermore, a diluting short DNA strand or organic compound could be co-assembled with the probe DNA to adjust the strand spacing on the surface. Another issue that has to be addressed is the low DNA loading, which is required to maintain a good redox activity. This limits the amount of probe strands available for hybridization and could explain why no change in impact frequency was observable. A suitable strategy to solve this problem could be the use of stem-loop structures as probe strand. Such an approach could benefit from the different oxidation behaviour for silver nanoparticles modified with a stem-loop DNA. Additionally, one could think about a complementary detection scheme with two different types of electrodes. The DNA-capped

---

AgNPs are attached to the first electrode via hybridization with a slightly mismatched strand immobilized onto the electrode. The interaction has to be sufficient for immobilization but weaker than hybridization with the fully complementary target strand. In presence of the target strand hybridization takes place and the nanoparticles are released from the electrode. A second electrode, biased to an oxidizing potential, collects the released nanoparticles, which can be monitored as impacts in the current-time trace.

In summary, this work reports a detailed evaluation of different relevant parameters for employing DNA-capped AgNPs for stochastic nanoparticle impact electrochemistry. Importantly, new insights on the oxidation behaviour in presence of DNA as ligand could be obtained. The relation between DNA density and conformation and the oxidation behaviour is an important aspect for a better understanding of the oxidation process and could help to design more efficient DNA-nanoparticle probes. The optimized measurement parameters could serve as basis for the development and improvement of sensing schemes.





## 8 Appendix

### MEA Fabrication

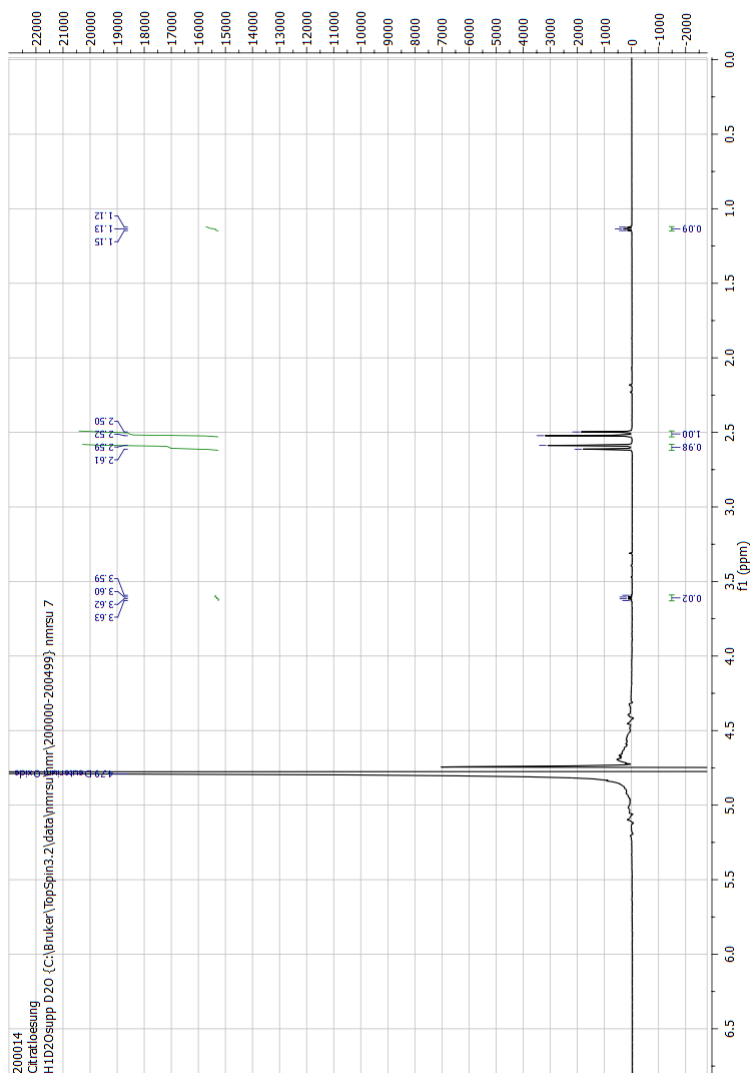
The basis for the production of MEAs is a borosilicate wafer with a diameter of 100 mm and a thickness of 500  $\mu\text{m}$ . This wafer is firstly covered with a two resist layer via spin-coating. The photoresists were LOR 3b (Microchem, Newton, MA) and nLOF 2070 (MicroChemicals, Ulm, Germany) respectively. The 64 electrode and feedline pattern is fabricated via standard photolithography. After patterning the layout the metallic electrodes and feedlines are build up using electron beam deposition. At first, a 10 nm Ti layer is deposited followed by 200 nm of Au and another 10 nm Ti layer. The Ti layers are necessary for adhesion between the metal and the substrate/passivation. Afterwards, a lift-off process is used for removal of the photoresist layers. For insulation of the feedlines a passivation layer is inevitable. The alternating stacks of  $\text{SiO}_2$  and  $\text{Si}_3\text{N}_4$  are produced with plasma enhanced physical vapour deposition. The  $\text{Ta}_2\text{O}_5$  ALD layer is deposited via plasma enhanced atomic layer deposition at 130°C. The regions for electrode openings and bondpads are defined by photolithography with AZ5214 as photoresist and opened with a two step reactive ion etching process. The ALD layer is opened with a mixture of  $\text{CF}_4$ ,  $\text{O}_2$  and Ar, for the ONONO stack  $\text{CHF}_3$  is added. After the wafer has run through all production steps it is diced into nine individual chips.

### Particle modification and characterization

#### NMR of AgNP stock solution

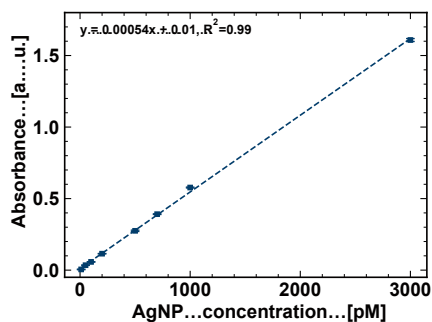
The  $^1\text{H}$ -NMR spectrum shows absorptions around 2.5 ppm corresponding to the enantiotopic  $\text{CH}_2\text{COOH}$  groups of the citrate molecule [266]. Citrate is the major component with some minor impurities of ethanol. The impurities could also be introduced during sample transfer or cleaning of glassware. The peak around 5 ppm corresponds to the solvent  $\text{D}_2\text{O}$ .

**Ethanol (C<sub>2</sub>H<sub>5</sub>OH):** <sup>1</sup>H-NMR (600 MHz, D<sub>2</sub>O) δ [ppm]: 3.83-3.43 (m, 1H), 1.13 (t, J = 7.1 Hz, 1H).

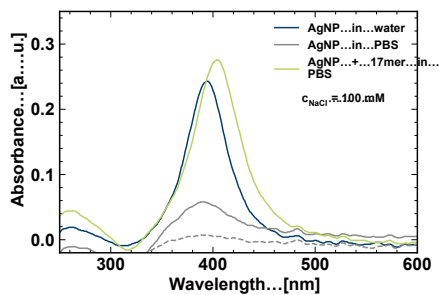


100

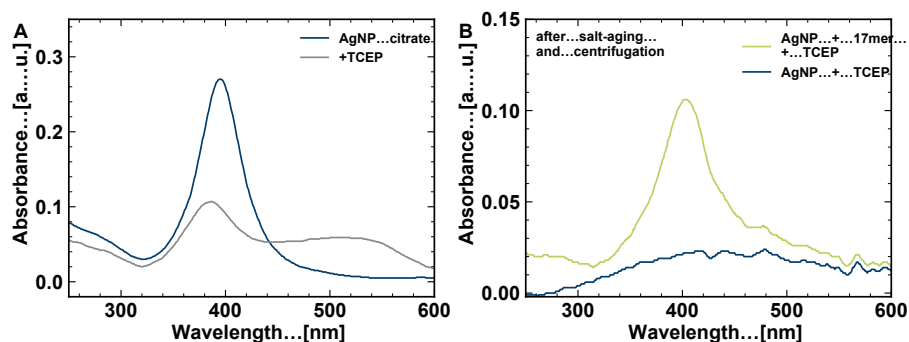
## Physical and chemical properties



**Figure 8.2:** UV-Vis absorption based calibration curve for determination of AgNP concentration after modification. Dashed line = linear fit.



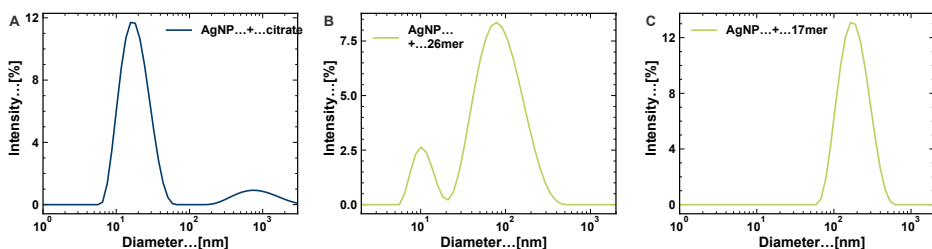
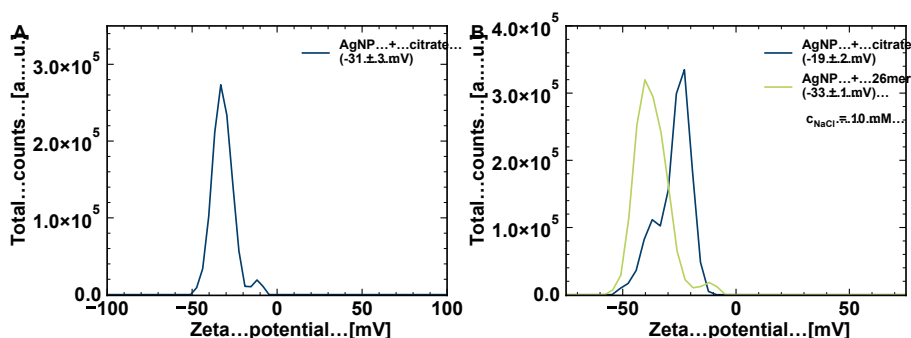
**Figure 8.3:** UV-Vis spectra of citrate-capped AgNPs in water (blue), PBS (grey) and spectra of DNA-capped AgNPs in PBS (green). Solid line:  $t = 0$  min, dashed line:  $t = 10$  min.  $c_{\text{NaCl}} = 100$  mM



**Figure 8.4:** A) UV-Vis spectra of citrate-capped nanoparticles (blue) and after mixing with TCEP (grey). B) UV-Vis spectra of DNA-capped nanoparticles (green) and citrate-capped nanoparticles (blue) after incubation with TCEP, salt-aging and centrifugation.

**Table 8.1:** Summary of detected amounts of phosphorus and silver via inductively coupled plasma mass spectrometry.

Sample	P [mg/kg]	Ag [mg/kg]
AgNP citrate	$0.043 \pm 0.008$	$16.7 \pm 0.4$
DNA-AgNP 1:100-1	$0.102 \pm 0.008$	$15 \pm 3$
DNA-AgNP 1:100-2	$0.13 \pm 0.03$	$6 \pm 3$
DNA-AgNP 1:500-1	$0.204 \pm 0.019$	$10 \pm 11$
DNA-AgNP 1:500-2	$0.157 \pm 0.019$	$9 \pm 10$

**Figure 8.5:** Dynamic light scattering intensity distributions for A) citrate-capped AgNPs, B) 26-mer-capped AgNPs and C) 17mer-capped AgNPs. Diameter according to STEM for all  $\approx 10$  nm.**Figure 8.6:** A) Zeta potential distribution of 10 nm citrate-capped nanoparticles (blue) in water. B) Zeta potential distribution of 10 nm citrate-capped nanoparticles (blue) and DNA-capped nanoparticles (green) measured with 10 mM NaCl as background electrolyte.

## Density of DNA strands on nanoparticles

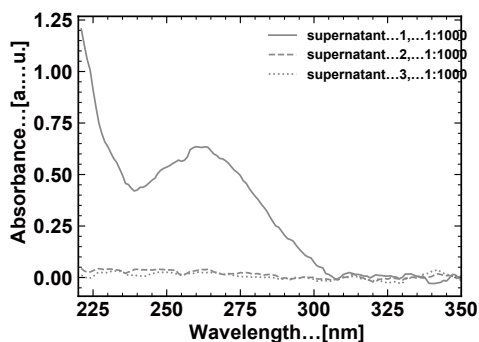


**Figure 8.7:** UV-Vis spectra of centrifugation supernatants for highest DNA concentration (ratio NP:DNA = 1:1000) during modification. No DNA residues detectable after second centrifugation round.

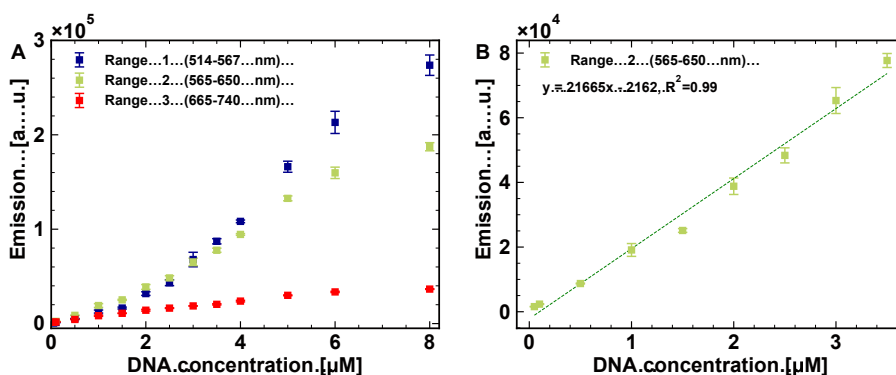


**Figure 8.8:** A) Fluorescence emission vs. 17mer DNA concentration for excitation at  $\approx 470$  nm and the emission recorded in range 1 (514-567 nm, blue), range 2 (565-650 nm, green) and range 3 (665-740 nm, red). B) Fluorescence emission in range 2 for 17mer DNA, dashed line = linear fit.

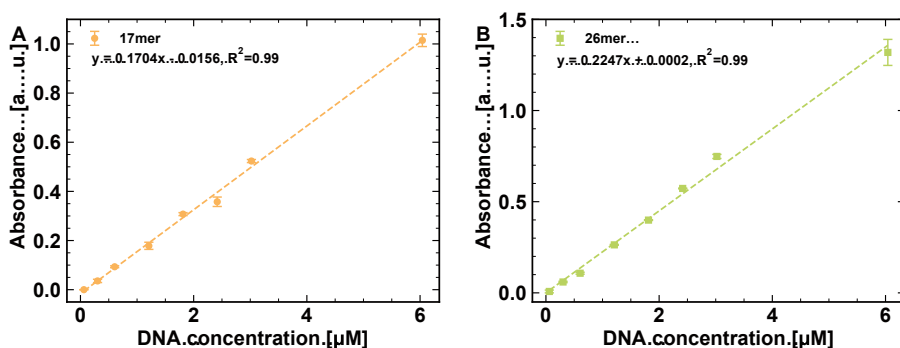
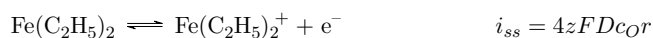


Figure 8.9: A) UV-Vis absorption intensity vs. DNA concentration for A) 17mer and B) 26mer, dashed line = linear fit to data set.

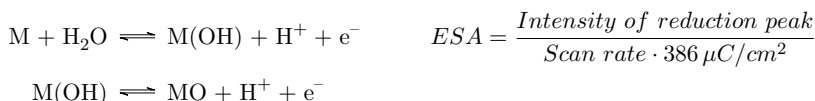
## Stochastic nanoparticle impact electrochemistry

### Characterization of BioMAS measurement device and experimental procedure

Cyclic voltammetry with 1,1'-ferrocene dimethanol,  $\text{Fc}(\text{MeOH})_2$ , as redox probe (A) was used as indicator for electrode performance. A key feature of microelectrodes is the fast establishment of steady-state conditions and the steady-state current (plateau in CV) can be used to calculate the electrochemical surface area [57]. The occurring reaction and the equation are given in the following.



Another way for determining the electrochemical surface area is based on adsorption or desorption of oxygen or hydrogen from acidic solution (here 50 mM  $\text{H}_2\text{SO}_4$ ). During the anodic potential sweep OH species adsorb chemically on the gold surface followed by formation of an oxide layer with a complex stoichiometry as given in the following equations [267,268]. This oxide layer undergoes reduction during the cathodic sweep and the intensity of the reduction peak (derived by integration) can be used to calculate the ESA [142,269]. The average ESA was calculated as  $124 \pm 16 \mu\text{m}^2$  (Fc) and  $123 \pm 20 \mu\text{m}^2$  ( $\text{H}_2\text{SO}_4$ ).



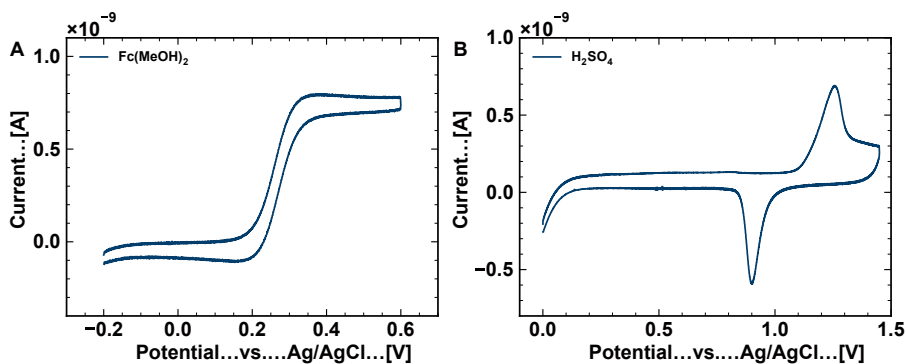


**Figure 8.10:** Exemplary cyclic voltammogram of MEA electrodes recorded in A)  $\text{Fc}(\text{MeOH})_2$  at a scan rate of 100 mV/s and B)  $\text{H}_2\text{SO}_4$  at a scan rate of 50 mV/s.

### Comparison between citrate- and DNA-capped nanoparticles

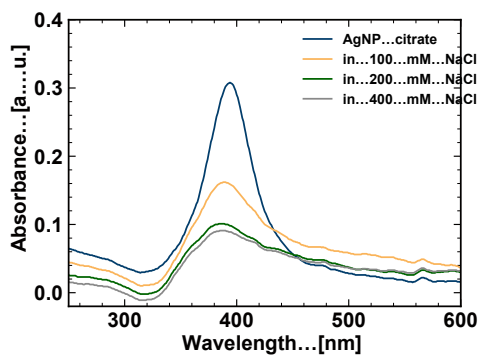


**Figure 8.11:** UV-Vis spectra of citrate-capped AgNPs in different concentrations of NaCl, no NaCl = blue, 100 mM = orange, 200 mM = green, 400 mM = grey.



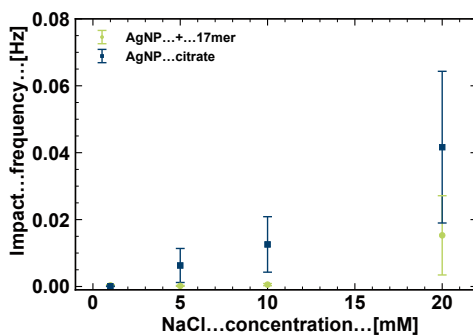


**Figure 8.12:** Impact frequency per chip [Hz] (normalization by maximum number of impacts) for oxidation of citrate- and DNA-capped AgNPs for 1-20 mM NaCl in the electrolyte ( $c_{\text{AgNP}} = 23 \text{ pM}$ , potential = 0.4 V).

### Single stranded DNA with secondary structure

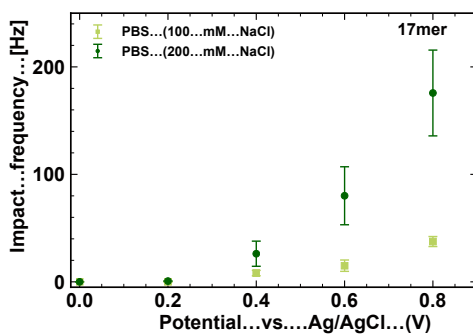


**Figure 8.13:** Impact frequency per chip for 17mer-capped AgNPs (ratio 1:100) in PBS buffer containing 100 mM NaCl (green) and 200 mM NaCl (darkgreen) and different oxidation potentials ( $c_{\text{AgNP}} = 23 \text{ pM}$ )

## Detection of DNA hybridization

### Experimental evaluation and predictions of ssDNA structure

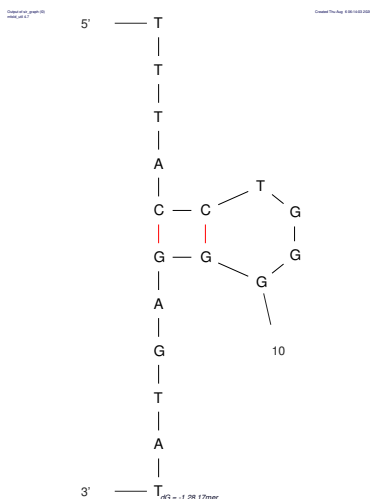


Figure 8.14: Structure of predicted stem-loop folding of 17mer with formed base pairs marked in red.

### DNA hybridization in solution and on nanoparticles

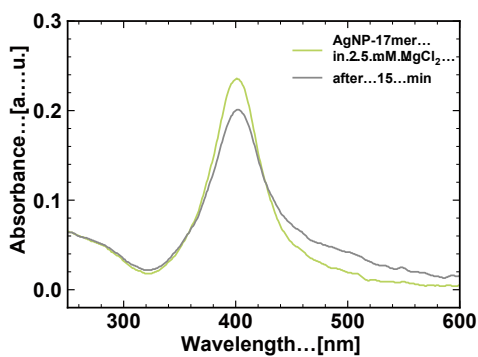


Figure 8.15: UV-Vis spectra of 17mer-capped AgNPs in presence of 2.5 mM MgCl<sub>2</sub>.

## List of abbreviations

<b>AgNP</b>	Silver nanoparticle
<b>DNA</b>	Deoxyribonucleic acid
<b>MEA</b>	Microelectrode array
<b>LOD</b>	Limit of detection
<b>EDL</b>	Electrochemical double layer
<b>IHP</b>	Inner Helmholtz plane
<b>OHP</b>	Outer Helmholtz plane
<b>SHE, NHE</b>	Standard or normal hydrogen electrode
<b>NP</b>	Nanoparticle
<b>SAM</b>	Self-assembled monolayer
<b>LSPR</b>	Localized surface plasmon resonance
<b>RNA</b>	Ribonucleic acid
<b>bp</b>	Base pair
<b>PCR</b>	Polymerase chain reaction
<b>PSB</b>	Polystyrene bead
<b>ECA</b>	Electrocatalytic amplification
<b>ALD</b>	Atomic layer deposition
<b>PDMS</b>	Polydimethylsiloxane
<b>WE</b>	Working electrode
<b>RE</b>	Reference electrode
<b>CE</b>	Counter electrode
<b>CV</b>	Cyclic voltammetry
<b>BioMAS</b>	Bioelectronic multifunctional amplifier system
<b>op amp</b>	Operational amplifier
<b>fbr</b>	Feedback resistor

---

**ADC** Analog-digital-converter

**AC** Alternating current

**rms** Root mean square

**pk2pk** Peak to peak

**NMR** Nuclear magnetic resonance

**PBS** Phosphate buffered saline

**SG** SYBR Green I

**ssDNA** Single stranded DNA

**cDNA** Complementary DNA

**dsDNA** Double stranded DNA

**RFU** Relative fluorescence unit

**RT** Room temperature

**DLS** Dynamic light scattering

**ICPMS** Inductively coupled plasma mass spectrometry

**STEM** Scanning transmission electron microscopy

**std** Standard deviation

**sem** Standard error of the mean

**ESA** Electrochemical surface area

**PSD** Power spectral density

**CT** Charge transfer

**NTA** Nanoparticle tracking analysis



## Bibliography

- [1] J. J. Gooding and K. Gaus, "Single-Molecule Sensors: Challenges and Opportunities for Quantitative Analysis," *Angew. Chemie - Int. Ed.*, vol. 55, no. 38, pp. 11354–11366, 2016.
- [2] S. Goines and J. E. Dick, "Review-Electrochemistry's Potential to Reach the Ultimate Sensitivity in Measurement Science," *J. Electrochem. Soc.*, vol. 167, no. 3, p. 037505, 2020.
- [3] J. H. Zhang and Y. G. Zhou, "Nano-impact electrochemistry: Analysis of single bioentities," *TrAC - Trends Anal. Chem.*, vol. 123, p. 115768, 2020.
- [4] L. A. Baker, "Perspective and Prospectus on Single-Entity Electrochemistry," *J. Am. Chem. Soc.*, vol. 140, no. 46, pp. 15549–15559, 2018.
- [5] Y. Wang, X. Shan, and N. Tao, "Emerging tools for studying single entity electrochemistry," *Faraday Discuss.*, vol. 193, pp. 9–39, 2016.
- [6] S. G. Lemay, S. Kang, K. Mathwig, and P. S. Singh, "Single-molecule electrochemistry: Present status and outlook," *Acc. Chem. Res.*, vol. 46, no. 2, pp. 369–377, 2013.
- [7] M. Neves and D. Martín-Yerga, "Advanced Nanoscale Approaches to Single-(Bio)entity Sensing and Imaging," *Biosensors*, vol. 8, no. 4, p. 100, 2018.
- [8] T. Moazzenzade, J. Huskens, and S. G. Lemay, "Stochastic electrochemistry at ultralow concentrations: The case for digital sensors," *Analyst*, vol. 145, no. 3, pp. 750–758, 2020.
- [9] N. J. Ronkainen, H. B. Halsall, and W. R. Heineman, "Electrochemical biosensors," *Chem. Soc. Rev.*, vol. 39, no. 5, pp. 1747–1763, 2010.
- [10] G. Mabbott, *Electroanalytical Chemistry: Principles, Best Practices, and Case Studies*. John Wiley & Sons, Inc., 2020.
- [11] W. Cheng and R. G. Compton, "Electrochemical detection of nanoparticles by 'nano-impact' methods," *Trends Anal. Chem.*, vol. 58, pp. 79–89, 2014.

- [12] S. V. Sokolov, S. Eloul, E. Kätelhön, C. Batchelor-McAuley, and R. G. Compton, "Electrode-particle impacts: a users guide," *Phys. Chem. Chem. Phys.*, vol. 19, no. 1, pp. 28–43, 2017.
- [13] M. Pumera, "Impact electrochemistry: Measuring individual nanoparticles," *ACS Nano*, vol. 8, no. 8, pp. 7555–7558, 2014.
- [14] D. Andreescu, K. A. Kirk, F. H. Narouei, and S. Andreescu, "Electroanalytic Aspects of Single-Entity Collision Methods for Bioanalytical and Environmental Applications," *ChemElectroChem*, vol. 5, no. 20, pp. 2920–2936, 2018.
- [15] A. López-Serrano, R. M. Olivas, J. S. Landaluze, and C. Cámara, "Nanoparticles: A global vision. Characterization, separation, and quantification methods. Potential environmental and health impact," *Anal. Methods*, vol. 6, no. 1, pp. 38–56, 2014.
- [16] K. Tiede, A. B. Boxall, S. P. Tear, J. Lewis, H. David, and M. Hassellöv, "Detection and characterization of engineered nanoparticles in food and the environment," *Food Addit. Contam.*, vol. 25, no. 7, pp. 795–821, 2008.
- [17] E. J. E. Stuart, N. V. Rees, J. T. Cullen, and R. G. Compton, "Direct electrochemical detection and sizing of silver nanoparticles in seawater media.," *Nanoscale*, vol. 5, no. 1, pp. 174–177, 2013.
- [18] W. Cheng, E. J. Stuart, K. Tschulik, J. T. Cullen, and R. G. Compton, "A disposable sticky electrode for the detection of commercial silver NPs in seawater," *Nanotechnology*, vol. 24, no. 50, 2013.
- [19] X. Li, C. Batchelor-McAuley, and R. G. Compton, "Silver nanoparticle detection in real-world environments via particle impact electrochemistry," *ACS Sensors*, vol. 4, no. 2, pp. 464–470, 2019.
- [20] S. J. Kwon and A. J. Bard, "DNA analysis by application of Pt nanoparticle electrochemical amplification with single label response," *J. Am. Chem. Soc.*, vol. 134, no. 26, pp. 10777–10779, 2012.
- [21] A. D. Castañeda, N. J. Brenes, A. Kondajji, and R. M. Crooks, "Detection of microRNA by Electrocatalytic Amplification: A General Approach for Single-Particle Biosensing," *J. Am. Chem. Soc.*, vol. 139, no. 22, pp. 7657–7664, 2017.
- [22] A. Karimi, A. Hayat, and S. Andreescu, "Biomolecular detection at ssDNA-conjugated nanoparticles by nano-impact electrochemistry," *Biosens. Bioelectron.*, vol. 87, pp. 501–507, 2017.

- 
- [23] P. S. Singh, E. Kätelhön, K. Mathwig, B. Wolfrum, and S. G. Lemay, "Stochasticity in Single-Molecule Nanoelectrochemistry: Origins, Consequences, and Solutions," *ACS Nano*, vol. 6, no. 11, pp. 9662–9671, 2012.
- [24] K. Mathwig, T. J. Aartsma, G. W. Canters, and S. G. Lemay, "Nanoscale Methods for Single-Molecule Electrochemistry," *Annu. Rev. Anal. Chem.*, vol. 7, no. 1, pp. 383–404, 2014.
- [25] Y. T. Long, P. R. Unwin, and L. A. Baker, "Single-Entity Electrochemistry: Fundamentals and Applications," *ChemElectroChem*, vol. 5, no. 20, pp. 2918–2919, 2018.
- [26] Y. Wu, D. Bennett, R. D. Tilley, and J. J. Gooding, "How Nanoparticles Transform Single Molecule Measurements into Quantitative Sensors," *Adv. Mater.*, vol. 32, no. 18, p. 1904339, 2019.
- [27] K. J. Krause, A. Yakushenko, and B. Wolfrum, "Stochastic On-Chip Detection of Subpicomolar Concentrations of Silver Nanoparticles," *Anal. Chem.*, vol. 87, no. 14, pp. 7321–7325, 2015.
- [28] S. Song, L. Wang, J. Li, C. Fan, and J. Zhao, "Aptamer-based biosensors," *TrAC - Trends Anal. Chem.*, vol. 27, no. 2, pp. 108–117, 2008.
- [29] J. Ustarroz, M. Kang, E. Bullions, and P. R. Unwin, "Impact and Oxidation of Single Silver Nanoparticles at Electrode Surfaces: One Shot versus Multiple Events," *Chem. Sci.*, vol. 8, no. 3, pp. 1–13, 2016.
- [30] K. J. Krause, F. Brings, J. Schnitker, E. Kätelhön, P. Rinklin, D. Mayer, R. G. Compton, S. G. Lemay, A. Offenhäusser, and B. Wolfrum, "The Influence of Supporting Ions on the Electrochemical Detection of Individual Silver Nanoparticles: Understanding the Shape and Frequency of Current Transients in Nano-impacts," *Chem. - A Eur. J.*, vol. 23, no. 19, pp. 4638–4643, 2017.
- [31] K. Ngamchuea, R. O. D. Clark, S. V. Sokolov, N. P. Young, C. Batchelor-McAuley, and R. G. Compton, "Single oxidative collision events of silver nanoparticles: understanding the rate-determining chemistry," *Chem. - A Eur. J.*, vol. 23, no. 63, pp. 16085–16096, 2017.
- [32] W. Ma, H. Ma, Z. Y. Yang, and Y. T. Long, "Single Ag Nanoparticle Electro-oxidation: Potential-Dependent Current Traces and Potential-Independent Electron Transfer Kinetic," *J. Phys. Chem. Lett.*, vol. 9, no. 6, pp. 1429–1433, 2018.
- [33] E. E. L. Tanner, S. V. Sokolov, N. P. Young, and R. G. Compton, "DNA capping agent control of electron transfer from silver nanoparticles," *Phys. Chem. Chem. Phys.*, vol. 19, no. 15, pp. 9733–9738, 2017.



- [34] W. Schmickler and E. Santos, *Interfacial electrochemistry*. Springer Science & Business Media, 2010.
- [35] V. S. Bagotsky, *Fundamentals of electrochemistry*, vol. 44. John Wiley & Sons, 2005.
- [36] F. Scholz, *Electroanalytical methods*, vol. 1. Springer, 2010.
- [37] M. Grätzel, “Photoelectrochemical cells,” *Lancet*, vol. 367, no. 9518, pp. 1262–1270, 2001.
- [38] A. J. Bard and L. R. Faulkner, *Electrochemical Methods- Fundamentals and Applications*. John Wiley & Sons, 2001.
- [39] H. Helmholtz, “Studien über electrische Grenzschichten,” *Ann. Phys.*, vol. 243, no. 7, pp. 337–382, 1879.
- [40] M. Gouy, “Sur la constitution de la charge électrique à la surface d’un électrolyte,” *J. Phys. Theor. Appl.*, vol. 9, no. 1, pp. 457–468, 1910.
- [41] D. L. Chapman, “A contribution to the theory of electrocapillarity,” *London, Edinburgh, Dublin Philos. Mag. J. Sci.*, vol. 25, no. 148, pp. 475–481, 1913.
- [42] O. Stern, “Zur Theorie der elektrolytischen Doppelschicht,” *Berichte der Bunsengesellschaft für Phys. Chemie*, vol. 30, no. 21-22, pp. 508–516, 1924.
- [43] D. C. Grahame, “The electrical double layer and the theory of electrocapillarity,” *Chem. Rev.*, vol. 41, no. 3, pp. 441–501, 1947.
- [44] P. M. Biesheuvel and J. E. Dykstra, “The difference between Faradaic and Nonfaradaic processes in Electrochemistry,” *arXiv:1809.02930v1*, pp. 1–10, 2018.
- [45] E. R. Brown, T. G. McCord, D. E. Smith, and D. D. DeFord, “Some Investigations on Instrumental Compensation of Nonfaradaic Effects in Voltammetric Techniques,” *Anal. Chem.*, vol. 38, no. 9, pp. 1119–1129, 1966.
- [46] P. W. Atkins and J. De Paula, *Physikalische Chemie*. John Wiley & Sons, 2013.
- [47] M. Ciobanu, J. P. Wilburn, M. L. Krim, and D. E. Cliffl, “Fundamentals,” in *Handb. Electrochem.*, pp. 3–30, Elsevier B.V, 2007.
- [48] K. J. Vetter, *Elektrochemische Kinetik*. Springer-Verlag, 2013.
- [49] R. R. Gagné, C. A. Koval, and G. C. Lisensky, “Ferrocene as an internal standard for electrochemical measurements,” *Inorg. Chem.*, vol. 19, no. 9, pp. 2854–2855, 1980.

- 
- [50] K. Stulik, C. Amatore, K. Holub, V. Marecek, and W. Kutner, "Microelectrodes. Definitions, characterization, and applications (Technical report)," *Pure Appl. Chem.*, vol. 72, no. 8, pp. 1483–92, 2000.
- [51] F. G. Cottrell, "Der Reststrom bei galvanischer Polarisation, betrachtet als ein Diffusionsproblem," *Zeitschrift für Phys. Chemie*, vol. 42, no. 1, pp. 385–431, 1903.
- [52] C. G. Zoski, "Ultramicroelectrodes: Design, fabrication, and characterization," *Electroanalysis*, vol. 14, no. 15–16, pp. 1041–1051, 2002.
- [53] K. Aoki, "Theory of ultramicroelectrodes," *Electroanalysis*, vol. 5, no. 8, pp. 627–639, 1993.
- [54] R. J. Forster, "Microelectrodes: new dimensions in electrochemistry," *Chem. Soc. Rev.*, vol. 23, no. 4, pp. 289–297, 1994.
- [55] S. Szunerits and L. Thouin, "Microelectrode Arrays," in *Handb. Electrochem.*, no. 2, pp. 391–428, Elsevier B.V., 2007.
- [56] D. Shoup and A. Szabo, "Chronoamperometric current at finite disk electrodes," *J. Electroanal. Chem.*, vol. 140, no. 2, pp. 237–245, 1982.
- [57] K. Aoki and J. Osteryoung, "Diffusion-controlled current at the stationary finite disk electrode. Theory," *J. Electroanal. Chem.*, vol. 122, no. C, pp. 19–35, 1981.
- [58] D. W. M. Arrigan, "Nanoelectrodes, nanoelectrode arrays and their applications.," *Analyst*, vol. 129, no. 12, pp. 1157–1165, 2004.
- [59] M. Auffan, J. Rose, J. Y. Bottero, G. V. Lowry, J. P. Jolivet, and M. R. Wiesner, "Towards a definition of inorganic nanoparticles from an environmental, health and safety perspective," *Nat. Nanotechnol.*, vol. 4, no. 10, pp. 634–641, 2009.
- [60] K. J. Klabunde and R. M. Richards, *Nanoscale materials in chemistry*. John Wiley & Sons, 2009.
- [61] K. J. Klabunde, J. Stark, O. Koper, C. Mohs, D. G. Park, S. Decker, Y. Jiang, I. Lagadic, and D. Zhang, "Nanocrystals as stoichiometric reagents with unique surface chemistry," *J. Phys. Chem.*, vol. 100, no. 30, pp. 12142–12153, 1996.
- [62] C. Burda, X. Chen, R. Narayanan, and M. A. El-Sayed, "Chemistry and properties of nanocrystals of different shapes," *Chem. Rev.*, vol. 105, no. 4, pp. 1025–1102, 2005.
- [63] C. N. Rao, G. U. Kulkarni, P. J. Thomas, and P. P. Edwards, "Metal nanoparticles and their assemblies," *Chem. Soc. Rev.*, vol. 29, no. 1, pp. 27–35, 2000.

- [64] I. Khan, K. Saeed, and I. Khan, "Nanoparticles: Properties, applications and toxicities," *Arab. J. Chem.*, vol. 12, no. 7, pp. 908–931, 2019.
- [65] J. Polte, "Fundamental growth principles of colloidal metal nanoparticles - a new perspective," *CrystEngComm*, vol. 17, no. 36, pp. 6809–6830, 2015.
- [66] Murray, C. B., Kagan, R., B. M.G., C. B. Murray, C. R. Kagan, and M. G. Bawendi, "Synthesis and Characterization of Monodisperse Nanocrystals and Close-Packed Nanocrystal Assemblies," *Annu. Rev. Mater. Sci.*, vol. 30, no. 1, pp. 545–610, 2000.
- [67] K. M. Abou El-Nour, A. Eftaiha, A. Al-Warthan, and R. A. Ammar, "Synthesis and applications of silver nanoparticles," *Arab. J. Chem.*, vol. 3, no. 3, pp. 135–140, 2010.
- [68] R. A. Sperling and W. J. Parak, "Surface modification, functionalization and bioconjugation of colloidal Inorganic nanoparticles," *Philos. Trans. R. Soc. A Math. Phys. Eng. Sci.*, vol. 368, no. 1915, pp. 1333–1383, 2010.
- [69] T. Laaksonen, P. Ahonen, C. Johans, and K. Kontturi, "Stability and electrostatics of mercaptoundecanoic acid-capped gold nanoparticles with varying counterion size," *ChemPhysChem*, vol. 7, no. 10, pp. 2143–2149, 2006.
- [70] R. Pamies, J. G. H. Cifre, V. F. Espín, M. Collado-González, F. G. D. Baños, and J. G. De La Torre, "Aggregation behaviour of gold nanoparticles in saline aqueous media," *J. Nanoparticle Res.*, vol. 16, no. 4, 2014.
- [71] J. C. Love, L. A. Estroff, J. K. Kriebel, R. G. Nuzzo, and G. M. Whitesides, "Self-assembled monolayers of thiolates on metals as a form of nanotechnology," *Chem. Rev.*, vol. 105, no. 4, pp. 1103–1169, 2005.
- [72] W. B. Caldwell, D. J. Campbell, K. Chen, B. R. Herr, C. A. Mirkin, A. Malik, M. K. Durbin, P. Dutta, and K. G. Huang, "A Highly Ordered Self-Assembled Monolayer Film of an Azobenzenealkanethiol on Au (111): Electrochemical Properties and Structural Characterization by Synchrotron in-Plane X-ray Diffraction, Atomic Force Microscopy, and Surface-Enhanced Raman Spectroscopy," *J. Am. Chem. Soc.*, vol. 117, no. 22, pp. 6071–6082, 1995.
- [73] M. H. Schoenfish and J. E. Pemberton, "Air stability of alkanethiol self-assembled monolayers on silver and gold surfaces," *J. Am. Chem. Soc.*, vol. 120, no. 18, pp. 4502–5413, 1998.
- [74] M. J. Hostetler, A. C. Templeton, and R. W. Murray, "Dynamics of place-exchange reactions on monolayer-protected gold cluster molecules," *Langmuir*, vol. 15, no. 11, pp. 3782–3789, 1999.

- 
- [75] K. A. Willets and R. P. Van Duyne, "Localized Surface Plasmon Resonance Spectroscopy and Sensing," *Annu. Rev. Phys. Chem.*, vol. 58, no. 1, pp. 267–297, 2007.
- [76] S. Link and M. A. El-Sayed, "Optical properties and ultrafast dynamics of metallic nanocrystals," *Annu. Rev. Phys. Chem.*, vol. 54, no. 1, pp. 331–366, 2003.
- [77] K. L. Kelly, E. Coronado, L. L. Zhao, and G. C. Schatz, "The optical properties of metal nanoparticles: The influence of size, shape, and dielectric environment," *J. Phys. Chem. B*, vol. 107, no. 3, pp. 668–677, 2003.
- [78] D. D. Evanoff and G. Chumanov, "Synthesis and optical properties of silver nanoparticles and arrays," *ChemPhysChem*, vol. 6, no. 7, pp. 1221–1231, 2005.
- [79] J. A. Creighton and D. G. Eadon, "Ultraviolet-visible absorption spectra of the colloidal metallic elements," *J. Chem. Soc. Faraday Trans.*, vol. 87, no. 24, pp. 3881–3891, 1991.
- [80] Y. Xia and N. J. Halas, "Shape-controlled synthesis and surface plasmonic properties of metallic nanostructures," *MRS Bull.*, vol. 30, no. 5, pp. 338–348, 2005.
- [81] R. R. Sinden, *DNA structure and function*. Elsevier, 2012.
- [82] W. Saenger, *Principles of nucleic acid structure*. Springer Science & Business Media, 2013.
- [83] J. D. Watson, F. H. C. Crick, and J. D. Watson, "Molecular Structure of Nucleic Acids: A Structure for Deoxyribose Nucleic Acid," *Nature*, vol. 171, no. 4356, pp. 737–738, 1953.
- [84] T. E. Ouldrige, P. Šulc, F. Romano, J. P. Doye, and A. A. Louis, "DNA hybridization kinetics: Zippering, internal displacement and sequence dependence," *Nucleic Acids Res.*, vol. 41, no. 19, pp. 8886–8895, 2013.
- [85] S. A. Kushon, J. P. Jordan, J. L. Seifert, H. Nielsen, P. E. Nielsen, and B. A. Armitage, "Effect of secondary structure on the thermodynamics and kinetics of PNA hybridization to DNA hairpins," *J. Am. Chem. Soc.*, vol. 123, no. 44, pp. 10805–10813, 2001.
- [86] Y. Gao, L. K. Wolf, and R. M. Georgiadis, "Secondary structure effects on DNA hybridization kinetics: A solution versus surface comparison," *Nucleic Acids Res.*, vol. 34, no. 11, pp. 3370–3377, 2006.
- [87] C. Chen, W. Wang, Z. Wang, F. Wei, and X. S. Zhao, "Influence of secondary structure on kinetics and reaction mechanism of DNA hybridization," *Nucleic Acids Res.*, vol. 35, no. 9, pp. 2875–2884, 2007.

- [88] Y. Yin and X. S. Zhao, “Kinetics and dynamics of DNA hybridization,” *Acc. Chem. Res.*, vol. 44, no. 11, pp. 1172–1181, 2011.
- [89] N. E. Broude, “Stem-loop oligonucleotides: A robust tool for molecular biology and biotechnology,” *Trends Biotechnol.*, vol. 20, no. 6, pp. 249–256, 2002.
- [90] S. Burge, G. N. Parkinson, P. Hazel, A. K. Todd, and S. Neidle, “Quadruplex DNA: Sequence, topology and structure,” *Nucleic Acids Res.*, vol. 34, no. 19, pp. 5402–5415, 2006.
- [91] M. L. Bochman, K. Paeschke, and V. A. Zakian, “DNA secondary structures: Stability and function of G-quadruplex structures,” *Nat. Rev. Genet.*, vol. 13, no. 11, pp. 770–780, 2012.
- [92] H. A. Erlich, D. Gelfand, and J. J. Sninsky, “Recent advances in the polymerase chain reaction,” *Science (80-. )*, vol. 252, no. 5013, pp. 1643 – 1651, 1991.
- [93] M. J. Heller, “DNA Microarray Technology: Devices, Systems, and Applications,” *Annu. Rev. Biomed. Eng.*, vol. 4, no. 1, pp. 129–153, 2002.
- [94] S. Woo and P. W. Rothemund, “Programmable molecular recognition based on the geometry of DNA nanostructures,” *Nat. Chem.*, vol. 3, no. 8, pp. 620–627, 2011.
- [95] N. C. Seeman and H. F. Sleiman, “DNA nanotechnology,” *Nat. Rev. Mater.*, vol. 3, no. 1, pp. 1–23, 2017.
- [96] A. P. Alivisatos, K. P. Johnsson, X. Peng, T. E. Wilson, C. J. Loweth, M. P. Bruchez, and P. G. Schultz, “Organization of ‘nanocrystal molecules’ using DNA,” *Nature*, vol. 382, no. 6592, pp. 609–611, 1996.
- [97] C. A. Mirkin, R. L. Letsinger, R. C. Mucic, and J. J. Storhoff, “A DNA-based method for rationally assembling nanoparticles into macroscopic materials,” *Nature*, vol. 382, no. 6592, p. 607, 1997.
- [98] N. L. Rosi and C. A. Mirkin, “Nanostructures in biodiagnostics,” *Chem. Rev.*, vol. 105, no. 4, pp. 1547–1562, 2005.
- [99] G. Doria, J. Conde, B. Veigas, L. Giestas, C. Almeida, M. Assunção, J. Rosa, and P. V. Baptista, “Noble metal nanoparticles for biosensing applications,” *Sensors*, vol. 12, no. 2, pp. 1657–1687, 2012.
- [100] P. D. Howes, R. Chandrawati, and M. M. Stevens, “Colloidal nanoparticles as advanced biological sensors,” *Science (80-. )*, vol. 346, no. 6205, 2014.

- 
- [101] N. Geerts and E. Eiser, "DNA-functionalized colloids: Physical properties and applications," *Soft Matter*, vol. 6, no. 19, pp. 4647–4660, 2010.
- [102] S. Basu, S. Jana, S. Pande, and T. Pal, "Interaction of DNA bases with silver nanoparticles: Assembly quantified through SPRs and SERS," *J. Colloid Interface Sci.*, vol. 321, no. 2, pp. 288–293, 2008.
- [103] H. Kimura-Suda, D. Y. Petrovykh, M. J. Tarlov, and L. J. Whitman, "Base-dependent competitive adsorption of single-stranded DNA on gold," *J. Am. Chem. Soc.*, vol. 125, no. 30, pp. 9014–9015, 2003.
- [104] M. Östblom, B. Liedberg, L. M. Demers, and C. A. Mirkin, "On the structure and desorption dynamics of DNA bases adsorbed on gold: A temperature-programmed study," *J. Phys. Chem. B*, vol. 109, no. 31, pp. 15150–15160, 2005.
- [105] T. M. Herne and M. J. Tarlov, "Characterization of DNA probes immobilized on gold surfaces," *J. Am. Chem. Soc.*, vol. 119, no. 38, pp. 8916–8920, 1997.
- [106] S. R. Nicewarner Peña, S. Raina, G. P. Goodrich, N. V. Fedoroff, and C. D. Keating, "Hybridization and enzymatic extension of Au nanoparticle-bound oligonucleotides," *J. Am. Chem. Soc.*, vol. 124, no. 25, pp. 7314–7323, 2002.
- [107] L. M. Demers, C. A. Mirkin, R. C. Mucic, R. A. Reynolds, R. L. Letsinger, R. Elghariani, and G. Viswanadham, "A fluorescence-based method for determining the surface coverage and hybridization efficiency of thiol-capped oligonucleotides bound to gold thin films and nanoparticles," *Anal. Chem.*, vol. 72, no. 22, pp. 5535–5541, 2000.
- [108] S. J. Hurst, A. K. R. Lytton-Jean, and C. A. Mirkin, "Maximizing DNA loading on a range of gold nanoparticle sizes," *Anal. Chem.*, vol. 78, no. 24, pp. 8313–8318, 2006.
- [109] S. M. Schreiner, D. F. Shudy, A. L. Hatoh, A. Opdahl, L. J. Whitman, and D. Y. Petrovykh, "Controlled and efficient hybridization achieved with DNA probes immobilized solely through preferential DNA-substrate interactions," *Anal. Chem.*, vol. 82, no. 7, pp. 2803–2810, 2010.
- [110] H. Pei, F. Li, Y. Wan, M. Wei, H. Liu, Y. Su, N. Chen, Q. Huang, and C. Fan, "Designed diblock oligonucleotide for the synthesis of spatially isolated and highly hybridizable functionalization of DNA-gold nanoparticle nanoconjugates," *J. Am. Chem. Soc.*, vol. 134, no. 29, pp. 11876–11879, 2012.
- [111] P. Gong and R. Levicky, "DNA surface hybridization regimes," *Proc. Natl. Acad. Sci. U. S. A.*, vol. 105, no. 14, pp. 5301–5306, 2008.

- [112] C. Chen, W. Wang, J. Ge, and X. S. Zhao, "Kinetics and thermodynamics of DNA hybridization on gold nanoparticles," *Nucleic Acids Res.*, vol. 37, no. 11, pp. 3756–3765, 2009.
- [113] A. Takashima and M. Oishi, "Kinetic study of DNA hybridization on DNA-modified gold nanoparticles with engineered nano-interfaces," *RSC Adv.*, vol. 5, no. 93, pp. 76014–76018, 2015.
- [114] S. E. F. Kleijn, S. C. S. Lai, M. T. M. Koper, and P. R. Unwin, "Electrochemistry of nanoparticles," *Angew. Chemie - Int. Ed.*, vol. 53, no. 14, pp. 3558–3586, 2014.
- [115] S. M. Oja, Y. Fan, C. M. Armstrong, P. Defnet, and B. Zhang, "Nanoscale Electrochemistry Revisited," *Anal. Chem.*, vol. 88, no. 1, pp. 414–430, 2016.
- [116] S. M. Oja, M. Wood, and B. Zhang, "Nanoscale electrochemistry," *Anal. Chem.*, vol. 85, no. 2, pp. 473–486, 2013.
- [117] F. T. Patrice, K. Qiu, Y.-L. Ying, and Y.-T. Long, "Single Nanoparticle Electrochemistry," *Annu. Rev. Anal. Chem.*, vol. 12, no. 1, pp. 347–370, 2019.
- [118] S. J. Kwon, H. Zhou, F.-R. F. Fan, V. Vorobyev, B. Zhang, and A. J. Bard, "Stochastic electrochemistry with electrocatalytic nanoparticles at inert ultramicroelectrodes-theory and experiments," *Phys. Chem. Chem. Phys.*, vol. 13, no. 12, p. 5394, 2011.
- [119] B. M. Quinn, P. G. Van 't Hof, and S. G. Lemay, "Time-resolved electrochemical detection of discrete adsorption events," *J. Am. Chem. Soc.*, vol. 126, no. 27, pp. 8360–8361, 2004.
- [120] J. Poon, C. Batchelor-McAuley, K. Tschulik, and R. G. Compton, "Single graphene nanoplatelets: capacitance, potential of zero charge and diffusion coefficient," *Chem. Sci.*, vol. 6, no. 5, pp. 2869–2876, 2015.
- [121] A. N. Sekretaryova, M. Y. Vagin, A. P. F. Turner, and M. Eriksson, "Electrocatalytic currents from single enzyme molecules," *J. Am. Chem. Soc.*, vol. 138, no. 8, pp. 2504–2507, 2016.
- [122] E. Kätelhön, L. Sepunaru, A. A. Karyakin, and R. G. Compton, "Can nanoimpacts detect single-enzyme activity? Theoretical considerations and an experimental study of catalase impacts," *Acs Catal.*, vol. 6, no. 12, pp. 8313–8320, 2016.
- [123] E. Lebegue, C. M. Anderson, J. E. Dick, L. J. Webb, and A. J. Bard, "Electrochemical detection of single phospholipid vesicle collisions at a Pt ultramicroelectrode," *Langmuir*, vol. 31, no. 42, pp. 11734–11739, 2015.

- 
- [124] B.-K. Kim, A. Boika, J. Kim, J. E. Dick, and A. J. Bard, "Characterizing Emulsions by Observation of Single Droplet Collisions- Attoliter Electrochemical Reactors," *J. Am. Chem. Soc.*, vol. 136, no. 13, pp. 4849–4852, 2014.
- [125] H. S. Toh and R. G. Compton, "Electrochemical detection of single micelles through 'nano-impacts'," *Chem. Sci.*, vol. 6, no. 8, pp. 5053–5058, 2015.
- [126] D. W. M. Arrigan, *Electrochemical strategies in detection science*. No. 6, Royal Society of Chemistry, 2016.
- [127] X. Xiao and A. J. Bard, "Observing single nanoparticle collisions at an ultramicroelectrode by electrocatalytic amplification," *J. Am. Chem. Soc.*, vol. 129, no. 31, pp. 9610–9612, 2007.
- [128] Y. Xiao, F. R. F. Fan, J. Zhou, and A. J. Bard, "Current transients in single nanoparticle collision events," *J. Am. Chem. Soc.*, vol. 130, no. 49, pp. 16669–16677, 2008.
- [129] Y.-G. Zhou, N. V. Rees, and R. G. Compton, "The Electrochemical Detection and Characterization of Silver Nanoparticles in Aqueous Solution," *Angew. Chemie Int. Ed.*, vol. 50, no. 18, pp. 4219–4221, 2011.
- [130] Y. G. Zhou, N. V. Rees, and R. G. Compton, "Electrode-nanoparticle collisions: The measurement of the sticking coefficient of silver nanoparticles on a glassy carbon electrode," *Chem. Phys. Lett.*, vol. 514, no. 4-6, pp. 291–293, 2011.
- [131] B. Haddou, N. V. Rees, and R. G. Compton, "Nanoparticle-electrode impacts: the oxidation of copper nanoparticles has slow kinetics.," *Phys. Chem. Chem. Phys.*, vol. 14, no. 39, pp. 13612–7, 2012.
- [132] E. Kätelhön and R. G. R. Compton, "Understanding nano-impacts: Impact times and near-wall hindered diffusion," *Chem. Sci.*, vol. 5, no. 12, pp. 4592–4598, 2014.
- [133] K. J. Krause, K. Mathwig, B. Wolfrum, and S. G. Lemay, "Brownian motion in electrochemical nanodevices," *Eur. Phys. J. Spec. Top.*, vol. 223, no. 14, pp. 3165–3178, 2014.
- [134] H. Brenner, "The slow motion of a sphere through a viscous fluid towards a plane surface," *Chem. Eng. Sci.*, vol. 16, no. 3-4, pp. 242–251, 1961.
- [135] A. J. Goldman, R. G. Cox, and H. Brenner, "Slow viscous motion of a sphere parallel to a plane wall-I Motion through a quiescent fluid," *Chem. Eng. Sci.*, vol. 22, no. 4, pp. 637–651, 1967.
- [136] P. Sharma, S. Ghosh, S. Bhattacharya, A. You, M. A. Y. Be, and I. In, "A high-precision study of hindered diffusion near a wall," *Appl. Phys. Lett.*, vol. 97, no. 10, pp. 1–4, 2010.



- [137] W. Ma, H. Ma, J.-F. Chen, Y.-Y. Peng, Z.-Y. Yang, H.-F. Wang, Y.-L. Ying, H. Tian, and Y.-T. Long, "Tracking motion trajectories of individual nanoparticles using time-resolved current traces," *Chem. Sci.*, vol. 8, no. 3, pp. 1854–1861, 2017.
- [138] D. M. Adams, L. Brus, C. E. Chidsey, S. Creager, C. Creutz, C. R. Kagan, P. V. Kamat, M. Lieberman, S. Lindsay, R. A. Marcus, R. M. Metzger, M. E. Michel-Beyerle, J. R. Miller, M. D. Newton, D. R. Rolison, O. Sankey, K. S. Schanze, J. Yardley, and X. Zhu, "Charge transfer on the nanoscale: Current status," *J. Phys. Chem. B*, vol. 107, no. 28, pp. 6668–6697, 2003.
- [139] C. M. Hill, J. Kim, and A. J. Bard, "Electrochemistry at a Metal Nanoparticle on a Tunneling Film: A Steady-State Model of Current Densities at a Tunneling Ultramicroelectrode," *J. Am. Chem. Soc.*, vol. 137, no. 35, pp. 11321–11326, 2015.
- [140] K. J. Krause, *Microfabricated Electrode Arrays as a Tool for the Investigation of Diffusion Limited Electrochemistry at the Nanoscale*. PhD thesis, RWTH Aachen University, 2017.
- [141] "Gamry Instruments, [Online]. Available: <https://www.gamry.com/application-notes/instrumentation/potentiostat-fundamentals/>. [Accessed: 29 September 2020]."
- [142] S. Trasatti and O. A. Petrii, "Real surface area measurements in electrochemistry," *Pure Appl. Chem.*, vol. 63, no. 5, pp. 711–734, 1991.
- [143] R. Sarpeshkar, "Low-power transimpedance amplifiers and photoreceptors," in *Ultra Low Power Bioelectron. Fundam. Biomed. Appl. Bio-Inspired Syst.*, vol. 1, pp. 275–300, Cambridge University Press, 2011.
- [144] K. J. Krause, N. Adly, A. Yakushenko, J. Schnitker, D. Mayer, A. Offenhäusser, and B. Wolfrum, "Influence of Self-Assembled Alkanethiol Monolayers on Stochastic Amperometric On-Chip Detection of Silver Nanoparticles," *Anal. Chem.*, vol. 88, no. 7, pp. 3632–3637, 2016.
- [145] P. G. Figueiredo, L. Grob, P. Rinklin, K. J. Krause, and B. Wolfrum, "On-Chip Stochastic Detection of Silver Nanoparticles without a Reference Electrode," *ACS Sensors*, vol. 3, no. 1, pp. 93–98, 2018.
- [146] R. Mancini, "Op amp stability and input capacitance," *Texas Instruments*, 2004.
- [147] M. Zuker, "Mfold web server for nucleic acid folding and hybridization prediction," *Nucleic Acids Res.*, vol. 31, no. 13, pp. 3406–3415, 2003.
- [148] "<https://www.sigmaaldrich.com/catalog/product/aldrich/730785?lang=de&region=DE>."

- 
- [149] B. Liu and J. Liu, "Methods for preparing DNA-functionalized gold nanoparticles, a key reagent of bioanalytical chemistry," *Anal. Methods*, vol. 9, no. 18, pp. 2633–2643, 2017.
- [150] K. A. Huynh and K. L. Chen, "Aggregation kinetics of citrate and polyvinylpyrrolidone coated silver nanoparticles in monovalent and divalent electrolyte solutions," *Environ. Sci. Technol.*, vol. 45, no. 13, pp. 5564–5571, 2011.
- [151] T. M. Alligrant, R. Dasari, K. J. Stevenson, and R. M. Crooks, "Electrocatalytic Amplification of Single Nanoparticle Collisions Using DNA-Modified Surfaces," *Langmuir*, vol. 31, no. 42, pp. 11724–11733, 2015.
- [152] H. Zipper, H. Brunner, J. Bernhagen, and F. Vitzthum, "Investigations on DNA intercalation and surface binding by SYBR Green I, its structure determination and methodological implications," *Nucleic Acids Res.*, vol. 32, no. 12, 2004.
- [153] C. A. Schneider, W. S. Rasband, and K. W. Eliceiri, "NIH Image to ImageJ: 25 years of image analysis," *Nat. Methods*, vol. 9, no. 7, pp. 671–675, 2012.
- [154] Y. Cao, R. Jin, and C. A. Mirkin, "DNA-modified core-shell Ag/Au nanoparticles," *J. Am. Chem. Soc.*, vol. 123, no. 32, pp. 7961–7962, 2001.
- [155] I. Tokareva and E. Hutter, "Hybridization of Oligonucleotide-Modified Silver and Gold Nanoparticles in Aqueous Dispersions and on Gold Films," *J. Am. Chem. Soc.*, vol. 126, no. 48, pp. 15784–15789, 2004.
- [156] H. Cai, Y. Xu, N. Zhu, P. He, and Y. Fang, "An electrochemical DNA hybridization detection assay based on a silver nanoparticle label," *Analyst*, vol. 127, no. 6, pp. 803–808, 2002.
- [157] D. G. Thompson, A. Enright, K. Faulds, W. E. Smith, and D. Graham, "Ultrasensitive DNA Detection Using Oligonucleotide - Silver Nanoparticle Conjugates," *Anal. Chem.*, vol. 80, no. 8, pp. 15784–15789, 2008.
- [158] B. C. Vidal, T. C. Deivaraj, J. Yang, H. P. Too, G. M. Chow, L. M. Gan, and J. Y. Lee, "Stability and hybridization-driven aggregation of silver nanoparticle-oligonucleotide conjugates," *New J. Chem.*, vol. 29, no. 6, pp. 812–816, 2005.
- [159] X. Zhang, M. R. Servos, and J. Liu, "Fast pH-assisted functionalization of silver nanoparticles with monothiolated DNA," *Chem. Commun.*, vol. 48, no. 81, pp. 10114–10116, 2012.

- [160] Y. Zheng, Y. Li, and Z. Deng, "Silver nanoparticle-DNA bionanoconjugates bearing a discrete number of DNA ligands," *Chem. Commun.*, vol. 48, no. 49, pp. 6160–6162, 2012.
- [161] H. Hinterwirth, S. Kappel, T. Waitz, T. Prohaska, and W. Lindner, "Quantifying Thiol Ligand Density of Self-Assembled Monolayers on Gold Nanoparticles by Inductively Coupled Plasma- Mass Spectrometry," *ACS Nano*, vol. 7, no. 2, pp. 1129–1136, 2013.
- [162] X. Zhang, T. Gouriye, K. Göeken, M. R. Servos, R. Gill, and J. Liu, "Toward fast and quantitative modification of large gold nanoparticles by thiolated DNA: Scaling of nanoscale forces, kinetics, and the need for thiol reduction," *J. Phys. Chem. C*, vol. 117, no. 30, pp. 15677–15684, 2013.
- [163] S. Nath, S. K. Ghosh, S. Kundu, S. Praharaj, S. Panigrahi, and T. Pal, "Is gold really softer than silver? HSAB principle revisited," *J. Nanoparticle Res.*, vol. 8, no. 1, pp. 111–116, 2006.
- [164] J. J. Storhoff, R. Elghanian, R. C. Mucic, C. A. Mirkin, and R. L. Letsinger, "One-pot colorimetric differentiation of polynucleotides with single base imperfections using gold nanoparticle probes," *J. Am. Chem. Soc.*, vol. 120, no. 9, pp. 1959–1964, 1998.
- [165] C. Pfeiffer, C. Rehbock, D. Hühn, C. Carrillo-Carrion, D. J. De Aberasturi, V. Merk, S. Barcikowski, and W. J. Parak, "Interaction of colloidal nanoparticles with their local environment: The (ionic) nanoenvironment around nanoparticles is different from bulk and determines the physico-chemical properties of the nanoparticles," *J. R. Soc. Interface*, vol. 11, no. 96, 2014.
- [166] X. Zhang, M. R. Servos, and J. Liu, "Surface science of DNA adsorption onto citrate-capped gold nanoparticles," *Langmuir*, vol. 28, no. 8, pp. 3896–3902, 2012.
- [167] S. V. Sokolov, K. Tschulik, C. Batchelor-McAuley, K. Jurkschat, and R. G. Compton, "Reversible or Not? Distinguishing Agglomeration and Aggregation at the Nanoscale," *Anal. Chem.*, vol. 87, no. 19, pp. 10033–10039, 2015.
- [168] P. Mulvaney, "Surface plasmon spectroscopy of nanosized metal particles," *Langmuir*, vol. 12, no. 3, pp. 788–800, 1996.
- [169] R. I. MacCuspie, "Colloidal stability of silver nanoparticles in biologically relevant conditions," *J. Nanoparticle Res.*, vol. 13, no. 7, pp. 2893–2908, 2011.
- [170] N. Bhatt, P. J. J. Huang, N. Dave, and J. Liu, "Dissociation and degradation of thiol-modified DNA on gold nanoparticles in aqueous and organic solvents," *Langmuir*, vol. 27, no. 10, pp. 6132–6137, 2011.

- 
- [171] R. Wu, L. P. Jiang, J. J. Zhu, and J. Liu, "Effects of Small Molecules on DNA Adsorption by Gold Nanoparticles and a Case Study of Tris(2-carboxyethyl)phosphine (TCEP)," *Langmuir*, vol. 35, no. 41, pp. 13461–13468, 2019.
- [172] E. Tomaszewska, K. Soliwoda, K. Kadziola, B. Tkacz-Szczesna, G. Celichowski, M. Cichomski, W. Szmaja, and J. Grobelny, "Detection limits of DLS and UV-Vis spectroscopy in characterization of polydisperse nanoparticles colloids," *J. Nanomater.*, vol. 2013, 2013.
- [173] A. M. El Badawy, T. P. Luxton, R. G. Silva, K. G. Scheckel, M. T. Suidan, and T. M. Tolaymat, "Impact of environmental conditions (pH, ionic strength, and electrolyte type) on the surface charge and aggregation of silver nanoparticles suspensions," *Environ. Sci. Technol.*, vol. 44, no. 4, pp. 1260–1266, 2010.
- [174] Y. Agrawal and V. Patel, "Nanosuspension: An approach to enhance solubility of drugs," *J. Adv. Pharm. Technol. Res.*, vol. 2, no. 2, p. 81, 2011.
- [175] Malvern Instruments, "Zeta potential: An Introduction in 30 minutes," *Zetasizer Nano Serles Tech. Note. MRK654-01*, vol. 2, pp. 1–6, 2011.
- [176] K. B. Cederquist and C. D. Keating, "Curvature effects in DNA: Au nanoparticle conjugates," *ACS Nano*, vol. 3, no. 2, pp. 256–260, 2009.
- [177] F. Schreiber, "Structure and growth of self-assembling monolayers," *Prog. Surf. Sci.*, vol. 65, no. 5-8, pp. 151–257, 2000.
- [178] D. S. Karpovich and G. J. Blanchard, "Direct Measurement of the Adsorption Kinetics of Alkanethiolate Self-Assembled Monolayers on a Microcrystalline Gold Surface," *Langmuir*, vol. 10, no. 9, pp. 3315–3322, 1994.
- [179] H. M. Schessler, D. S. Karpovich, and G. J. Blanchard, "Quantitating the balance between enthalpic and entropic forces in alkanethiol/gold monolayer self assembly," *J. Am. Chem. Soc.*, vol. 118, no. 40, pp. 9645–9651, 1996.
- [180] V. Chan, D. J. Graves, P. Fortina, and S. E. McKenzie, "Adsorption and Surface Diffusion of DNA Oligonucleotides at Liquid/Solid Interfaces," *Langmuir*, vol. 13, no. 2, pp. 320–329, 1997.
- [181] M. Yang, H. C. Yau, and H. L. Chan, "Adsorption kinetics and ligand-binding properties of thiol-modified double-stranded DNA on a gold surface," *Langmuir*, vol. 14, no. 21, pp. 6121–6129, 1998.

- [182] R. Marie, H. Jensenius, J. Thaysen, C. B. Christensen, and A. Boisen, "Adsorption kinetics and mechanical properties of thiol-modified DNA-oligos on gold investigated by microcantilever sensors," *Ultramicroscopy*, vol. 91, no. 1-4, pp. 29–36, 2002.
- [183] P. Sandström, M. Boncheva, and B. Åkerman, "Nonspecific and thiol-specific binding of DNA to gold nanoparticles," *Langmuir*, vol. 19, no. 18, pp. 7537–7543, 2003.
- [184] A. B. Steel, R. L. Levicky, T. M. Herne, and M. J. Tarlov, "Immobilization of nucleic acids at solid surfaces: Effect of oligonucleotide length on layer assembly," *Biophys. J.*, vol. 79, no. 2, pp. 975–981, 2000.
- [185] W. J. Parak, T. Pellegrino, C. M. Micheel, D. Gerion, S. C. Williams, and A. P. Alivisatos, "Conformation of oligonucleotides attached to gold nanocrystals probed by gel electrophoresis," *Nano Lett.*, vol. 3, no. 1, pp. 33–36, 2003.
- [186] J. Liu, "Adsorption of DNA onto gold nanoparticles and graphene oxide: Surface science and applications," *Phys. Chem. Chem. Phys.*, vol. 14, no. 30, pp. 10485–10496, 2012.
- [187] S. Xu, S. J. Cruchon-Dupeyrat, J. C. Garno, G. Y. Liu, G. K. Jennings, T. H. Yong, and P. E. Laibinis, "In situ studies of thiol self-assembly on gold from solution using atomic force microscopy," *J. Chem. Phys.*, vol. 108, no. 12, pp. 5002–5012, 1998.
- [188] D. B. Hibbert, J. J. Gooding, and P. Erokhin, "Kinetics of Irreversible Adsorption with Diffusion : Application to Biomolecule Immobilization," *Langmuir*, vol. 18, no. 5, pp. 1770–1776, 2002.
- [189] A. M. Smith, A. A. Lee, and S. Perkin, "The Electrostatic Screening Length in Concentrated Electrolytes Increases with Concentration," *J. Phys. Chem. Lett.*, vol. 7, no. 12, pp. 2157–2163, 2016.
- [190] S. J. Kwon and A. J. Bard, "DNA analysis by application of Pt nanoparticle electrochemical amplification with single label response," *J. Am. Chem. Soc.*, vol. 134, no. 26, pp. 10777–10779, 2012.
- [191] A. D. Castañeda, D. A. Robinson, K. J. Stevenson, and R. M. Crooks, "Electrocatalytic amplification of DNA-modified nanoparticle collisions via enzymatic digestion," *Chem. Sci.*, vol. 7, no. 10, pp. 6450–6457, 2016.
- [192] A. F. Johnstone, G. W. Gross, D. G. Weiss, O. H. Schroeder, A. Gramowski, and T. J. Shafer, "Microelectrode arrays: A physiologically based neurotoxicity testing platform for the 21st century," *Neurotoxicology*, vol. 31, no. 4, pp. 331–350, 2010.

- 
- [193] M. E. J. Obien, K. Deligkaris, T. Bullmann, D. J. Bakkum, and U. Frey, "Revealing neuronal function through microelectrode array recordings," *Front. Neurosci.*, vol. 8, p. 423, 2015.
- [194] J. Yao and K. D. Gillis, "Quantification of noise sources for amperometric measurement of quantal exocytosis using microelectrodes," *Analyst*, vol. 137, no. 11, pp. 2674–2681, 2012.
- [195] A. Yakushenko, E. Kätelhön, and B. Wolfrum, "Parallel on-chip analysis of single vesicle neurotransmitter release," *Anal. Chem.*, vol. 85, no. 11, pp. 5483–5490, 2013.
- [196] S. T. Larsen, M. L. Heien, and R. Taboryski, "Amperometric noise at thin film band electrodes," *Anal. Chem.*, vol. 84, no. 18, pp. 7744–7749, 2012.
- [197] D. Kim, B. Goldstein, W. Tang, F. J. Sigworth, and E. Culurciello, "Noise analysis and performance comparison of low current measurement systems for biomedical applications," *IEEE Trans. Biomed. Circuits Syst.*, vol. 7, no. 1, pp. 52–62, 2013.
- [198] J. T. Long and S. G. Weber, "Noise at Microelectrodes and Microelectrode Arrays in Amperometry and Voltammetry," *Anal. Chem.*, vol. 60, no. 20, pp. 2309–2311, 1988.
- [199] S. Bell, "Measurement good practice guide No. 11," *Natl. Phys. Lab.*, no. 2, pp. 1–41, 2004.
- [200] H. S. Toh, C. Batchelor-McAuley, K. Tschulik, and R. G. Compton, "Electrochemical detection of chloride levels in sweat using silver nanoparticles: A basis for the preliminary screening for cystic fibrosis," *Analyst*, vol. 138, no. 15, pp. 4292–4297, 2013.
- [201] A. J. Bard, R. Parsons, and J. Jordan, *Standard potentials in aqueous solution*, vol. 6. CRC press, 1985.
- [202] R. G. Bates and J. B. Macaskill, "Standard Potential of the Silver-Silver Chloride Electrode," *Pure Appl. Chem.*, vol. 50, no. 11-12, pp. 1701–1706, 1978.
- [203] D. A. Robinson, Y. Liu, M. A. Edwards, N. J. Vitti, S. M. Oja, B. Zhang, and H. S. White, "Collision Dynamics during the Electrooxidation of Individual Silver Nanoparticles," *J. Am. Chem. Soc.*, vol. 139, no. 46, pp. 16923–16931, 2017.
- [204] C. A. Little, X. Li, C. Batchelor-McAuley, N. P. Young, and R. G. Compton, "Particle-electrode impacts: Evidencing partial versus complete oxidation via variable temperature studies," *J. Electroanal. Chem.*, vol. 823, no. May, pp. 492–498, 2018.
- [205] L. Sun, W. Wang, and H. Y. Chen, "Dynamic Nanoparticle-Substrate Contacts Regulate Multi-Peak Behavior of Single Silver Nanoparticle Collisions," *ChemElectroChem*, vol. 5, no. 20, pp. 2995–2999, 2018.

- [206] J. Ellison, C. Batchelor-McAuley, K. Tschulik, and R. G. Compton, "The use of cylindrical micro-wire electrodes for nano-impact experiments; Facilitating the sub-picomolar detection of single nanoparticles," *Sensors Actuators, B Chem.*, vol. 200, pp. 47–52, 2014.
- [207] X. Yuan, N. Wolf, T. J. Hondrich, P. Shokoohimehr, F. Milos, M. Glass, D. Mayer, V. Maybeck, M. Prömpers, A. Offenhäusser, and R. Wördenweber, "Engineering Biocompatible Interfaces via Combinations of Oxide Films and Organic Self-Assembled Monolayers," *ACS Appl. Mater. Interfaces*, vol. 12, no. 14, pp. 17121–17129, 2020.
- [208] X. Xiao, S. Pan, J. S. Jang, F. R. F. Fan, and A. J. Bard, "Single nanoparticle electrocatalysis: Effect of monolayers on particle and electrode on electron transfer," *J. Phys. Chem. C*, vol. 113, no. 33, pp. 14978–14982, 2009.
- [209] L. Kergoat, B. Piro, M. Berggren, M.-C. Pham, A. Yassar, and G. Horowitz, "DNA detection with a water-gated organic field-effect transistor," *Org. Electron.*, vol. 13, no. 1, pp. 1–6, 2012.
- [210] M. C. Pham, B. Piro, D. Tran, T. Ledoan, and L. H. Dao, "Direct Electrochemical Detection of Oligonucleotide Hybridization on Poly(5-hydroxy-1,4-naphthoquinone- co-5-hydroxy-3-thioacetic Acid-1,4-naphthoquinone) Film," *Anal. Chem.*, vol. 75, no. 23, pp. 6748–6752, 2003.
- [211] S. Reisberg, B. Piro, V. Noël, and M. C. Pham, "DNA electrochemical sensor based on conducting polymer: Dependence of the "signal-on" detection on the probe sequence localization," *Anal. Chem.*, vol. 77, no. 10, pp. 3351–3356, 2005.
- [212] K. Tschulik, W. Cheng, C. Batchelor-McAuley, S. Murphy, D. Omanović, and R. G. Compton, "Non-Invasive Probing of Nanoparticle Electrostatics," *ChemElectroChem*, vol. 2, no. 1, pp. 112–118, 2015.
- [213] L. V. Stebounova, E. Guio, and V. H. Grassian, "Silver nanoparticles in simulated biological media: A study of aggregation, sedimentation, and dissolution," *J. Nanoparticle Res.*, vol. 13, no. 1, pp. 233–244, 2011.
- [214] J. H. Park, A. Boika, H. S. Park, H. C. Lee, and A. J. Bard, "Single collision events of conductive nanoparticles driven by migration," *J. Phys. Chem. C*, vol. 117, no. 13, pp. 6651–6657, 2013.
- [215] L. Bousse, S. Mostarshed, B. Van Der Shoot, N. F. de Rooij, P. Gimmel, and W. Göpel, "Zeta potential measurements of Ta2O5 and SiO2 thin films," *J. Colloid Interface Sci.*, vol. 147, no. 1, pp. 22–32, 1991.

- 
- [216] T. H. E. Odijk, "Polyelectrolytes near the rod limit," *J. Polym. Sci. Polym. Phys. Ed.*, vol. 15, no. 3, pp. 477–483, 1977.
- [217] J.-L. Barrat and J.-F. Joanny, "Persistence length of polyelectrolyte chains," *Europhys. Lett.*, vol. 24, no. 5, p. 333, 1993.
- [218] Y. Zhang, H. Zhou, and Z. C. Ou-Yang, "Stretching single-stranded DNA: Interplay of electrostatic, base-pairing, and base-pair stacking interactions," *Biophys. J.*, vol. 81, no. 2, pp. 1133–1143, 2001.
- [219] A. Gubarev, J.-m. Y. Carrillo, and A. V. Dobrynin, "Scale-Dependent Electrostatic Stiffening in Biopolymers," *Macromolecules*, vol. 42, no. 15, pp. 5851–5860, 2009.
- [220] A. Y. Sim, J. Lipfert, D. Herschlag, and S. Doniach, "Salt dependence of the radius of gyration and flexibility of single-stranded DNA in solution probed by small-angle x-ray scattering," *Phys. Rev. E*, vol. 86, no. 2, pp. 1–5, 2012.
- [221] A. Bosco, J. Camunas-Soler, and F. Ritort, "Elastic properties and secondary structure formation of single-stranded DNA at monovalent and divalent salt conditions," *Nucleic Acids Res.*, vol. 42, no. 3, pp. 2064–2074, 2014.
- [222] B. Liu, A. J. Bard, M. V. Mirkin, and S. E. Creager, "Electron Transfer at Self-Assembled Monolayers Measured by Scanning Electrochemical Microscopy," *J. Am. Chem. Soc.*, vol. 126, no. 5, pp. 1485–1492, 2004.
- [223] C. R. Bradbury, J. Zhao, and D. J. Fermín, "Distance-independent charge-transfer resistance at gold electrodes modified by thiol monolayers and metal nanoparticles," *J. Phys. Chem. C*, vol. 112, no. 27, pp. 10153–10160, 2008.
- [224] H. Cohen, C. Nogues, D. Ullien, S. Daube, R. Naaman, and D. Porath, "Electrical characterization of self-assembled single- and double-stranded DNA monolayers using conductive AFM," *Faraday Discuss.*, vol. 131, pp. 367–376, 2006.
- [225] J. Zhao, C. R. Bradbury, and D. J. Fermín, "Long-range electronic communication between metal nanoparticles and electrode surfaces separated by polyelectrolyte multilayer films," *J. Phys. Chem. C*, vol. 112, no. 17, pp. 6832–6841, 2008.
- [226] J. N. Chazalviel and P. Allongue, "On the origin of the efficient nanoparticle mediated electron transfer across a self-assembled monolayer," *J. Am. Chem. Soc.*, vol. 133, no. 4, pp. 762–764, 2011.
- [227] A. Barfidokht, S. Ciampi, E. Luais, N. Darwish, and J. J. Gooding, "Distance-dependent electron transfer at passivated electrodes decorated by gold nanoparticles," *Anal. Chem.*, vol. 85, no. 2, pp. 1073–1080, 2013.



- [228] S. Abbasian, A. Moshaii, M. Nikkhah, and N. Farkhari, "Adsorption of DNA on colloidal Ag nanoparticles: Effects of nanoparticle surface charge, base content and length of DNA," *Colloids Surfaces B Biointerfaces*, vol. 116, pp. 439–445, 2014.
- [229] N. Farkhari, S. Abbasian, A. Moshaii, and M. Nikkhah, "Mechanism of adsorption of single and double stranded DNA on gold and silver nanoparticles: investigating some important parameters in bio-sensing applications," *Colloids Surfaces B Biointerfaces*, vol. 148, pp. 657–664, 2016.
- [230] T. Pellegrino, R. A. Sperling, A. P. Alivisatos, and W. J. Parak, "Gel Electrophoresis of Gold-DNA Nanoconjugates," *J. Biomed. Biotechnol.*, vol. 2007, 2007.
- [231] J. W. Park and J. S. Shumaker-Parry, "Structural study of citrate layers on gold nanoparticles: Role of intermolecular interactions in stabilizing nanoparticles," *J. Am. Chem. Soc.*, vol. 136, no. 5, pp. 1907–1921, 2014.
- [232] B. Tinland, A. Pluen, J. Sturm, and G. Weill, "Persistence length of single-stranded DNA," *Macromolecules*, vol. 30, no. 19, pp. 5763–5765, 1997.
- [233] S. V. Kuznetsov, Y. Shen, A. S. Benight, and A. Ansari, "A semiflexible polymer model applied to loop formation in DNA hairpins," *Biophys. J.*, vol. 81, no. 5, pp. 2864–2875, 2001.
- [234] F. J. Mearns, E. L. Wong, K. Short, D. B. Hibbert, and J. J. Gooding, "DNA biosensor concepts based on a change in the DNA persistence length upon hybridization," *Electroanalysis*, vol. 18, no. 19-20, pp. 1971–1981, 2006.
- [235] Z. Li, S. C. Chang, and R. S. Williams, "Self-assembly of alkanethiol molecules onto platinum and platinum oxide surfaces," *Langmuir*, vol. 19, no. 17, pp. 6744–6749, 2003.
- [236] C. Yuan, H. Chen, X. W. Lou, and L. A. Archer, "DNA bending stiffness on small length scales," *Phys. Rev. Lett.*, vol. 100, no. 1, pp. 1–4, 2008.
- [237] J. Ambia-Garrido, A. Vainrub, and B. M. Pettitt, "A model for structure and thermodynamics of ssDNA and dsDNA near a surface: A coarse grained approach," *Comput. Phys. Commun.*, vol. 181, no. 12, pp. 2001–2007, 2010.
- [238] M. Steichen and C. Buess-Herman, "Electrochemical detection of the immobilization and hybridization of unlabeled linear and hairpin DNA on gold," *Electrochem. commun.*, vol. 7, no. 4, pp. 416–420, 2005.
- [239] B. Giese, J. Amaudrut, A. K. Köhler, M. Spormann, and S. Wessely, "Direct observation of hole transfer through DNA by hopping between adenine bases and by tunnelling," *Nature*, vol. 412, no. 6844, pp. 318–320, 2001.

- 
- [240] H. Cohen, C. Nogues, R. Naaman, and D. Porath, "Direct measurement of electrical transport through single DNA molecules of complex sequence," *Proc. Natl. Acad. Sci.*, vol. 102, no. 33, pp. 11589–11593, 2005.
- [241] B. Xu, P. Zhang, X. Li, and N. Tao, "Direct conductance measurement of single DNA molecules in aqueous solution," *Nano Lett.*, vol. 4, no. 6, pp. 1105–1108, 2004.
- [242] H. Van Zalinge, D. J. Schiffrin, A. D. Bates, W. Haiss, J. Ulstrup, and R. J. Nichols, "Single-molecule conductance measurements of single- and double-stranded DNA oligonucleotides," *ChemPhysChem*, vol. 7, no. 1, pp. 94–98, 2006.
- [243] T. Kubar and M. Elstner, "What governs the charge transfer in DNA? The role of DNA conformation and environment," *J. Phys. Chem. B*, vol. 112, no. 29, pp. 8788–8798, 2008.
- [244] E. Palek and M. Fojta, "Peer Reviewed: Detecting DNA Hybridization and Damage," *Anal. Chem.*, vol. 73, no. 3, pp. 74 A–83 A, 2001.
- [245] A. Sassolas, B. D. Leca-Bouvier, and L. J. Blum, "DNA biosensors and microarrays," *Chem. Rev.*, vol. 108, no. 1, pp. 109–139, 2008.
- [246] J. SantaLucia and D. Hicks, "The thermodynamics of DNA structural motifs," *Annu. Rev. Biophys. Biomol. Struct.*, vol. 33, pp. 415–440, 2004.
- [247] Y. Shen, S. V. Kuznetsov, and A. Ansari, "Loop dependence of the dynamics of DNA hairpins," *J. Phys. Chem. B*, vol. 105, no. 48, pp. 12202–12211, 2001.
- [248] V. P. Antao, S. Y. Lai, and I. Tinoco, "A thermodynamic study of unusually stable RNA and DNA hairpins," *Nucleic Acids Res.*, vol. 19, no. 21, pp. 5901–5905, 1991.
- [249] I. Hirao, Y. Nishimura, Y.-i. Tagawa, K. Watanabe, and K.-i. Miura, "Extraordinarily stable mini-hairpins: Electrophoretical and thermal properties of the various sequence variants of D(GCFAAAGC) and their effect on DNA sequencing," *Nucleic Acids Res.*, vol. 20, no. 15, pp. 3891–3896, 1992.
- [250] D. Rentzeperis, K. Alessi, and L. A. Marky, "Thermodynamics of DNA hairpins: Contribution of loop size to hairpin stability and ethidium binding," *Nucleic Acids Res.*, vol. 21, no. 11, pp. 2683–2689, 1993.
- [251] S. Kannan and M. Zacharias, "Role of the closing base pair for d(GCA) hairpin stability: Free energy analysis and folding simulations," *Nucleic Acids Res.*, vol. 39, no. 19, pp. 8271–8280, 2011.

- [252] E. M. Moody and P. C. Bevilacqua, "Thermodynamic coupling of the loop and stem in unusually stable DNA hairpins closed by CG base pairs," *J. Am. Chem. Soc.*, vol. 125, no. 8, pp. 2032–2033, 2003.
- [253] A. I. Dragan, R. Pavlovic, J. B. McGivney, J. R. Casas-Finet, E. S. Bishop, R. J. Strouse, M. A. Schenerman, and C. D. Geddes, "SYBR Green I: Fluorescence properties and interaction with DNA," *J. Fluoresc.*, vol. 22, no. 4, pp. 1189–1199, 2012.
- [254] F. Vitzthum, G. Geiger, H. Bisswanger, H. Brunner, and J. Bernhagen, "A quantitative fluorescence-based microplate assay for the determination of double-stranded DNA using SYBR green I and a standard ultraviolet transilluminator gel imaging system," *Anal. Biochem.*, vol. 276, no. 1, pp. 59–64, 1999.
- [255] R. Rasmussen, T. Morrison, M. Herrmann, and C. Wittwer, "Quantitative PCR by Continuous Fluorescence Monitoring of a Double Strand DNA Specific Binding Dye," *Biochemica*, vol. 2, no. 8, p. 11, 1998.
- [256] H. Zipper, C. Buta, K. Lämmle, H. Brunner, J. Bernhagen, and F. Vitzthum, "Mechanisms underlying the impact of humic acids on DNA quantification by SYBR Green I and consequences for the analysis of soils and aquatic sediments.," *Nucleic Acids Res.*, vol. 31, no. 7, 2003.
- [257] F. C. Chien, J. S. Liu, H. J. Su, L. A. Kao, C. F. Chiou, W. Y. Chen, and S. J. Chen, "An investigation into the influence of secondary structures on DNA hybridization using surface plasmon resonance biosensing," *Chem. Phys. Lett.*, vol. 397, no. 4-6, pp. 429–434, 2004.
- [258] A. Vainrub and B. M. Pettitt, "Surface electrostatic effects in oligonucleotide microarrays: Control and optimization of binding thermodynamics," *Biopolymers*, vol. 68, no. 2, pp. 265–270, 2003.
- [259] A. W. Peterson, "The effect of surface probe density on DNA hybridization," *Nucleic Acids Res.*, vol. 29, no. 24, pp. 5163–5168, 2001.
- [260] B. A. Stillman and J. L. Tonkinson, "Expression microarray hybridization kinetics depend on length of the immobilized DNA but are independent of immobilization substrate," *Anal. Biochem.*, vol. 295, no. 2, pp. 149–157, 2001.
- [261] P. S. Randeria, M. R. Jones, K. L. Kohlstedt, R. J. Banga, M. Olvera De La Cruz, G. C. Schatz, and C. A. Mirkin, "What Controls the Hybridization Thermodynamics of Spherical Nucleic Acids?," *J. Am. Chem. Soc.*, vol. 137, no. 10, pp. 3486–3489, 2015.
- [262] T. M. Alligrant, E. G. Nettleton, and R. M. Crooks, "Electrochemical detection of individual DNA hybridization events," *Lab Chip*, vol. 13, no. 3, pp. 349–354, 2013.

- 
- [263] G. Bonnet, S. Tyagi, A. Libchaber, and F. R. Kramer, "Thermodynamic basis of the enhanced specificity of structured DNA probes," *Proc. Natl. Acad. Sci. U. S. A.*, vol. 96, no. 11, pp. 6171–6176, 1999.
- [264] V. Filipe, A. Hawe, and W. Jiskoot, "Critical evaluation of nanoparticle tracking analysis (NTA) by NanoSight for the measurement of nanoparticles and protein aggregates," *Pharm. Res.*, vol. 27, no. 5, pp. 796–810, 2010.
- [265] J. Kypr, I. Kejnovská, D. Renčiuk, and M. Vorlíčková, "Circular dichroism and conformational polymorphism of DNA," *Nucleic Acids Res.*, vol. 37, no. 6, pp. 1713–1725, 2009.
- [266] A. Guy, P. Jones, and S. J. Hill, "Identification and chromatographic separation of antimony species with  $\alpha$ -hydroxy acids," *Analyst*, vol. 123, no. 7, pp. 1513–1518, 1998.
- [267] H. Angerstein-Kozłowska, B. E. Conway, A. Hamelin, and L. Stoicoviciu, "Elementary steps of electrochemical oxidation of single-crystal planes of Au-I. Chemical basis of processes involving geometry of anions and the electrode surfaces," *Electrochim. Acta*, vol. 31, no. 8, pp. 1051–1061, 1986.
- [268] H. Angerstein-Kozłowska, B. E. Conway, A. Hamelin, and L. Stoicoviciu, "Elementary steps of electrochemical oxidation of single-crystal planes of Au Part II. A chemical and structural basis of oxidation of the (111) plane," *J. Electroanal. Chem.*, vol. 228, no. 1-2, pp. 429–453, 1987.
- [269] D. Dickertmann, J. W. Schultze, and K. J. Vetter, "Electrochemical formation and reduction of monomolecular oxide layers on (111) and (100) planes of gold single crystals," *J. Electroanal. Chem. Interfacial Electrochem.*, vol. 55, no. 3, pp. 429–443, 1974.



## List of Figures

2.1	Electrochemical double layer illustration and potential profile . . . . .	6
2.2	Electrode reaction pathway . . . . .	8
2.3	Potential, concentration and current profile vs. time for a chronoamperometric step experiment . . . . .	11
2.4	Microelectrode geometry with diffusion profile . . . . .	13
2.5	Illustration of nanoparticle synthesis and stabilization . . . . .	15
2.6	Schematic illustration of a localized surface plasmon . . . . .	16
2.7	Chemical formula of DNA structure . . . . .	17
2.8	Scheme of DNA hybridization and secondary structures . . . . .	19
2.9	Blocking impacts . . . . .	22
2.10	Electrocatalytic amplification impacts . . . . .	23
2.11	Material dissolution impacts . . . . .	24
2.12	Theoretical model of the space above an electrode with segmentation into four different zones . . . . .	25
3.1	Simplified schematic of the different fabrication steps of MEAs . . . . .	27
3.2	Layout of microelectrode array and sensor area . . . . .	28
3.3	Simplified circuit diagram of a potentiostat with 3 electrode setup (adapted from ref. [141]). . . . .	29
3.4	Picture of the BioMAS measurement setup consisting of the main-amplifier (top) and the pre-amplification headstage (bottom) . . . . .	30
3.5	Simplified equivalent circuit diagram of a transimpedance amplifier. . . . .	31
3.6	BioMAS measurement software interface. Parameter settings (red), live mode (blue), noisy channel (green), orientation for connection (orange). . . . .	32
3.7	Exemplary current time trace and zoom in single oxidation peak . . . . .	34
3.8	Scheme of the AgNP-DNA conjugate modification and separation procedure .	36
4.1	Scheme of the nanoparticle modification via the salt-aging procedure . . . . .	44
4.2	Image of nanoparticle solutions and corresponding UV-Vis spectra . . . . .	45
4.3	UV-Vis spectra of DNA-capped nanoparticles after 3 months storage and in high salt solution . . . . .	46
4.4	STEM image and corresponding size distribution . . . . .	48

4.5	Scheme for increasing DNA density on the nanoparticle surface . . . . .	49
4.6	Isotherms for DNA adsorption on silver nanoparticles . . . . .	50
5.1	Current-time trace and power spectral density of pure electronic setup and in combination with electrochemical setup . . . . .	57
5.2	Insertion scheme . . . . .	59
5.3	Oxidation of silver nanoparticles . . . . .	62
5.4	Exemplary current time trace and zoom in single oxidation peak . . . . .	63
5.5	Impact frequency for different concentration of AgNPs and size distribution calculated from impact charge . . . . .	64
5.6	Impact frequency for citrate- and DNA-capped AgNPs at different potentials and the corresponding size distribution . . . . .	66
5.7	Impact frequency for different potentials and electrolyte concentrations . . . .	69
5.8	Normed impact frequency for AgNP oxidation with varying concentration of NaCl in electrolyte . . . . .	71
5.9	Impact frequency for different DNA concentrations during AgNP modification	74
5.10	Scheme for DNA conformation on AgNPs . . . . .	75
5.11	Tunnelling for AgNPs with DNA modification . . . . .	76
5.12	Impact frequency for different potentials and electrolyte concentrations . . . .	77
5.13	Impact frequency for different DNA concentrations during AgNP modification	79
6.1	Fluorescence emission spectra for SYBR Green I . . . . .	85
6.2	Fluorescence emission for different single stranded DNA . . . . .	86
6.3	Fluorescence assay for DNA hybridization in solution . . . . .	88
6.4	Fluorescence assay for DNA hybridization on silver nanoparticles . . . . .	90
6.5	Fluorescence assay for DNA hybridization on silver nanoparticles . . . . .	91
6.6	Impact based detection scheme for DNA hybridization . . . . .	92
6.7	Collision nanoelectrochemistry for detection of DNA hybridization . . . . .	93
8.1	NMR of AgNP stock solution . . . . .	100
8.2	UV-Vis based calibration curve for AgNPs . . . . .	101
8.3	UV-Vis spectra of nanoparticles in PBS . . . . .	101
8.4	UV-Vis spectra of citrate and DNA-capped nanoparticles . . . . .	101
8.5	DLS intensity distributions . . . . .	102
8.6	Zeta potential distribution . . . . .	102
8.7	UV-Vis spectra of centrifugation supernatants . . . . .	103
8.8	Calibration data for fluorescence based DNA density determination . . . . .	103
8.9	Calibration data for UV-Vis based DNA density determination . . . . .	104
8.10	Exemplary CV curves of MEA electrodes . . . . .	105
8.11	UV-Vis spectra of citrate-capped AgNPs in different salt concentrations . . . .	105

8.12 Normed impact number for AgNP oxidation with varying concentration of NaCl in electrolyte . . . . .	106
8.13 Impact frequency for different potentials and electrolyte concentrations . . . .	106
8.14 Structure of predicted stem-loop folding of 17mer . . . . .	107
8.15 UV-Vis spectra of DNA-capped AgNPs in presence of magnesium ions . . . .	107





## List of Tables

3.1	Measurement parameters for current recordings with BioMAS system. . . . .	33
3.2	DNA sequences with respective functional groups and complementary strands labelled as cDNA. . . . .	35
3.3	Summary of used buffer solutions with composition and pH values. pH values adjusted with HCl or NaOH, accuracy: $\pm 0.05$ pH units. . . . .	41
3.4	List of used chemicals and suppliers. . . . .	41
3.5	Python functions used for data evaluation and plotting. . . . .	42
4.1	Success rate for stable nanoparticle modifications . . . . .	47
4.2	Summary of physical and chemical nanoparticle properties . . . . .	48
4.3	Parameters for DNA adsorption . . . . .	52
5.1	Average root mean square (rms) and peak to peak (pk2pk) noise for the picoAmp headstage and MEA chips . . . . .	56
5.2	Averaged values for the total number of impacts, frequency in Hz per chip and electrode, number of active, dead and noisy channels (of 63) for different measurement positions (1-5) . . . . .	60
5.3	Averaged values for the total number of impacts, frequency in Hz per chip and electrode, number of active, inactive and noisy channels (of 63) for different MEA chips . . . . .	61
5.4	Calculated extension of different DNA configurations. The value of contour length includes 1 nm for the thiol anchoring group [185]. . . . .	75
6.1	Summary of DNA folding predictions based on the Mfold web server [147]. T = 25°C, $c_{\text{NaCl}}$ = 50 mM. . . . .	84
8.1	Summary of results from ICPMS . . . . .	102



# Acknowledgements

This work would not have been possible without the help and support of so many other people and I would like to thank everyone, who supported me during my thesis.

First of all, I would like to thank Prof. Dr. Andreas Offenhäusser for his supervision and giving me the opportunity to work at his institute. I really enjoyed working on a fascinating research topic in this highly interdisciplinary team.

I would also like to thank Prof. Dr. Ulrich Simon for agreeing to act as second reviewer for this thesis.

Special thanks goes to Dr. Dirk Mayer for the supervision of my work in his research group. He always had time for fruitful discussions and gave me a lot of stimulating advices and ideas for experiments and interpretations. His support and guidance helped to navigate this thesis in the right direction.

Furthermore, I want to thank Prof. Dr. Bernhard Wolfrum and his group for support and training on my topic and for generously sharing their data analysis and evaluation method with me.

I want to thank Marko Banzet for the preparation of many MEA chips in the cleanroom and Elke Brauweiler-Reuters and Elmar Neumann for the recording of nice STEM images of my samples.

Especially, I want to thank Tina Breuer, Dr. Vanessa Maybeck, and Elke Brauweiler-Reuters for organizing everything regarding the labs. Without their work the life of us PhD students would have been a lot more complicated.

Additionally, I want to thank Dr. Vanessa Maybeck for all the discussions regarding the biological part of my thesis.

Furthermore, I want to thank Fabian Brings and Johannes Lewen for the support with the measurement system and any kind of issues related with programming.

A special thanks goes to the groups of IBI-6 and IBI-2, who gave me the possibility to use their equipment. Sometimes I was using their equipment more than any of their lab members and I always received help and support for any kind of issues.

I want to thank the whole group for the nice time and atmosphere at the institute. Special thanks goes to Kagithiri, Pegah, Corinna and Frano for the great time, lots of nice lunch breaks and activities aside the scientific work. Thanks for motivating and cheering me up, whenever it was necessary.

I want to thank my good friends, Alina, Anna and Julia, who have accompanied me now for almost 10 years throughout my complete studies. Without them my time in Cologne would not have been that great.

Particularly, I want to thank my family for their endless support. Finally, I want to thank Thomas for his support and for always being there for me. Thank you for believing in me and building me up whenever it was needed.

Band / Volume 52

**Resistive switching memory devices from atomic layer deposited binary and ternary oxide thin films**

N. Aslam (2017), X, 172 pp

ISBN: 978-3-95806-274-0

Band / Volume 53

**Operando X-ray photoemission electron microscopy (XPEEM) investigations of resistive switching metal-insulator-metal devices**

C. J. Schmitz (2017), IX, 153 pp

ISBN: 978-3-95806-283-2

Band / Volume 54

**Optimization of powder and ceramic processing, electrical characterization and defect chemistry in the system  $\text{Yb}_x\text{Ca}_{1-x}\text{MnO}_3$**

M. Rahmani (2018), XIV, 164 pp

ISBN: 978-3-95806-323-5

Band / Volume 55

**Organic-Metal Hybrid Interfaces at the Mesoscopic Scale**

G. Zamborlini (2018), xi, 133 pp

ISBN: 978-3-95806-328-0

Band / Volume 56

**Configurable frequency synthesizer for large scale physics experiments**

N. Parkalian (2019), xxi, 114 pp

ISBN: 978-3-95806-393-8

Band / Volume 57

**Resistive switching phenomena in stacks of binary transition metal oxides grown by atomic layer deposition**

H. Zhang (2019), ix, 196 pp

ISBN: 978-3-95806-399-0

Band / Volume 58

**Element-Selective Investigation of Femtosecond Spin Dynamics in  $\text{Ni}_x\text{Pd}_{1-x}$  Magnetic Alloys using Extreme Ultraviolet Radiation**

S. Gang (2019), 93, xx pp

ISBN: 978-3-95806-411-9

Band / Volume 59

**Defect engineering in oxide thin films**

F. V. E. Hensling (2019), 10, 164 pp

ISBN: 978-3-95806-424-9

Band / Volume 60

**Chemical control of the electrical surface properties of *n*-doped transition metal oxides**

M. Andrä (2019), X, 150, XXXVIII pp

ISBN: 978-3-95806-448-5

Band / Volume 61

**Digital Signal Processing and Mixed Signal Control of Receiver Circuitry for Large-Scale Particle Detectors**

P. Muralidharan (2020), xv, 109 pp

ISBN: 978-3-95806-489-8

Band / Volume 62

**Development of Electromagnetic Induction Measurement and Inversion Methods for Soil Electrical Conductivity Investigations**

X. Tan (2020), ix, 124 pp

ISBN: 978-3-95806-490-4

Band / Volume 63

**Novel System Approach for a mm-range Precision Indoor Positioning System**

R. Xiong (2020), xi, 144 pp

ISBN: 978-3-95806-517-8

Band / Volume 64

**Quantitative investigation of group III-nitride interfaces by a combination of scanning tunneling microscopy and off-axis electron holography**

Y. Wang (2021), 102 pp

ISBN: 978-3-95806-534-5

Band / Volume 65

**Scalable Control Electronics for a Spin Based Quantum Computer**

L. Geck (2021), xiv, 114, xv-xxxiii

ISBN: 978-3-95806-540-6

Band / Volume 66

**DNA-capped silver nanoparticles for stochastic nanoparticle impact electrochemistry**

L. Nörbel (2021), VI, 142 pp

ISBN: 978-3-95806-541-3





Information  
Band / Volume 66  
ISBN 978-3-95806-541-3